Wireless Monitoring Systems for Long-Term Reliability Assessment of Bridge Structures based on Compressed Sensing and Data-Driven Data Interrogation Methods

by

Sean Michael O'Connor

A dissertation submitted in partial fulfillment
of the requirements for the degree of
Doctor of Philosophy
(Civil Engineering)
in the University of Michigan
2015

Doctoral Committee:

Professor Jerome P. Lynch, Chair
Professor Anna C. Gilbert
Professor Victor Li
Associate Professor Jason P. McCormick
Professor Radoslaw L. Michalowski

© Sean M. O’Connor

2015

DEDICATIONS

To my parents, Chuck & Maria, and my wife Yilan
for all their support

ACKNOWLEDGEMENTS

This work was supported by the United States Department of Commerce, National Institute of Standards and Technology (NIST), Technology Innovation Program (TIP) managed under the direction of program manager Dr. Jean-Louis Staudenmann. Additional support was provided by the Michigan Department of Transportation (MDOT) with special thanks to David Juntunen, Peter Jansson and Matt Niemi. The authors would also like to acknowledge the generous support provided by the National Science Foundation (NSF) through grant number CCF-0910765 (PI: Prof. M. Flynn, University of Michigan). Additional support was provided by the Office of Naval Research under Contract Number N00014-10-1-0613.

There has been vast support in conducting the research presented here. I would first like to acknowledge my advisor, Professor Jerome Lynch, for his mentorship and guidance. He has not only taught me what it means to be an academic but also how to be a professional in the research community. He has constantly supported my research and has been the primary driver in the culmination presented here. Professor Lynch has been a teacher, mentor and friend throughout my time at the University of Michigan for which I will be forever grateful.

My first experiences with the LIST lab were with Dr. Junhee Kim, Dr. Andy Zimmerman and Dr. Andrew Swartz. Dr. Kim was my daily mentor and truly a great friend. He was the greatest influence to my initial contributions to the LIST lab and provided the basis for everything

I would learn over the next five years. Dr. Andy Zimmerman and Dr. Andrew Swartz shared their expertise in their design and development of the *Narada* wireless platform which I utilized extensively to conduct the research presented here. I have a great amount of respect and admiration for these individuals and will always value their knowledge and friendship.

I would like to thank my dissertation committee, Professor Victor Li (CEE), Professor Radoslaw Michalowski (CEE), Professor Jason McCormick (CEE) and Professor Anna Gilbert (MATH) for their guidance and support with my thesis work. Professor Michalowski guided my very first research experience in an off-site pipeline monitoring project at Cornell University the summer before graduate school. My experience with this project had an enormous impact on my decision to conduct research during my graduate studies. Professor Gilbert guided my understanding of sparse signal analysis and approximation as well as the Compressed Sensing research shown in Chapter 3.

I want to acknowledge my fellow graduate students whom have worked side-by-side with me for the majority of my time in the Laboratory for Intelligent Systems and Technologies (LIST). In particular: Dr. Mike Kane, Dr. Courtney Peckens, Jeff Bergman, Dr. Sukhoon Pyo, Ted Byrne, Nephi Johnson, Andy Burton and Mitsuhito Hirose. I owe a great amount of gratitude to these individuals for their friendship and support. This group of people has made the past five years a truly enjoyable experience and have shaped a lot of great memories for me. There is a large group of fellow graduate students outside of the LIST whom have also made the graduate program a memorable social experience. In particular: Dr. Sid Nadakuru, Dr. Clinton Carlson, Eric Warner, Rudy Nie, Alyssa Kody, Paul Beata, Jon Hubler and Will Greenwood to name a few.

Finally, I want to acknowledge my family for their love and support. My wife, Yilan Zhang, constantly motivates me and is my biggest supporter. She has shown me a love and caring that I could not have imagined before and has truly given my life a new meaning. My parents, Charles and Maria, have always supported me and encouraged me to continue my education. Their love and support is the root of all my achievements and is a model for the person I strive to be.

TABLE OF CONTENTS

LIST OF FIGURES

LIST OF TABLES

ABSTRACT

Wireless Monitoring Systems for Long-Term Reliability Assessment of Bridge Structures based on Compressed Sensing and Data-Driven Data Interrogation Methods

by

Sean Michael O'Connor

Chair: Jerome P. Lynch

The state of the nation's highway bridges has garnered significant public attention due to large inventories of aging assets and insufficient funds for repair and replacement. Current management methods are based on visual inspections (VI) that have many known limitations including reliance on surface evidence of deterioration and subjectivity introduced by trained inspectors. To address the limitations of current inspection practice, structural health monitoring (SHM) systems can be used to provide quantitative measures of structural behavior and an objective basis for condition assessment. SHM systems are intended to be a cost effective monitoring technology that not only measures structural behavior but also automates the processing of data to characterize damage and provides information to aide asset managers with their decisions. Unfortunately, this realization of SHM systems does not currently exist. In order for SHM to be realized as a decision support tool for bridge owners engaged in performance- and

risk-based asset management, technological hurdles must still be overcome including: reduction of SHM sensing costs, optimization of sensing strategies given system energy constraints, and scalable data interrogation architectures that translate raw sensor data into actionable information that empowers decision-making.

This thesis focuses on advancing wireless SHM systems; wireless SHM adopts wireless sensor networks (WSN) as a means of eradicating the high costs of installing wiring in a structure. An innovative wireless monitoring system was designed for permanent deployment on bridges in cold northern climates. Northern climates that are cold and overcast are an added challenge to permanent WSN as the potential for solar harvesting is reduced and batteries are more difficult to charge. First, efforts advancing energy efficient usage strategies for WSN due to the energy constraints of wireless sensors powered by solar energy were made. With WSN energy consumption proportional to amount of data transmitted, data reduction strategies are prioritized to reduce the energy requirements of WSN. A novel data compression paradigm termed compressed sensing is advanced for embedment in a wireless sensor microcontroller for data reduction prior to transmission. In addition, fatigue life estimation algorithms are embedded in a wireless sensor for local data processing leading to dramatic reduction in data transmission demand. In the second part of the thesis, a radical top-down design strategy for a monitoring system is explored to target the specific damage concerns of bridge owners. The top-down strategy is in contrast to generalized global vibration approaches that are often “shooting in the dark” for damage detection. Data-driven algorithmic approaches on local bridge sub-systems are then created to provide statistical performance and reliability characterization of bridge response given long-term structural response and environmental data. Statistical process control (SPC) and reliability index (β) frameworks based on machine learning and Gaussian process regression

(GPR) methods are advanced as a scalable and autonomous means of transforming monitoring data into valuable information relevant to bridge risk management. Validation of the wireless monitoring system architecture is made using the Telegraph Road Bridge (Monroe, Michigan), a multi-girder short-span highway bridge that represents the majority fraction of the U.S. national inventory.

CHAPTER 1.

INTRODUCTION

1.1 State of the United States Bridge Infrastructure

1.1.1 Deterioration and Financial Constraints

The 2013 ASCE Report Card for America's Infrastructure reports that 24.9 percent of the nation's bridges are rated as structurally deficient or functionally obsolete as designated by the Federal Highway Administration (FHWA) [1] and assesses an overall grade of C+ [2]. It also states that an annual $20.5 billion dollar investment is required for significant improvement of bridge conditions while only $12.8 billion is actually spent [2]. According to the 2014 National Bridge Inventory (NBI), there are approximately 610,749 bridges throughout the United States [1]. A compiling of NBI data by Transportation for America shows that the average bridge age is 43 years while the average intended design life of bridges is typically 50 years [3]. Simultaneous financial constraints and growing inventories of aging bridges presents many difficult asset management challenges to bridge owners across the nation. The current task of maintaining these inventories is immense due to the sheer volume of bridges needing inspection and the costs associated with repairs. To make matters worse, travel demands are increasing while the cost of construction labor and materials is rising. A 2007 report by American Association of State Highway and Transportation Officials (AASHTO) states that by 2015 construction costs will have risen 70% from 1993 [4]. The FHWA also projects a 2.07% growth in highway travel through 2020 [5].

Of the U.S. national bridge inventory, approximately 41 percent (248,284) are classified as stringer/multi-beam or girder structure type [1]. Given this percentage, this class of bridge garners significant management attention by most bridge owners (*i.e.*, departments of transportation). Common defects in steel beam members include corrosion, fracture, out-of-plane deformation and traffic impact. This bridge class commonly utilizes a reinforced concrete deck. Cracking, delamination and spalling of the deck is a target of inspections due to its common occurrence. In multi-girder bridges, composite action construction is common to utilize the strength of the deck in the section properties of the girders [6]. If designed for, composite action is expected and relied upon for structural integrity; loss of composite action would be a significant defect in these bridge types.

Pin and hanger bridges are of particular interest in this dissertation. Pin and hanger bridges are a special type of stringer/multi-beam bridge type. These bridges utilize hanger plates (also termed link plates) to support adjacent girders from another. This design detail was used to allow for easier design calculations and to move bridge expansion joints away from the bridge bearings. Approximately 35 percent of the 2,914 bridges (1,012) with steel beams owned by the Michigan Department of Transportation (MDOT) are pin and hanger style designs [7]. The majority of these bridges were constructed between 1940 and 1980, soon after which the pin and hanger design was essentially discontinued in Michigan. Several problems with the pin and hanger detail have been documented [7, 8] including fracture, corrosion and beam-end contact. The Mianus River Bridge in Greenwich, Connecticut collapsed without warning in 1983 from a failed pin and hanger detail coupled with a lack of redundancy in the bridge design. The National Transportation Safety Board

(NTSB) highway accident report [9] found that the probable cause of the Mianus River Bridge collapse was undetected lateral displacement of the hanger plate caused by corrosion-induced forces. In 1978, the St. Clair River bridge in Illinois had several fractured hanger plates due to high stress from in-plane bending caused by corrosion induced pin-plate fixity [10]. The span did not collapse due to redundancy but did experience a drop in the bridge deck by as much as 0.75 inches (1.9 cm). A MDOT report [7] cited several pin and hanger bridges revealing problems in the state including corrosion, beam-end contact and link plate fracture. Figure 1-1 shows a typical link plate assembly and a link plate removed from a highway bridge in Michigan with considerable section loss due to corrosion.

1.1.2 Current State-of-Practice for Bridge Management

Following the 1967 collapse of the Point Pleasant Bridge [11], the U.S. Congress mandated the establishment of the National Bridge Inspection Standards (NBIS) in 1971 to develop and formalize a bridge inspection program [12]. The primary form of inspection has been and still is visual inspection (VI) [13]. There are seven basic types of inspection: 1) initial (inventory) inspection; 2) routine (periodic) inspection; 3) damage inspection; 4) in-depth inspection; 5)

Figure 1-1. Pin and hanger detail: (a) suspending center span girder from end span girder and (b-c) extensive corrosion damage and section loss.

fracture-critical inspection; 6) underwater inspection; and 7) special (interim) inspection [14]. An initial inspection is the first inspection for the bridge accompanied by load capacity ratings. This inspection records a baseline of structural condition. According to the NBIS, routine inspections should not exceed 24 months and some bridges require more frequent inspections. Damage inspections are unscheduled to assess damage from human actions (*e.g.*, vehicle collisions) or environmental factors. In-depth inspections are close-up inspections with better damage detection capability than routine inspection requirements offer. Fracture-critical inspections should be done at arm's length for tension elements whose failure could cause bridge collapse and may be supplemented by non-destructive testing (NDT). Underwater evaluations generally require diving for scour evaluations and inspections should not exceed 60 months. Special inspections are non-scheduled inspections at the owner's request to monitor suspected issues such as scour or fatigue [14]. Inspection tasks include visual examination, physical examination, and evaluation of bridge components by trained inspectors. Bridge deficiencies are usually described by corrosion, cracking, splitting, overstressing, collision and connection slippage [14]. Based on inspection grades, maintenance and repair tasks can be scheduled as needed.

While VI is an effective management tool, it does come with several drawbacks. Damage is not always manifested at the surface and damage locations may be hard to reach or view. Also, VI is inherently subjective as perceptions and notions of damage can vary from person to person; it has been reported by the FHWA that significant improvements are needed with regard to VI results variability [15]. Even though inspectors are trained to ensure inspections are uniformly executed and quality controls are used, routine inspections reports have been observed to show significant variability in condition rating (predicted that only 68% vary ± 1 point of the average and 95% will vary ± 2 points [15]). It was also reported that in-depth inspections are unlikely to correctly identify the defects intended for the in-depth inspection; for example only 3.9% of weld inspections correctly identified the presence of crack indications [13]. VI also has cost implications as they are laborious and are often contracted to third-party inspectors. Reports on the annual cost of bridge inspection is about $1,200 per bridge resulting in a cost of over $350M for the U.S. per year [16].

Alternatively, non-destructive evaluation (NDE) techniques are also used in bridge inspection including electromagnetic testing, ultrasonic testing, infrared and thermal testing, radiographic testing, magnetic particle testing and acoustic emission testing, among many others [17]. A brief description of the above mentioned NDE methods is given (as adapted from [18]), to provide some context for each method. Eddy current inspection is a common form of electromagnetic testing used to detect cracks at or below the surface of metallic objects. Eddy current testing uses alternating current in a coil close to the specimen of interest to generate eddy currents in the test specimen. Eddy currents will change over time with material changes such as cracks. Ultrasonic testing uses known properties of sound waves in a particular medium to infer material degradation and specimen boundaries. Change in velocity and reflectivity of ultrasonic waves introduced into the test specimen are used to quantify changes in the specimen. Infrared and thermal testing typically uses thermal imaging cameras to detect hot-spots or heat flow which is sensitive to material properties and boundaries. Radiographic testing includes X-ray testing to detect discontinuities in metals including cracks and welds. Magnetic particle testing detects surface and near-surface flaws by observing the collection of loose particles at locations of magnetic flux leakage. The test specimen must be electrically conductive and large currents may be needed for large specimens. Finally, acoustic emission methods monitor cumulative sound energy produced by degradation (*e.g.*, crack growth) [19]. AE is commonly used to detect crack formation in cables and concrete decks. These NDE methods are often used in short-term deployments for a specific prescribed inspection and often require impeding traffic; such methods are not cost-effective (and in some cases infeasible) for continuous monitoring. The drawbacks associated with NDE methods include manual application of technologies by trained technicians, technician subjectivity to interpret results (*e.g.,* acoustic emission threshold selection), the cost of equipment and *a priori* knowledge of damage locations. To complement visual inspections (which are infrequent and often subjective) permanent sensor systems installed in a bridge have been widely implemented for continuous (or frequently periodic) structural monitoring. Similar to NDE methods, structural monitoring offers a quantitative and objective basis to evaluating a bridge structure.

1.2 Structural Monitoring and Health Assessment

The growth and proliferation of sensor technologies largely propelled by industry investments and government funding [20] has improved the ability of engineers to monitor structures for performance assessments. Structural monitoring (SM) encompasses VI, NDE and sensor data methods to assess structural performance. The use of structural sensor systems have been reported to undergo three phases over the last 50 years [20]: 1) assessing structures with new design concepts; 2) monitor performance and limits of performance from extreme loading; and 3) most recently, assess structural health. When SM is combined with damage detection strategies and the data interrogation process used for health tracking is automated, SM is then referred to as structural health monitoring (SHM).

SHM has been described as the process of implementing an automated means of damage detection for civil, mechanical and aerospace infrastructure based on monitoring data [21-23]. The growing complexity of bridge management makes evident the need for SM (and SHM) to provide a means for more cost effective bridge management. While some researchers may view SHM as having the potential to replace VI, this thesis views SHM as providing a direly needed quantitative basis regarding damage detection of a structure (*e.g.*, bridge) as a powerful complement to VI. Many academic and commercial sensing technologies have been deployed for bridge SHM including wireless sensors, self-sensing materials, piezoelectrics, among others [24]. In addition, researchers have leveraged the large number of SM systems deployed on bridges to develop and refine algorithms that identify structural damage. While a tremendous amount of research (and commercialization) attention has clearly been focused on SHM over the past two decades, major technical obstacles still exist for the technology that must be addressed. These obstacles are preventing emergence of a commercially viable SHM system (or framework) that can be applied generally to a broad class of structures with clear and justifiable benefits enumerated for bridge owners. It is for this reason that there are a large number of structural monitoring systems on bridges but very few SHM systems to date.

1.2.1 Challenges of SHM

Widespread adoption of SHM has been slow for several reasons. First, wired SHM systems are costly, obtrusive and do not scale well as channel costs increase faster than linear with channel count. Channel costs have been reported from $5,000 per channel [25] up to $22,000 per channel for larger systems [26]. As a result of high costs, the effectiveness of the SHM system is never realized as budget constraints may not allow an adequate number of sensor channels. Especially with damage being a local event, scaling the system to capture damage (especially its onset) may require high sensor density in a structure. SHM systems which are too expensive to make a positive cost-benefit case will have no hope for widespread commercial adoption.

Second, standard SHM algorithmic approaches have not proven to translate well from laboratory to real-world structures. This is partly due to measurement uncertainties introduced by sensors, environmental influences (*e.g.,* temperature variations) and load influences, and structural uncertainties including boundary conditions, as-built connectivity and material properties. As a result, changes in structural parameters are difficult to attribute exclusively to damage because non-damage influences [27] can have as large if not larger effect. SHM algorithmic practice has traditionally been physics-based (*e.g.,* model updating [28]) or data-driven (*e.g.,* outlier detection [29]) supported largely by global acceleration measures [30]. Physics-based approaches utilize physical understanding of system mechanics to build mathematical models describing expected response behavior. Residuals from sensor data and expected physics-based healthy model data are settled by adjusting model parameters (*e.g.,* stiffness) or introducing damage models (*e.g.,* crack growth models). A major challenge in physics-based models is a lack of knowledge on the physics of the damage event [31, 32]. The effectiveness of physics-based damage detection methods such as those based on FE model updating have been challenged due to the high amount of uncertainty associated with a structure's modal characteristics (*i.e.,* modal frequency, modal damping, mode shape) which often form a basis for analysis. Specifically, modal characteristics are global properties that exhibit limited sensitivity to localized changes in the structure. Furthermore, they exhibit high sensitivity to variations in the environmental conditions (*e.g.,* temperature) [33, 34]. Data-driven approaches are typically divided into statistical and machine learning approaches, using monitored data to model system behavior. Statistical approaches fit probabilistic models to measured data while machine learning approaches attempt to recognize complex patterns and make decisions based on empirical separations [32]. Data-driven methods are only as good as the quality and quantity of data obtained. Statistical approaches have been proposed to better handle the inherent uncertainties in vibration measurements (and structural properties derived from them) when making statements about damage in the presence of varying environmental and operational conditions (EOCs) [35]. Outlier detection methods including statistical process control (SPC) on time-history features can be effective [36] but have not been widely adopted by asset managers, possibly due to a lack of physical intuition or design criteria in the process.

The third challenge of SHM is how to integrate monitoring data into decision making processes [37, 38]. As the cost of sensor technologies continue to reduce, sensor density will grow along with the volume of data being collected. Large sets of data demands scalable strategies for data management to efficiently store and process big data sets for the extraction of decision making information.

1.3 Emergence of Wireless Telemetry for SHM

Structural monitoring systems typically convey measurements from installed sensors (*e.g.*, accelerometers, strain gages, potentiometers) via coaxial cables to a central server for data acquisition, storage, and processing. Employing wireless sensor networks (WSNs) in lieu of wired sensors carry many advantages. First and foremost, wireless monitoring systems are without vast lengths of coaxial wiring and as a result can be installed very quickly, making them very cost effective in material and labor [39]. Driving installation costs down addresses the first challenge for SHM described in Section 1.2. Second, the modular nature of wireless sensors facilitates easy sensor placement and the creation of flexible system architectures (*e.g.,* mobile sensing) [40, 41]. Third, the low cost of wireless sensors drives high densities of sensors to be installed [42, 43]. Higher sensor densities scale monitoring systems to capture local structural behaviors, not just global behaviors. Fourth, most wireless sensor platforms possess computational capacity, enabling autonomous operation and local data interrogation; this is extremely valuable from a power consumption standpoint [44].

Since the introduction of wireless telemetry to SHM [39], several researchers have deployed wireless sensors for temporary and short-term monitoring of bridge structures [45, 46]. Many commercial and academic wireless nodes are available today including the “mote” wireless platforms (*e.g.*, MicaZ, iMote, iMote2, TmoteSky) [47-49] developed at UC-Berkely but commercialized by Crossbow, Intel, Memsic and Moteiv that run the TinyOS operating system [50]. In this thesis, the *Narada* platform [51] developed at the University of Michigan is used. *Narada* operates on a proprietary OS in a state machine architecture that offers real-time determinism to sensing tasks. Each of the abovementioned platforms operate using the IEEE 802.15.4 communication standards.

Several WSN implementations have been installed around the world for bridge monitoring over the past two decades. The use of wireless sensors with on-board intelligence offers opportunities for cost-effective local damage detection [52]. A number of long-term wireless bridge monitoring programs have been initiated for long-span bridges [53-55] but very few researchers have performed long-term monitoring on short-span bridges. This is unfortunate because SHM of short-span bridges could have a major impact due to the fact that they constitute the vast majority of bridges in the NBI. For example, approximately 86.7% of U.S. bridges have main spans between 20 ft. (6.1 m) and 99 ft. (30.2 m) and another 13.1% have main spans between 100 ft. (30.5 m) and 329 ft. (100.3 m) [56]. Also, short-span highway bridges receive less frequent inspection attention than long-span bridges and as a result may benefit more from the installation of permanent monitoring systems [57]. As wireless monitoring technologies mature and their costs continue to decline, the ability to deploy a large number of sensing channels in a bridge monitoring system continue to increase. Table 1-1 lists a few notable short-term and long-term WSN's implemented for bridge monitoring over the past two decades.

1.3.1 Short-Term Deployments

Wireless systems deployed for days to several months are considered short-term deployments. Modal analysis is a common goal of short-term installations since modal properties can be extracted from short-term data (ignoring time-varying effects of environmental and operational conditions). Load-carrying capacity evaluations can also be performed during short-term load testing. There is a long history of short-term WSN's installed for bridge monitoring since 1998. The Alamosa Canyon bridge was among the first bridges instrumented for wireless sensing [58, 59]. Studies utilizing the Alamosa Canyon Bridge utilized academic wireless sensor prototypes powered by batteries to measure bridge accelerations to forced loading such as vehicular traffic [60]. Kim, *et al.* [61] deployed a short-term wireless network on the Golden Gate Bridge with 64 MicaZ nodes measuring acceleration. The study reports high quality data acquisition and cites transmission bandwidth constraints. Additional sensor data sources in short-term WSNs have been used less frequently, such as strain transducers and temperature sensors targeting load distributions and neutral axis estimations. For example, Whelan and Janoyan [62] developed a multi-functional WSN using accelerometers and strain gages to meet the requirements for load rating and short-term dynamic vibrations analysis. Gangone, *et al.* [63] instrumented a highway bridge in New York with wireless sensors collecting acceleration, strain and temperature data for capacity and demand measures, including load rating. Many other short-term wireless monitoring systems have been demonstrated on bridges [46, 64]. All of these short-term WSN's have cited the need for power management methods in order to implement long-term monitoring systems [46, 61] such as implementing sleep states and power harvesting.

1.3.2 Long-Term Deployments

Very few long-term wireless monitoring systems have been implemented to date as long-term systems face more significant technical challenges than short-term systems. These challenges include power supply, communication reliability, sensor reliability and challenging environmental conditions. Long-term systems are harder to install as they must be hardened against the outside environment and fastened securely in hard-to-reach locations. These systems have traditionally been acceleration-based and dedicated to signature, long-span bridges. The Stork Bridge, (200 ft. or 61 m) a cable-stay bridge in Winterthur, Switzerland was instrumented with a long-term WSN in 2007. Vibration-based cable stay force monitoring is performed using the Tmote Sky WSN platform [49] interfaced with accelerometers and a temperature/humidity sensing chip [55]. To resolve energy constraints from solar power, the Stork Bridge WSN utilizes low power hardware, low duty cycle radio operation and embedded computing. To the author's knowledge, this system remains in operation at the time of publication. One of the two Jindo Bridges which are twin cable-stayed bridges in Haenam, South Korea, was instrumented with seventy nodes deployed in 2009 [53] and extended to 113 nodes with 669 channels in 2010 until 2012 [65, 66]. The instrumented bridge is a three-span steel-box girder cable-stayed bridge with a 1,130 ft. (344 m) main span and 230 ft. (70 m) side spans [53]. The Jindo Bridge project was deployed to develop a cost-effective automated wireless monitoring framework using an iMote2 WSN [65]. The study also allowed researchers to address fundamental issues of field deployed WSN including time synchronization and communication reliability [66]. The implementation utilized solar panels for power as well as on-site and off-site data storage and processing to handle the large amount of sensor data collected

Table 1-1. Notable WSN structural monitoring projects

Bridge	Location	Bridge Type	Year	Duration	Wireless Platform	Sensing Transducer	Channel Counts
Short-Term (< 3 months)							
Alamosa (Straser [58])	Truth or Consequences, New Mexico	multi-girder conc. deck	1996	5 days	WiMMS	a	
Alamosa (Lynch *et al.*, [60])	Truth or Consequences, New Mexico	multi-girder conc. deck	2002	5 days	WiMMS2	a	7
Geumdang (Lynch *et al.* [46])	Icheon, South Korea	concrete box grider	2004	3 days	WiMMS2	a	14
Golden Gate (Kim *et al.* [61])	San Francisco, California	suspension	2007	~month	MicaZ	a	64
Wright Rd. (Whelan *et al.* [62])	St. Lawrence County, New York	multi-girder conc. deck	2009	N/A	Tmote Sky	a, s, t	40
Big Sucker (Gangone *et al.* [63])	Waddington, New York	multi-girder conc. deck	2011	2 days	N/A	a, s	90
Gi-Lu (Weng *et al.* [64])	Nan-Tou County, Taiwan	cable-stayed	2007	N/A	WiMMS2	v	12
Long-Term (> 3 months)							
Jindo (Jang *et al.* [53])	Haenam, South Korea	cable-stayed	2009 - 2012	3 years	iMote2	a, t, h, l, w	669
Stork (Feltrin *et al.* [55])	Wintherthur, Switzerland	cable-stayed	2006 - current	9 years	Tmote Sky	a, t, h	6
New Carquinez (Kurata *et al.* [54])	Vallejo, California	suspension	2011 - current	4 years	*Narada*	a, d, w, t, h	81

Sensing designations: (a) acceleration; (d) displacement; (h) humidity; (l) light; (s) strain; (t) temperature; (v) velocity; (w) wind

from 2009 - 2012. The New Carquinez (Alfred Zampa Memorial) Bridge, is a steel suspension bridge connecting Vallejo, CA and Crockett, CA, measuring 3,500 ft. (1,067 m) long with the main span between towers measuring 2,300 ft. long (700 m). The New Carquinez Bridge (NCB) was instrumented with a WSN consisting of 33 *Narada* nodes in 2010 (currently still in operation) measuring 124 channels of acceleration, strain, displacement, wind speed, temperature and humidity [54]. Solar and vibration based energy harvesting [67] provided power while data storage and data-to-information processing were addressed using a cyber-infrastructure framework that enabled easy but secure access to data for system end-users. The NCB deployment was motivated by California Department of Transportation (Caltrans) interest in post-seismic decision making assistance. While these long-term system deployments prove that wireless monitoring is a feasible alternative to more costly wired systems, they also reveal that more research is needed to improve the performance of wireless sensors deployed long-term in harsh field conditions. Specifically, power consumption, network stability, environmental factors and data management all require attention to harden these systems for more reliable performance.

1.3.3 Addressing Wireless Power Limitations for Long-Term Monitoring

The main limitation of WSNs deployed as part of a monitoring system is power. Civil infrastructure systems often do not provide a native power supply that WSNs can use for their operation. Strategies have been employed to increase the amount of energy available for use in the system through advanced energy harvesting techniques such as solar, wind, vibration, and RF scavenging [67-69]. Simply reducing power consumption at the wireless sensor node has also been enabled through the use of low-power hardware components in their design [51] and sleep states in their operation [70, 71]. Energy harvesting techniques and lower power hardware address the power limitations of WSN from one direction (*i.e.*, supply side); adoption of energy-efficient usage strategies approach from the other (*i.e.*, demand side). While trends in power harvesting are promising, the supply of energy provided by compact (*i.e.,* on the same scale of dimension as the packaged sensor module) power harvesting technologies is still smaller than the energy demand of most WSN hardware.

The low cost and modular installation of WSNs are undoubtedly driving the deployment of high density sensor installations resulting in high volume data transmission. Since the wireless radio has the largest power requirements in a wireless sensor node [72], data reduction techniques prior to transmission can go a long way towards power savings and in turn, preservation of limited local energy (*e.g.,* battery energy). There are also many other benefits to converting high bandwidth streams of raw time history sensor data to lower bandwidth streams of processed data. (*i.e.,* information). For example, data reduction preserves the use of the shared wireless communication channel. This in turn can improve the reliability of the wireless channel, especially for large WSNs. Another benefit is that end-users get more valuable information from the WSN. Specifically, processed information as opposed to raw sensor data can be more readily used by system end-users. Fortunately, most wireless sensors have some capacity for computation [52] as the microcontroller needed for digital communications also opens the door for local data processing. Data processing algorithms embedded in the computational core of a wireless sensor can convert raw time-history data into more compact forms. Several instances of embedded processing at the wireless node have been demonstrated, transforming high dimensional time-history data into lower dimensional information relevant to management and decision making. Tanner *et al.* [73] captured measurement extremes from high rate sampling as well as calculated correlation coefficients between accelerometers for statistical process control outlier detection for detection of structural damage. Zimmerman *et al.* [74] modified three output-only modal estimation methods (peak-picking, random decrement and frequency domain decomposition) for implementation in an array of processors distributed in a wireless network to emphasize parallel processing opportunities. Lynch *et al.* [75] were among the first to demonstrate the use of microcontrollers in wireless sensors for embedded analyses of civil infrastructure, programming statistical pattern recognition time-series models (AR and ARX) on-board a wireless sensor for damage detection. Numerous other examples exist for embedded and distributed computing in WSNs engaged in structural monitoring [76-78].

Another strategy to reducing data is the use of lossless [79] and lossy [80] data compression prior to wireless transfer of uniformly sampled raw sensor time-histories. Similar to data interrogation algorithms, the wireless sensor node utilizes its embedded data processing capabilities to compress raw data. Traditional compression methods, whether lossy or lossless, require complete time-history data before compression can ensue, keeping computational and storage requirements at the sensor high. Lynch *et al.* [79] implemented lossless Huffman coding into a microcontroller which exploits statistical relationships in the data to minimize data transmissions. Specifically, high probability data gets short symbol representation for transmission and low probability data gets long symbol representation. Compressed sensing [81-83] is an emerging lossy compression technique which realizes compression at the sampling stage of the data acquisition process through a number of encoded measurements, keeping sampling, storage and mathematical operations demands low. Other researchers have also begun exploring the use of CS for structural monitoring, such as damage detection [84], acceleration compression [85] and data loss recovery [86].

1.4 Bridging Structural Monitoring and Asset Management

There is currently a great divide between SHM practice and what is required for long-term asset management. Great progress has been made in SM and SHM development but there are still significant gaps that need bridging. Past wireless structural monitoring programs, such as those listed in Table 1-1, have made progress towards reducing the cost and complexity of installing structural monitoring systems but challenges are still apparent. The requirements for structural monitoring programs to be commercially viable and adoptable by owner's are they need to: 1) be cost-effective; 2) be long-term / permanent in duration; 3) capture damage scenarios of primary concern; 4) be preventative; 5) account for measurement uncertainties; 6) provide some degree of automated decision support. The introduction of wireless telemetry has made the cost of large-scale sensor systems feasible. However, power remains an issue for wireless systems and will continue to govern the long-term sustainability and communication reliability of the sensing system. Even as hardware power consumption and power harvesting technologies improve slowly and incrementally energy-efficient usage strategies offer the greatest opportunity for addressing the power limitations of WSNs. In order to target specific damage scenarios, sensing will need to be less general and less global. By tailoring a monitoring strategy to specific damage modalities, the monitoring system is closer to providing quantitative information about issues the owner is making decisions about (*e.g.,* repair now or wait to later). This strategy also aligns the monitoring system with VI information which is also based on damage events in bridge components. Owners are also more interested in damage prevention than in damage detection. Especially with the current financial climate, owners are placing renewed emphasis on preserving the current inventory by avoiding damage. Many current SHM sensor and algorithmic strategies are built for damage detection rather than damage prevention; therefore, modifications to sensor strategy and algorithms should be made to ensure systems are addressing owner needs. Conventional SHM typically stops with damage detection and does not consider the relevance of the result or the decision support that should be given after damage is characterized. If SHM systems are to be widely adopted for use, they will need to be more informative to owners in preventative maintenance decisions.

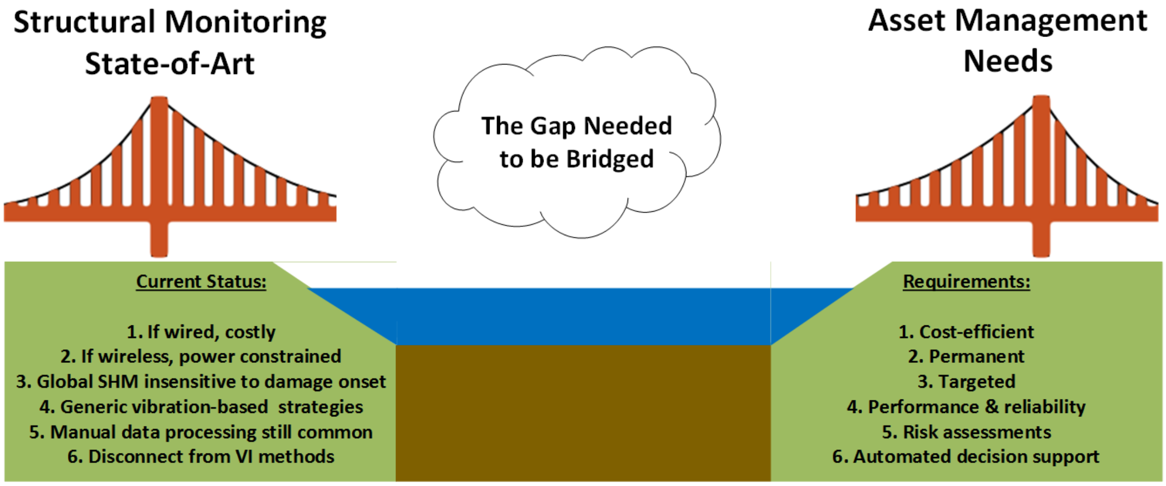

Figure 1-2. Bridging the gap between current state-of-practice SHM and long-term asset management empowered by data.

Owner's as well as SHM system designers are facing a large dilemma in meeting the goals of asset management as summarized by Figure 1-2. The owner needs to determine how to bring what is currently at his/her disposal (*i.e.*, VI and NDE methods) and convert that information into achieving performance goals to avoid damage, mitigate deterioration and preserve structures. The SHM designer needs to also determine how to cast sensor data into information relevant to asset management as well as convince the owner that monitoring can best enable that goal and do so cost-effectively and reliably.

1.4.1 Need for Risk-Based Asset Management

A reactive-only approach to bridge management seems infeasible in the current cost climate. Preventative maintenance provides a more cost-effective strategy over the entire bridge life-cycle as prevention often costs much less than repair or replacement [87]. The U.S. Congress placed a new emphasis on preventative maintenance over rehabilitation and replacement with the SAFETEA-LU bill in 2008, changing the name of the Highway Bridge Replacement Program

(HBRP) to the Highway Bridge Program (HBP) and allowing HBP funds to be spent on systemic preventative maintenance (SPM) [87]. This gives state transportation departments more flexibility in deciding whether to spend money on repair and replacement or prevention. The Moving Ahead for Progress in the 21st Century (MAP-21) surface transportation law enacted by Congress in 2012 as a two-year extension of SAFETEA-LU goes further by placing a special emphasis on transforming the management of highway infrastructure to a performance and outcome-based program. In particular, through the National Highway Performance Program (NHPP) states are required to develop risk- and performance-based asset management plans for the National Highway System (NHS) to improve or sustain asset condition and performance with penalties of reduced funding for non-compliance [88].

With new motivation and flexibility for preventative maintenance the task arises for assessing highway structures appropriately for maintenance needs. Existing bridge management programs utilizing Pontis [89] and BRIDGIT [90] algorithms revolve around condition ratings provided by VI and have been criticized for focusing on damage detection rather than reliability [91, 92]. Also, VI is not always capable of detecting defects. Introducing reliability analysis for structural assessment [93-95] has had a large impact on structural analysis and design, including the development of the LRFD design code. The use of reliability methods for bridge assessment [96-99] has been observed at least for the past 30 years.

As bridge management moves towards performance- and risk-based approaches, the gap between VI and risk analyses needs to be addressed. Sensor-based monitoring can be an enabling technology towards this goal. Structural monitoring encompasses VI and additionally includes objective sensor data information. Monitored data has the opportunity to further feed performance objectives such as capacity-demand assessments of in-service structures. Building further, statistical data information including the uncertainties associated with capacity and demand measures directly enables reliability analysis. Jumping from reliability to risk entails attaching a concept of consequences to failure modes which is not part of this thesis. Figure 1-3a illustrates the owners' dilemma while Figure 1-3b illustrates how sensor monitoring can potentially enable the transition from VI to risk-based asset management. Instead of viewing monitoring as a means of finding damage, an alternative strategy is to view monitoring as providing insight to structural behavior that reveals the capacity of the system and its components. With understanding of the loads imposed on a bridge (*e.g.*, traffic loads), a reliability framework would now be feasible.

1.5 Research Objectives and Dissertation Outline

The forward trend in bridge management lies in performance and reliability monitoring, as highlighted by the MAP-21 enactment requiring performance- and risk-based asset management. As such, this thesis focuses on the development of a WSN as well as algorithmic approaches

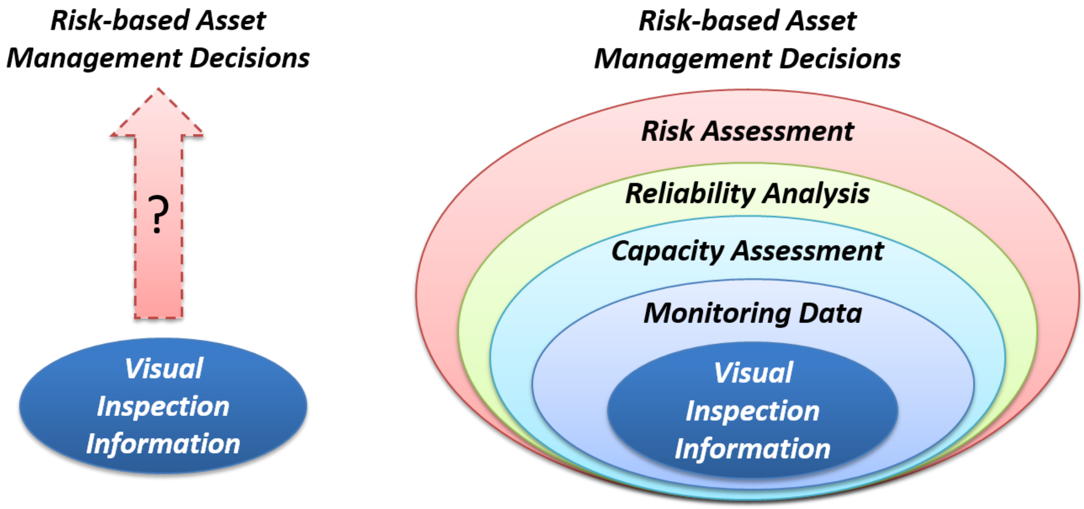

(a) (b)

Figure 1-3. Illustrations of (a) the owner's dilemma in going from visual inspection (current) to risk-based (future) management and (b) how sensor monitoring can be an enabling technology to resolve this dilemma.

targeting performance and reliability measures for long-term management. In this thesis, a novel long-term wireless structural monitoring system for a very representative highway bridge class is demonstrated for performance-based capacity-demand monitoring and reliability-based condition assessment. The WSN deployed on the Telegraph Road Bridge (TRB) is the first long-term WSN for a short-to-medium span highway bridge in the nation. Implementation of a WSN for monitoring short-to-medium span highway bridges is a valuable contribution in itself as there are very few such systems deployed and the procured long-term performance data is a valuable contribution towards future bridge management programs [100]. The FHWA's Long-Term Bridge Performance (LTBP) Program is a 20-year effort (minimum) authorized by the U.S. Congress to collect data from a representative sample of nationwide highway bridges to help better understand bridge deterioration and performance [100]. The work in this thesis is not part of the LTBP but presents the value of long-term performance data for in-service highway bridges. The testbed highway bridge used throughout this thesis is instrumented to address a number of health concerns particular to pin and hanger steel-concrete composite highway bridges. The data presented in this thesis adds to a scarce set of long-term performance data for the pin and hanger bridge class.

There are three main goals of the current study. The first goal is to implement a permanent WSN for structural performance monitoring hardened to survive a cold and overcast northern climate. The aforementioned challenges of power storage and power harvesting are magnified by northern winter environments and will require close attention to power management. To address the first goal of this study, solar panels and commercial charge controllers are used to provide complete power requirements to approximately 40 wireless sensors powering approximately 80 sensor channels, as well as a base station operating on a single board computer. Power efficient operational techniques for the *Narada* wireless sensor node [51] coupled with its low-power hardware design renders the sensing system capable of two weeks operation on a single 8V 3.2Ah sealed lead acid rechargeable battery in the absence of solar charging. Although the deep reserve of power seems excessive, the highly overcast and cold Michigan winter has shown to be a challenge to the sustained operation of the monitoring system. This work also addresses power limitations in WSNs for structural monitoring by implementing for the first time compressed sensing data compression and fatigue life monitoring embedded computing algorithms in a wireless microcontroller for field deployment and operational use in highway and naval applications.

The second goal of this thesis is to provide autonomous data processing frameworks to reveal performance insights otherwise unknown to structural managers by integrating data acquisition with embedded computational capabilities and cyber-infrastructure tools. Autonomous data processing is enabled through the embedded computational power of the *Narada* as well as the *SenStore* cyberinfrastructure framework [37], co-developed by the University of Michigan and SC Solutions (Sunnyvale, CA). Real-time tasks involving limited memory can be performed on-board the *Narada* node and provided to system end users upon request to limit transmissions. The thesis specifically focuses on embedment of fatigue estimation algorithms to convert strain time history data to peak strain histograms. Long-term statistical insights involving large data sets and computationally heavy algorithms are performed offline through the *SenStore* database.

The third goal is to implement a bridge performance- and reliability-based assessment strategy which targets typical damage modalities of the structure under investigation. A top-down sensor design strategy is implemented to drive the sensing strategy around primary damage concerns; the use of wireless telemetry is truly enabling here as the low-cost of wireless nodes permits high density instrumentation for accurate, localized measures. For the TRB, arrays of strain gages are used to assess long-term performance of composite action in the deck section, link plate bending and lock-up in the suspender details and beam-end contact due to thermal expansion. These three specific top-down strategies for sensing are intended to assess the performance of specific damage concerns for a specific bridge type and indicate damage inducing behavior, rather than damage itself. The global dynamic performance of the TRB is also monitored and characterized for on-site year-round environmental influence. Unfortunately, SHM practice has been largely unfruitful over the past two decades in terms of management support for bridge owners for the many reasons previously mentioned in this chapter. It is the goal of this thesis to move away from standard practice SHM and towards dense structural reliability assessments as they are a precursor to risk-based assessment. Reliability approaches are not new to the field [91, 101-105] but are far from being widely implementable at large-scale and often make many assumptions on capacity and demand. The goal of the top-down sensor strategy is to position the WSN to make capacity measures often ignored or assumed. Specifically, sub-system capacity can be largely affected by boundary condition (*e.g.,* pin and hanger rotation, steel-concrete interaction, free thermal expansion); as such these capacities are specifically monitored for introduction into a reliability framework. Coupling these information with load information (*e.g.*, WIM vehicle weight, temperature and thermal gradients) is a transformative approach that has great promise for adoption.

A permanent wireless SHM system deployed on the Telegraph Road Bridge (TRB) located in Monroe, MI, was designed and implemented as part of this thesis work. The system is unique by its long-term operation of a WSN on a short-span highway bridge, as well as its instrumentation strategy coupled with rich data processing techniques offering objective damage mitigating information to bridge owners. Information presented is driven by primary needs of the MDOT regarding link plate bridges [7], as well as more general health monitoring techniques previously shown to provide meaningful information towards the assessment of steel girder bridges such as neutral axis identification for composite action assessment [106]. Each analysis method is designed for automated information extraction to characterize structural performance insights otherwise unknown to inspectors and managers. Normalization of long-term data to EOC influence is done using regression methods with targeted system performance features presented within an outlier detection framework to enable automation. Reliability-based condition monitoring of a pin and hanger connection is proposed as a complement to current practice of VI and ultrasonic NDE, and to promote SHM systems as a tool for reliability-based management. The chapter layout of this thesis is illustrated in Figure 1-4 and described below.

Chapter 2 describes the TRB testbed in detail. The TRB was instrumented as part of the NIST Technology Innovation Program (NIST-TIP) effort that aimed to advance SHM technologies for infrastructure health management. The TRB instrumentation strategy was carefully designed based on specific concerns of MDOT (the TRB owner) in pin and hanger type bridges. A five year implementation reveals several insights in how to design and deploy a wireless sensor system to monitor a bridge and to collect appropriate data that serves as an input to structural performance analyses. The long-term performance of the TRB network and data collection are presented.

Chapter 3 describes an implementation of an emerging lossy data compression technique termed compressed sensing onto a wireless sensor platform to reduce bandwidth and power demands. The compressed sensing framework fits nicely into resource constrained embedded devices due to the simplicity of the compression technique applied at the sensor front-end (*i.e.*, at the time of data collection). Compressed data is assumed to be transmitted from the wireless sensor to a resource un-constrained device for signal recovery. Chapter 4 also addresses power and bandwidth concerns in wireless platforms by utilizing the computing power available for embedded fatigue life processing. On-board rainflow counting and power spectral density (PSD)

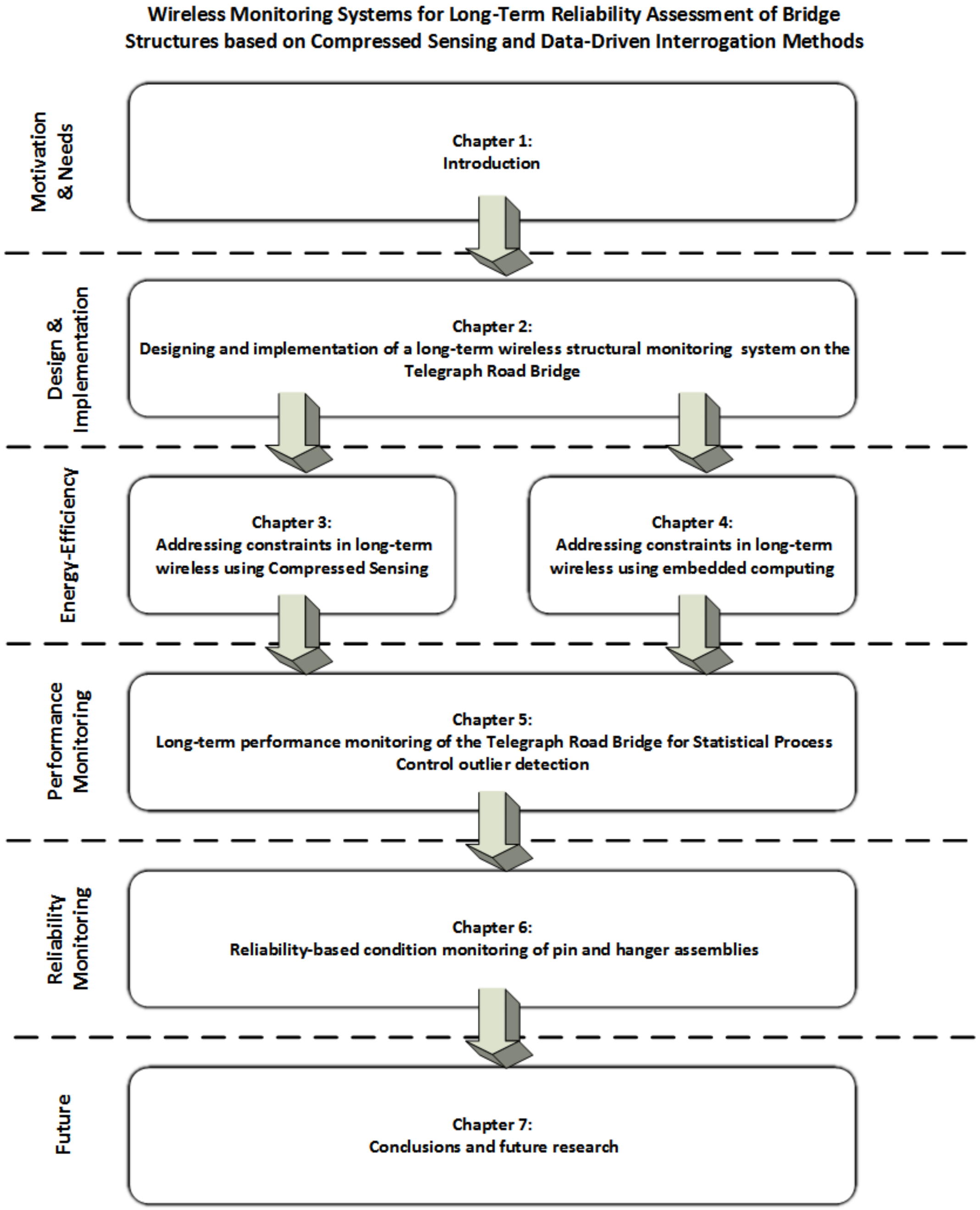

Figure 1-4. Schematic outline of thesis topics presented.

operations allow time-history data to be compressed into a fixed sized data structure (*i.e.*, a histogram). Transmission requirements in this case are largely removed, and can be performed on user request only.

Chapter 5 and Chapter 6 promote the use of long-term WSN’s to support performance- and risk-based asset management programs. Chapter 5 utilizes long-term data collected on specific damage modalities to model dependencies on environmental and operational condition (EOC’s) and further characterize the statistical behavior of each process to be cast into an automated outlier detection framework. Chapter 6 describes how long-term condition monitoring for pin and hanger assemblies can feed reliability-based management and capacity estimations. Pin and hanger limit states are evaluated for reliability to promote a framework for risk-based management. Limit state random variables are either taken from literature or estimated by long-term data statistics. The pin and hanger study in Chapter 6 also attempts to indicate incipient damage by detecting behavioral changes that lead to increased demands and lost capacity (pin locking, corrosion induced net-section loss).

Chapter 7 summarizes the work presented in this theses, discusses future work needed to continue the process of moving SHM towards decision making and states the key intellectual contributions made by the thesis.

CHAPTER 2.

DESIGN OF A LONG-TERM WIRELESS STRUCTURAL HEALTH MONITORING SYSTEM FOR PERFORMANCE ASSESSEMENT: THE TELEGRAPH ROAD BRIDGE DEMONSTRATION PROJECT

2.1 Introduction

Among the goals of this thesis work is to implement a permanent WSN for structural performance monitoring. The system should be hardened to survive a cold and overcast northern climate and serve as a testbed for developing performance- and reliability-based sensing strategies as well as signal processing techniques that can improve the power and bandwidth constraints inherent to wireless systems. A top-down sensing strategy which targets typical damage modalities and primary concerns of bridge owners is required. The system is multi-functional using accelerometers, strain gages and thermistors for local and global behavior monitoring. In addition to the sensing system, a server base station is designed to enable Internet connectivity and autonomous data processing to reveal performance insights otherwise unknown to structural managers. Solar panels and commercial charge controllers are used to provide complete power requirements to approximately 40 wireless sensors powering approximately 80 sensor channels, as well as a base station operating on a single board computer. Power efficient operational techniques for the *Narada* wireless sensor node [51] coupled with its low-power hardware design renders the sensing system capable of two weeks operation on a single 8V 3.2Ah sealed lead acid rechargeable battery in the absence of solar charging. Although the deep reserve of power seems excessive, the highly overcast and cold Michigan winter has shown to be a challenge to the sustained operation of the monitoring system. Acceleration based monitoring contributes to the overall effort of performance monitoring and is included in this chapter as a demonstration of long-term data acquisition and automated processing. However, the top-down sensor strategy promoted (and shown more in Chapter 5) is strain-based using acceleration only as supplemental information (along with temperature). Strain sensor placement is tailored to local system behavior rather than global or point behavior. Specifically, arrays of strain gages are used to assess long-term performance of composite action in the deck section, link plate bending and lock-up in the suspender details and beam-end contact due to thermal expansion.

This chapter describes a permanent wireless SHM system deployed on the Telegraph Road Bridge (TRB) located in Monroe, MI. The TRB was instrumented as part of the NIST Technology Innovation Program (NIST-TIP) effort that aimed to advance SHM technologies for infrastructure health management. A five year implementation has revealed several insights into design, deployment and data collection practices. The system is unique by its long-term operation of a WSN on a short-span highway bridge, as well as its instrumentation strategy. The system presented is driven by primary needs of the MDOT regarding link plate bridges [7], as well as more general health monitoring techniques previously shown to provide meaningful information towards the assessment of steel girder bridges such as neutral axis identification for composite action assessment [106].

2.2 Telegraph Road Bridge

The Telegraph Road Bridge (TRB), which is owned and managed by the Michigan Department of Transportation (MDOT), was constructed in 1973 and is located in Monroe, Michigan (Figure 2-1). The bridge carries two-lanes of northbound I-275 highway traffic (a separate bridge exists for southbound traffic) with the bridge experiencing routine heavy truck traffic due to its close proximity to the large manufacturing industries of Detroit (Michigan), Toledo (Ohio), and Windsor (Ontario). The TRB is a skewed (33°) steel stringer bridge consisting of three spans that are supported by two end abutment structures and two interior piers. Each span

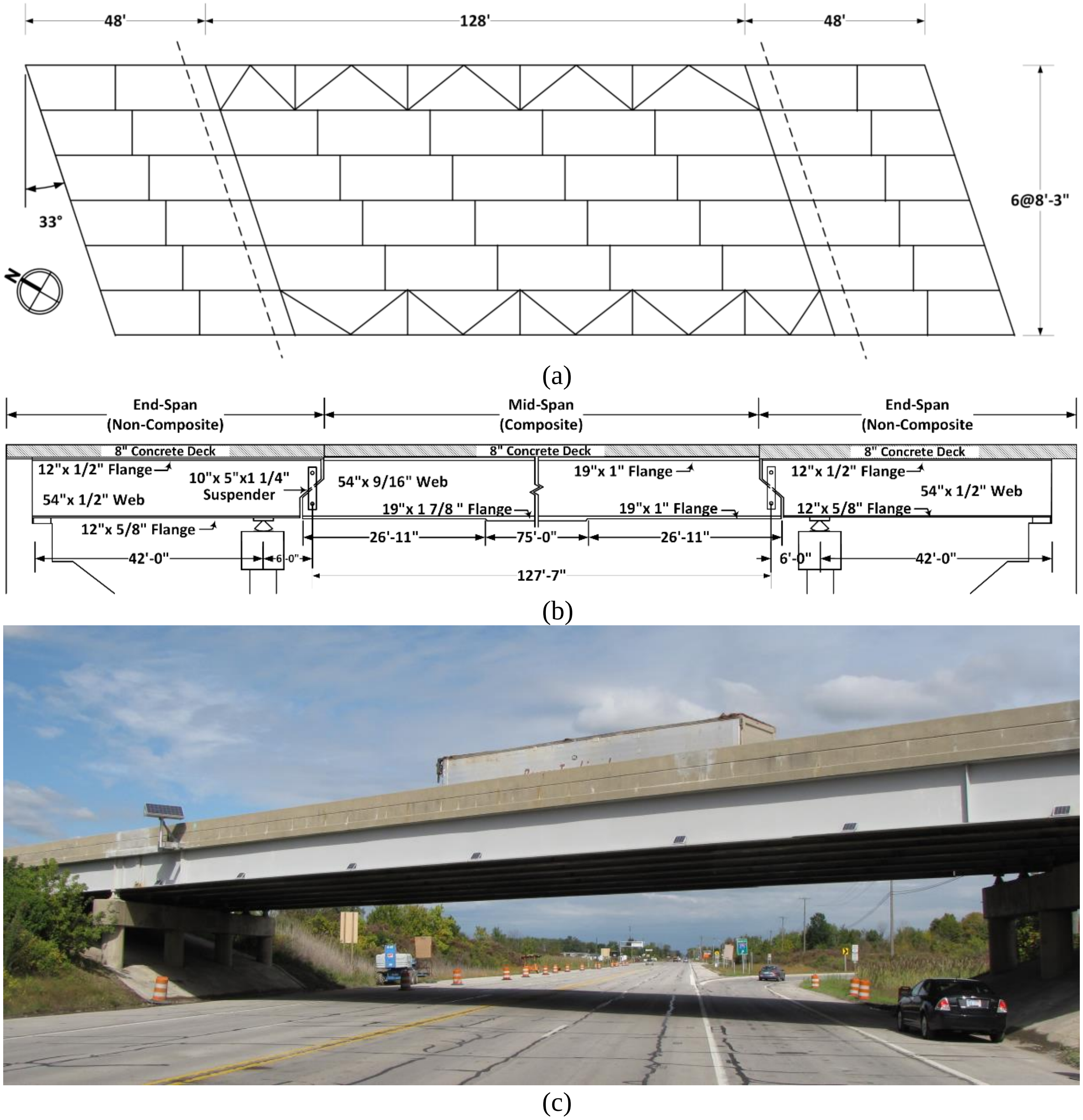

Figure 2-1. Telegraph Road Bridge: (a) erection diagram for built-up steel girders and bracing; (b) girder elevation showing major dimensions for end span and center span; (c) NB Telegraph Road view of bridge showing highway traffic above and solar panels on bridge perimeter.

consists of seven 54 inch (1.37 m) deep built-up steel girders whose centerlines are 99 inches (2.51 m) apart. The northern and southern spans are each 46.5 feet (14.17 m) long. Each of these spans is supported by an abutment structure on one end while the other end is cantilevered 6 feet (1.83 m) past rocker bearings supported by a concrete pier. The main center span is 128 feet (39.01 m) long and is suspended from the northern and southern spans through pin and hanger plate connections. At each end of the center span girders are two steel hanger plates resulting in a total of 28 plates supporting the center span. Each hanger plate is 42 inches (1.07 m) long, 10 inches (25.4 cm) wide, and 1.25 inches (3.18 cm) thick; the hanger plates connect to the girders through two steel pins with diameter 5 inches (12.7 cm). The bridge contains an 8 inch (20.32 cm) thick concrete deck with the deck in full composite action with the center span due to the presence of shear studs welded along the top flanges of the center span girders. The two side spans do not have shear studs so they are not expected to be in full composite action with the girders.

The TRB was selected in this study for two reasons. First, the bridge represents a very typical bridge in both the NBI and the MDOT inventory. As previously mentioned, approximately 41 percent (248,284) of the NBI are classified as stringer/multi-beam or girder type bridges [1]. In the MDOT inventory, approximately 44 percent (4,876) of the inventory are stringer/multi-beam or girder type. Even though the MDOT discontinued the use of pin and hanger details in the design of their new bridges in mid-1980's [107], many pin and hanger bridges remain in the MDOT inventory. Approximately 35 percent of the 2,914 steel beam bridges owned by the MDOT are pin and hanger style designs. Pin and hanger bridges use link plate assemblies to join adjacent spans, intending to create a hinge condition at the beam connection, allowing for easier design calculations and stress-free thermal expansion.

The second reason for the selection of the TRB was due to its age (42 years old) and age-based deterioration. Specifically, the recent inspection history of the TRB consistently cites several issues that are vigilantly watched by bridge inspectors. A large section of the northern abutment near the western corner had failed, as shown in Figure 2-2a, and was temporarily shored by a steel beam. The bridge deck has experienced cracking and spalling on its top surface (Figure 2-2b) as well as at the bottom-side haunch-girder flange interface. It is important to note that the decks of the northern and southern spans were significantly more degraded than that of the center span. Areas of heavy rust in the pin and hanger connections (Figure 2-2c) were noted in a 2011 inspection report indicating the plate-pin interfaces may be frozen, meaning that they may not be rotating due to corrosion between the plate, pin and possibly girder. A fatigue crack had developed in one of the steel girder webs at the connection between the girder web and the lateral bracing

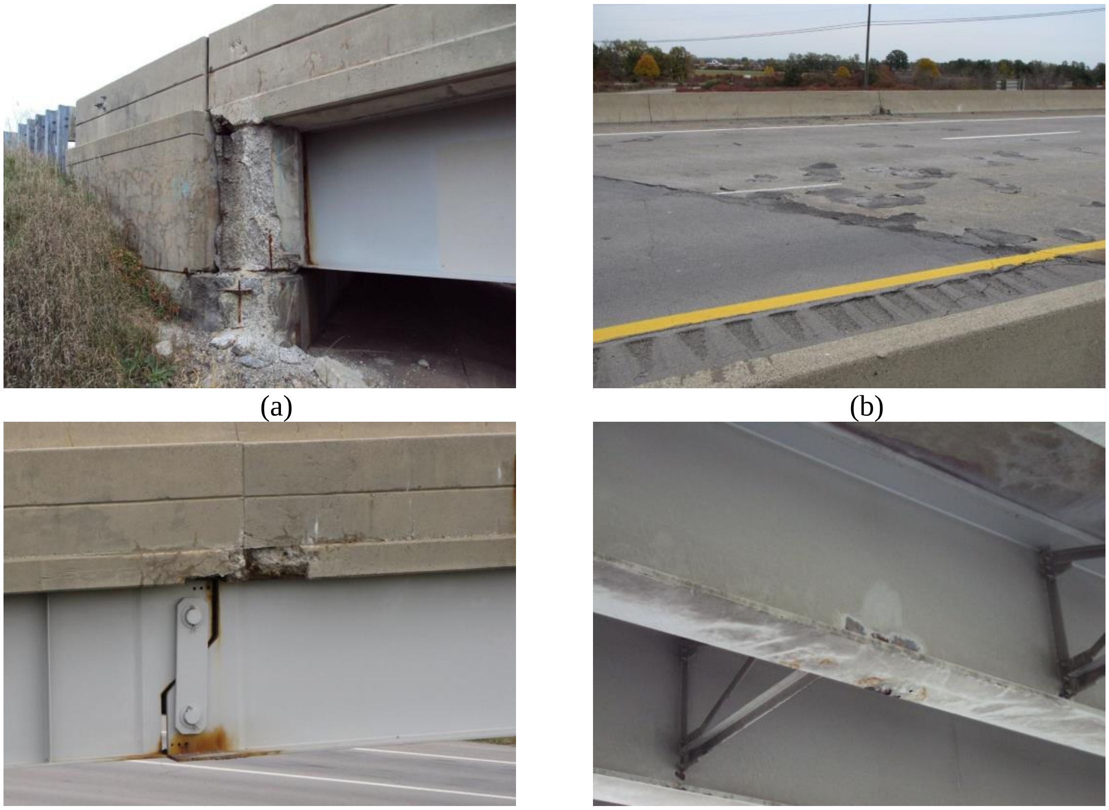

(a) (b)

(c) (d)

Figure 2-2. Deterioration history of the TRB: (a) northern abutment failure; (b) severe top-deck cracking and spalling; (c) pin and hanger plate corrosion; (d) web fatigue cracking.

system (Figure 2-2d). In 2011 (just prior to system installation), the TRB underwent a major renovation including repair of the failed northern abutment, hydro-demolition of the top surface of the bridge deck, repair of the web fatigue crack, and cleaning and painting of potentially corroded steel surfaces. The hydro-demolition repair of the bridge deck consisted of removal of the top deck to a height between the top and bottom steel reinforcement bar layers. A silica fume modified concrete (SFMC) was used as replacement on top of the remaining original concrete layer. Concrete cylinder testing of the SFMC showed compressive strengths between 6.4 ksi (44.1 MPa) and 7.4 ksi (51.0 MPa). The original concrete layer is noted in the bridge drawings to have design compressive strength of 3 ksi (20.7 MPa).

2.3 Monitoring System Design

Structural monitoring is an attractive management tool if and only if monitoring data can be used to improve the decision making of bridge owners. The majority of research in the field of structural health monitoring has focused on the creation of analytical frameworks that can be applied to a broad class of structures to identify damage (including existence, location, type, and severity) based on structural vibrations [21, 23, 30, 108]. While vibration-based SHM methods have shown great promise, this work offers an alternative monitoring strategy that is more closely aligned with the decision making processes of bridge owners (*e.g.*, MDOT). A top-down design strategy is proposed that explicitly maps the instrumentation strategy to the specific bridge performance issues that are of primary concern to the bridge owner. In the case of the TRB, the owner is primarily concerned with the behavior of the pin and hanger connections. Given the history of performance issues with pin and hanger connections on stringer bridges in Michigan [107], the monitoring system has a specific focus on the behavior of these connections. With respect to the pin and hanger connections, specific questions of the owner born out of past visual inspections include: 1) are the hanger plates locking due to corrosion; 2) what is the general state of stress in the hanger plates; 3) for the state of stress, what is the accumulation of fatigue in the plate relative to design life thresholds? Based on the past history of the failed northern abutment structure and severe cracking in the bridge deck, the owner was also interested in understanding the potential root causes of these deterioration mechanisms. Specifically, the following questions were of interest: 1) is the bridge experiencing restrained thermal expansion (*e.g.*, beam-end contact between the wing and center spans girders); 2) is deck deterioration coupled to the degrees of composite action between the deck and girders in each span?

To begin to answer these questions, the TRB monitoring system aims to install sensors that track specific response mechanisms over long periods of time that allow the normal (*i.e.*, healthy) baseline behavior of the bridge to be established. The monitoring system (and its information outputs) is intended to provide the bridge owner a quantifiable means of identifying when the bridge is moving away from its baseline healthy state towards a state with damage potential. To provide a robust baseline for normal bridge behavior, the environmental and operational conditions (EOC) of the bridge must also be concurrently monitored including thermal and vehicular loading. First, strain gage and thermistor arrays were designed to monitor the performance of the hanger plates at two locations. Strain gages installed on the hanger plates are positioned to allow axial strains and bending strains originating from corrosion in the pin and hanger assembly to be differentiated. Second, arrays of strain gages were designed to measure the strain profile through the bridge cross section at six locations. Three strain gages measure longitudinal strain in the steel girder and one strain transducer measures bottom side deck strain at the haunch-girder interface. To quantify the degree of composite action, the neutral axis of the section and strain continuity over the steel concrete interface are extracted. The strain transducers in the deck and thermistors also provide a means of assessing the expansion of the deck to ensure that girder-ends were not making contact potentially resulting in deck cracking, excessive rocker bearing displacements and abutment wall damage.

The TRB monitoring system was installed over nine months beginning in September 2011 and completed in June 2012; a number of minor system modifications have been made since its initial deployment. The monitoring system is comprised of two major parts: 1) a low-cost wireless sensor network based on the *Narada* wireless sensing platform [51]; 2) a cyberinfrastructure framework for the secure storage, curation and automated analysis of monitoring data. A wireless sensor network was elected over a traditional wired monitoring system to permit a dense monitoring system configuration at a relatively low deployment cost. In total, the monitoring system deployed on the TRB will include a total of 79 sensing channels collected using 39 *Narada* wireless sensor nodes (118 channels including battery monitoring). The wireless monitoring system on site is designed to push sensor data via an Internet-enabled base station to a secure server at the University of Michigan hosting the *SenStore* data management system [109, 110]. An important attribute of the TRB wireless monitoring system is that it has been hardened for long-term (*i.e.*, indefinite) operation in extreme winter climates (*e.g.*, low winter temperatures and snow/ice) common to northern climates such as Michigan.

2.3.1 Monitoring System Components

The TRB wireless monitoring system base station, as shown in Figure 2-3a and Figure 2-3b, is the common point of communication for the monitoring system architecture. A PC-104 single board computer running Linux is used as the monitoring system base station. It commands all *Narada* sensing operations through a Chipcon CC2420 RF transceiver operating on the 2.4 GHz

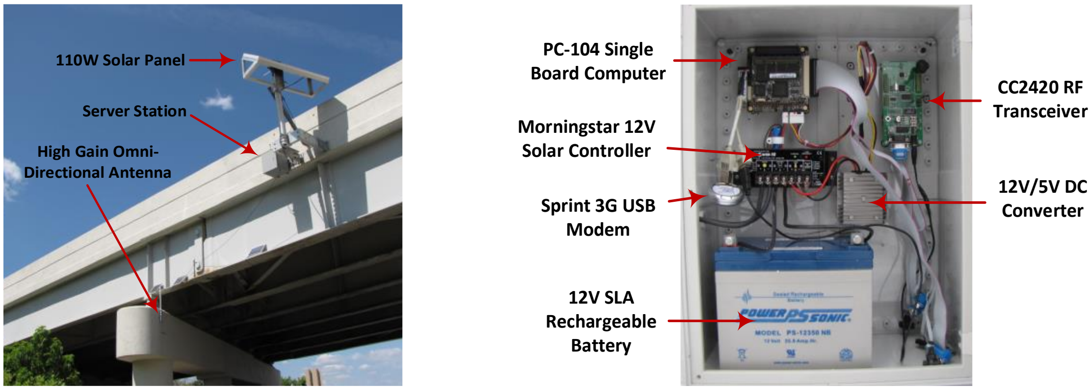

(a) (b)

Figure 2-3. TRB server station (a) installation to bridge fascia showing server station, solar panel and antenna (b) server station components inside waterproof enclosure (single board computer, solar controller, RF transceiver, rechargeable battery, DC-DC converter).

open industrial, scientific and medical (ISM) wireless channel. To boost the performance of the base station communications with *Narada* nodes deployed on the bridge, the Hawking Hi-Gain Omni-Directional 9dBi outdoor antenna is used by the base station transceiver and is mounted to the face of the north pier (underneath the girder line). In addition, a Sprint 3G Sierra Wireless 250U cellular modem is interfaced to the PC-104 computer via USB port to provide Internet access. The cellular modem has an external antenna that mounts on top of the base station enclosure. Solar energy provides all of the power consumed by the base station through the use of a UL-Solar 110W 12V multicrystalline solar panel. A SunSaver 10L charge controller is used to convert the solar energy generated by the solar panel to charge a PowerSonic PS-12350NB 12V 35Ah sealed lead acid rechargeable battery. Lead acid batteries are one of the few battery chemistries that can operate (including recharging) at low winter temperatures well below the freezing point. Additionally, a 12V-5V DC/DC converter is included in the base station design to step down the solar charging system voltage for direct use by the PC-104 computer. The entire system is enclosed in a water-tight cabinet mounted to the southerly facing fascia of the bridge.

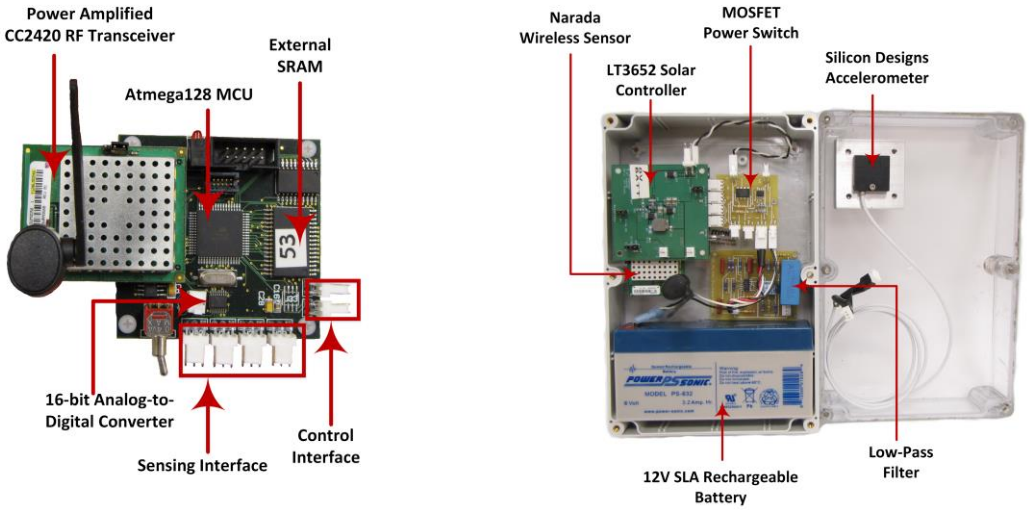

(a) (b)

Figure 2-4. *Narada* wireless sensor node: (a) standard node with key component highlighted; (b) complete *Narada* node enclosed in a waterproof plastic enclosure.

The building block of the TRB wireless monitoring system is the *Narada* wireless sensor node. The *Narada* wireless sensing node, shown in Figure 2-4a, was developed at the University of Michigan [51] specifically for use in structural monitoring applications. The *Narada* uses an Atmel Atmega128 microprocessor that operates at 8 MHz and has 128 kB of internal flash memory for the storage of embedded software. In addition, *Narada* is designed with an additional 128 kB of external SRAM to ensure the node has considerable data storage space. Wireless communications are handled by the Chipcon CC2420 IEEE 802.15.4 wireless radio that is contained on a separate daughter board that attaches to the main board of *Narada*. To ensure the node can communicate reliably over long distances, the radio board contains a power amplifier that provides the node with a line of sight communication range of over 2,300 feet (700 m) [111]. The *Narada* utilizes a four channel, 16-bit Texas Instruments ADS8341 analog-to-digital converter (ADC) for high quality data acquisition from any sensor that outputs a 0 to 5V voltage range. The *Narada* node when operating at 8 MHz consumes 60mA when transmitting, 30 mA when awake but not transmitting, and 2 mA when sleeping. Prior to deployment to the field, the *Narada* node is placed in a plastic waterproof enclosure along with a rechargeable sealed lead acid battery, battery charger, and signal conditioning circuitry associated with each sensor type (*e.g.*, amplified Wheatstone bridge circuit for strain gages, anti-alias filters) as seen in Figure 2-4b. Each *Narada* enclosure is powered by a single UL-Solar 10W 12V polycrystalline solar panel installed on the northern and southern fascia of the bridge. The sealed lead acid battery is continuously charged by the solar panel using the battery charger contained in the enclosure. To easily mount the enclosure to the bridge steel surfaces, four K&J Magnetics NdFeB (Grade 42) rare earth magnets are fastened to the bottom surface of the enclosure providing a contact force of 62.5 lb (0.61 N).

The last component of the monitoring system is the cyberinfrastructure that facilitates remote data storage and management. In particular, the wireless monitoring system adopts a data management system termed *SenStore* that was co-developed by SC Solutions (Sunnyvale, CA) and the University of Michigan [109, 112]. An instantiation of *SenStore* is created on a Linux server at the University of Michigan for the TRB. *Narada* nodes communicate data to the on-site base station that in turn utilizes its cellular connection to the Internet to securely communicate sensor data to *SenStore*. *SenStore* provides a scalable data management platform by combining three methods of data storage within the same data server: 1) relational database for bridge metadata; 2) hierarchical data format (HDF5) repository for sensor data; 3) flat file system for storage of files (*e.g.*, pictures, inspector reports). A PostgreSQL relational database is responsible for managing bridge metadata including bridge geometry, material types, component definitions, sensor location and sensor type, among others. While a relational database is well suited for relational data, it is ill suited for the storage of large tracks of time history data. To boost the query performance of the data server, sensor data is stored in an HDF5 repository that links to the relational database. The databases are included within a server-client model implemented using the Internet Communication Engine (ICE) technology. ICE provides server access via a flexible application programming interface (API) that is definable in various programming languages including Python, Java, and C.

2.3.2 Sensing Modalities and Configurations

The wireless monitoring system installed on the TRB includes a diverse number of sensors that are intended to track various bridge behaviors to external loading. The specific sensors selected along with their installation locations is motivated by the aforementioned top-down design strategy of the system. Figure 2-5 contains a summary of the sensors deployed on the TRB along with their locations. In general, the monitoring system contains three primary sensor types: 1) accelerometers to measure global vibrations; 2) strain gages to measure local strain responses; 3) thermistors to measure structural temperatures from external thermal loads. A total of 79 channels of data are collected using 39 *Narada* nodes (118 channels including battery monitoring). In this thesis, accelerometers are only included as a proxy measure for load magnitude. In the TRB monitoring system, the *Narada* samples 1-minute time-histories at 2-4 hour intervals.

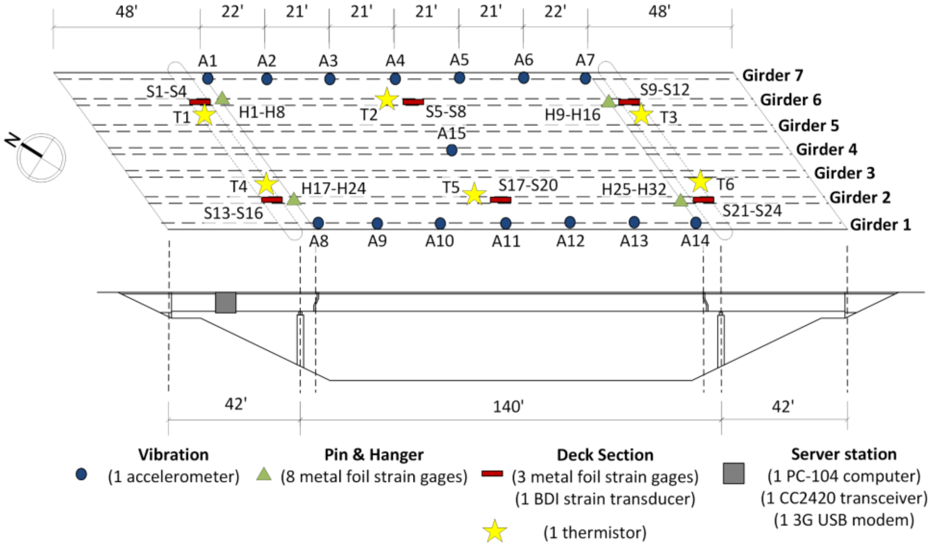

Figure 2-5. Sensing strategy on the TRB including sensor type and locations.

Accelerometers and strain gages are sampled at 200 Hz and 100 Hz, respectively; thermistor response and battery voltage are sampled at 1 Hz.

A primary management concern of the bridge owner is the performance and health of the TRB pin and hanger connections. In particular, there are four major concerns associated with pin and hanger connections [7]. First is fatigue; unanticipated extreme loads could lead to premature fatigue in the hanger plates. Second, corrosion is another concern that can result in the locking of the pin-plate connection. Should locking occur, the member would no longer behave as a pure axial element and would experience in-plane bending due to moments developing on the circumferences of the pins. Third, corrosion can occur behind the plate. The build-up of corrosion by-products can induce pressure on the plate resulting in out-of-plane bending and the walking of the plate off the pin. Finally, the link plate can corrode resulting in the loss of plate cross-section. To address these concerns, the wireless monitoring system is configured to closely monitor the hanger (link) plates at four locations in the bridge; namely, one hanger plate at each end of girder line 2 and 6 as shown in Figure 2-5. To address the concerns of link plate assemblies, a method to observe non-ideal performance in the link plate assembly is desired. Strain gages were attached to the link plates to identify in-plane bending (strong-axis), out-of-plane bending (weak-axis) and axial strain. This top-down sensing strategy targets live load deformation performance rather than material stress limits (which are assumed to be exceeded far after performance limits have been reached). Bending strains are consequences of corrosion buildup such as hindered rotation and link plate “walking” (when corrosion build up slowly forces the link plate down towards the end of the pin) as well as sway motions. Figure 2-6a shows the instrumentation strategy of the link plate strain gages that are intended to provide strain measures that can illuminate three possible modes of response (Figure 2-6b): axial deformation (normal), in-plane bending (abnormal) and

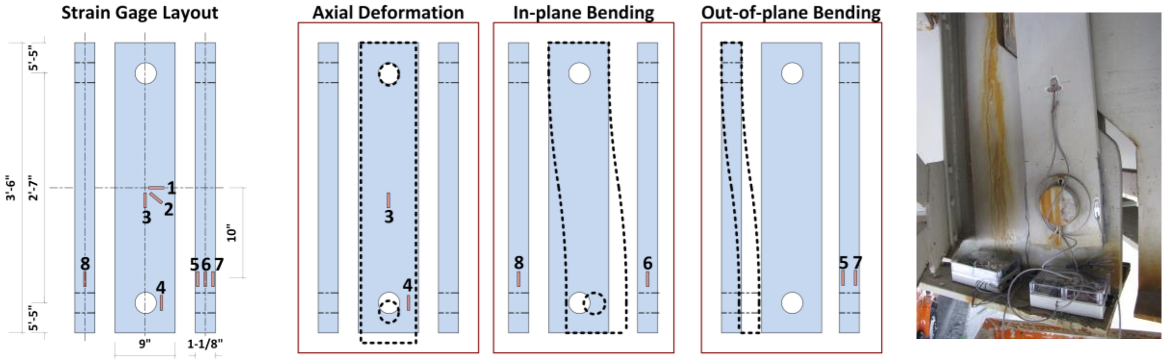

(a) (b) (c)

Figure 2-6. Link plate instrumentation: (a) strain gage layout with (b) targeted deformations sensors; (c) actual sensor installation.

out-plane bending (abnormal). A Micro-Measurements 350 Ω strain rosette (WK-06-060WR-350) is used at the center of the link plate (H1 - H3) providing three independent strain measurements. Additionally, five Tokkyo Sokki FLA-6-11-3LT 6 mm 120 Ω metal foil strain gages are used (H4-H8). Strain gage H4 was placed near the pin to observe stress concentrations anticipated at this location in the link plate. Strain gages H6 and H8 were placed on the sides of the link plate to measure in-plane bending strain, installed on the center line of the side face to remain as independent from out-of-plane strains as possible. A half-bridge configuration removes thermal effects and axial strains from this strain gage combination. Out-of-plane bending strains are measured using strain gages H5 and H7 with axial strains and thermal effects again cancelled by a half-bridge configuration; in-plane strain also cancels in this configuration. The metal foil gages installed on the link plates are interfaced to Wheatstone Bridge circuits followed by an Analog Device AD623 instrumentation amplifier for 1000 times gain prior to data acquisition. Figure 2-6c shows the installed hanger strain system on the TRB.

Another significant management concern is the health of the bridge deck. The side spans of the TRB have a history of rapid deterioration with cracking and spalling common. A history of severe damage to the west abutment as well as steel-concrete interface spalling may be indicators of the root causes of accelerated and localized deck deterioration. To ascertain potential causes for this deterioration, two major concerns are addressed by the monitoring system. First, an inability of the deck to freely expand due to beam end contact could lead to abutment and bearing damage as well as large loads across hanger plates and deck sections. Beam-end contact in pin and hanger bridges has been cited as a repeated problem for MDOT [7]. In the event that seasonal thermal expansion of the bridge deck exceeds the allotted displacement between spans, the beam ends will begin to bear on each other. The result is an unintended force directed across the diagonal portion of the beam ends which may lead to large stress increases in the link plates, local web buckling at the beam end and subsequent link plate disengagement from the pin [7], out-of-plane bending (weak-axis bending) and possibly link plate cracking. A one year MDOT study using vibrating wire strain gages [7] on a link plate revealed substantial stress increase estimated at about 2.3 MPa ⁄ ℃. Over a 60 ℃ change in temperature approximately 140 MPa stress increase was observed. Upon removal of the link plates MDOT measured a difference of 230 MPa indicating significant addition of dead load stress to the link plate due to beam end contact. Related problems include tilted rocker bearings on adjacent piers and beam pullout from the abutment support. For the proposed beam-end contact detection method in this study, Bridge Diagnostics, Inc. (BDI) strain transducers installed on the bottom side of the concrete bridge deck were used to measure thermal expansion. Under free thermal expansion, static strain measurements are expected to trend at a constant rate with temperature (at or near the thermal expansion coefficient). The TRB is assumed to operate with free expansion due to the pin and hanger design. BDI strain transducers were fixed to the concrete deck using a powder actuated bolt fastener for long term measurement. Static measurements from the BDI strain transducers began on October 1, 2013. Measurements were taken at six deck locations (S4, S8, S12, S16, S20 and S24). Each BDI sensor is coupled with a thermistor measuring local temperature. Thermal expansion coefficients for steel and concrete typically lie between 5 με ⁄ °F and 7 με ⁄ °F. Assuming that the link plate mechanism is operating freely, static strain response should correlate to thermal strain only. The BDI transducer itself requires post-processing corrections to provide thermal strain output; unpublished corrections from BDI were obtained and used in this study (personal communication, June 20, 2014). Second, losses in composite action can lead to serious performance issues and unsafe conditions, and should warrant a means to slow deterioration and/or increase inspections [113]. Slight loss of composite action in the steel-concrete section could lead to interface spalling and exposed reinforcement steel. Growing loss in composite action could lead to more severe deck deterioration and in the most severe case of composite action loss global instabilities are possible which could lead to catastrophic failure. To address these concerns, the wireless monitoring system is designed to measure composite action behavior at six locations of the bridge. Specifically, three locations on girder line G2 and three locations on girder line G6 were instrumented as shown in Figure 2-5, labeled S1 – S24. Four of the six locations measure side span behavior and two of the six measure center span behavior. A method to monitor composite action behavior is implemented by installing strain gages up the height of the steel-concrete section in an effort to build live load strain profiles induced by heavy truck crossings. The observed strain profile is used to verify continuity between steel and concrete and estimate the neutral axis position in the section. The degree of composite action in the bridge deck is inferred by comparing experimental and design calculated neutral axis positions. The expected neutral axis position as calculated from design drawings (under full composite action) lies at 53.5 in. (135.9 cm) from bottom flange for the end span section over the pier caps (S1-S4, S9-S12, S13-S16, S21-S24) and 47.8 in. (121.4 cm) from bottom flange for the mid-span sections (S5-S8, S17-S20). Figure 2-7a

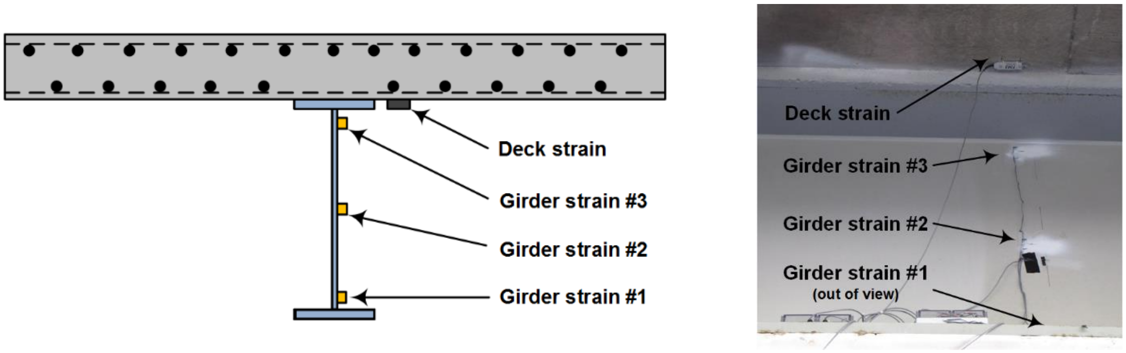

(a) (b)

Figure 2-7. Steel-concrete deck section instrumentation: (a) section strain gage layout; (b) actual sensor installation.

shows the instrumentation strategy intending to reveal both composite action and deck thermal expansion behavior; Figure 2-7b shows the TRB installation. The composite section is comprised of a 54 in. (137.16 cm) steel I-beam girder and approximately 10 in. (20.32 cm) reinforced concrete deck following deck resurfacing (originally an 8 in. deck) in August, 2011. The three steel girder strain gages are Tokkyo Sokki FLA-6-11-3LT 6 mm 120 Ω metal foil strain gages, placed at 3 in. (7.62 cm), 27 in. (68.58 cm), and 51 in. (129.54 cm) from the bottom flange of the steel girder. The deck sensor is a BDI strain transducer with an effective gage length of 3 in. (7.62 cm), placed on the bottom side of the concrete deck at 54 in. (137.16 cm) from bottom flange. The metal foil gages installed on the deck section are interfaced to Wheatstone Bridge circuits followed by an Analog Device AD623 instrumentation amplifier for 1000 times gain prior to data acquisition. The BDI strain transducers provide a differential output, the result of four internal active gages uniquely configured for axial response only. The differential signal is passed to an Analog Device AD623 instrumentation amplifier to convert to single-ended and for 500 times gain prior to data acquisition. Thermistor sensors are used to record structural surface temperatures, labeled T1 – T6 in Figure 2-5. U.S. Sensor Corp. USP13187 thermistors were installed with each group of strain gages, mounted to steel and concrete surfaces using 3M thermal epoxy. Thermistors are used to correct for thermal errors in strain gage response as well as correlate bridge behavior with temperature.

2.4 Power-Efficient System Configuration for Long-Term Operation

2.4.1 Power Harvesting and Storage

UL-Solar 10W 12V polycrystalline solar panels provide 100 percent of the power supplied to the TRB sensing system. Panels were chosen to provide adequate power for sustained sensing operations with minimal bridge footprint. The power system has seen two phases of instrumentation. Initially, Linear Technology LT3652 step-down battery chargers were used for charge control. The LT3652 is custom designed for solar powered operations with its ability to regulate solar input to keep panels at peak power output. At peak power conditions, the LT3652 was configured to charge an 8V 3.2Ah sealed lead acid (SLA) rechargeable battery at 1A, approximately a charge rate of 0.3C requiring about 3.3 hours to fully charge the battery from an empty state. PowerSonic 8V PS-832 rechargeable SLA batteries were used to store solar power, ideal for the harsh winter climate in Michigan as they have an operating temperature range for charging of -4°F (20°C) to 122°F (50°C) and discharging range of -40°F (-40°C) to 140°F (60°C). The LT3652, 8V SLA battery system was changed in May, 2014 to use SunSaver SS-10L-12V solar controllers with 12V SLA batteries. The commercial charge controllers provided an integrated low-voltage disconnect (LVD) and required no circuit board assembly, prompting the change in power management.

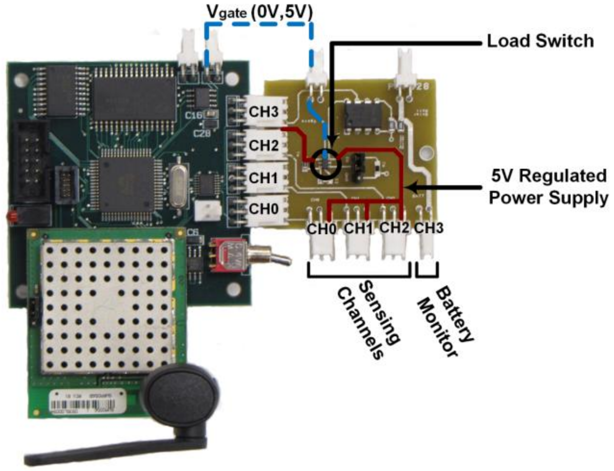

Figure 2-8. Load switch circuit interface for *Narada* using power MOSFET circuit in power line.

2.4.2 MOSFET Switching

Since the *Narada* wireless node was not originally intended for long-term sensing operations, the supply of power to connected sensors is direct from the battery power supply and as such the microprocessor has no regulation of sensor power consumption. To reduce power consumption, an external MOSFET-based load switching circuit was placed between the *Narada* node and sensor utilizing the Fairchild Semiconductor FDC6323L Integrated Load Switch. An easily accessible chip set line from the MCU for the digital-to-analog converter is used to raise and lower the MOSFET gate, effectively switching the power supply on and off to the connected sensor as desired. Figure 2-8 shows the load switching circuit board customized for *Narada* interface. The first three sensing channels (CHO, CH1, CH2) are passed through the load switch so that power supply to connected sensors is controllable. The fourth channel (CH3) is dedicated to monitoring battery voltage. A voltage divider is used bring the battery voltage into the sensing range of the *Narada* and an op-amp is used to buffer the signal. The chip set line for the D2A is chosen as the gate toggle since it holds 0V even when the MCU is in a sleep mode configuration,

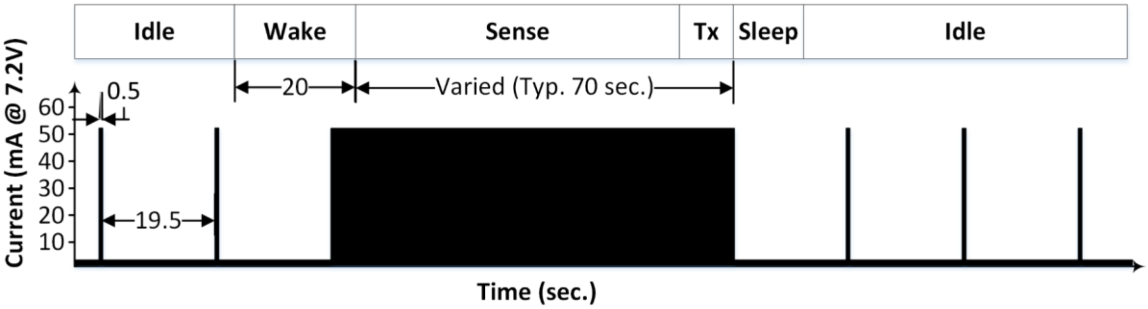

Figure 2-9. Duty-cycle of *Narada* for low-power sensing and long battery life.

effectively holding the load switch open during periods of inactivity. To switch power on to connected sensors, the chip set line is driven high (5V) forcing the load switch to close.

2.4.3 Sleep Mode Duty Cycling

Efficiency in power consumption at the sensor node is achieved through low-power sleep mode configuration to the microprocessor during standby time, as well as a disabling of the sensor when measurements are not being taken. *Narada* nodes are taken to a very low-power state by not only enabling the sleep mode in the Atmel Atmega128 microprocessor, but also disabling the radio which accounts for approximately half of the power consumed during sensing operations. Disabling the radio offers increased power efficiency at the wireless node. However, sensing operations are triggered by the base station via radio commands. In order to achieve an increased low-power state and also make the wireless node available to server commands, nodes are duty-cycled through power states to make all nodes briefly available to “wake-up” commands which take the *Narada* out of the low-power duty-cycle state, prior to issuance of sensing commands. The *Narada* is active for 0.5 seconds every 20 seconds (2.5 % duty cycle). Upon completion of sensing operations, the *Narada* node is returned to the low-power state to cycle in and out of sleep mode until the next sensing operation is issued by the base station. The power toggling routine is illustrated in Figure 2-9.

2.4.4 Results of Power Management

Both power management systems (8V LT3652 system & 12V SunSaver system) have been successful in harvesting and storing solar energy for sustained operations in the summer months. The LVD on the SunSaver has proven extremely valuable for winter weather management, preventing low voltages from corrupting *Narada* firmware which would require manual reprogramming of the wireless node. The SunSaver system will naturally shut down more often as a result of the LVD but will ensure that battery voltage remains at healthy levels. The use of the commercial charge controllers with LVD has significantly improved the ability of the wireless network to rebound after sustained harsh weather during winter months as shown by the long-term network performance chart in Figure 2-10a. The performance in winter 2015 is significantly better than winter 2014, having much less network failure and a fully operational network at the end of the winter period. Figure 2-10b shows data collected by the TRB system since 2011. The difference in summer and winter data collection is apparent for the W13 and W14; W15 portrays improved performance in data collection and a total of approximately 25 GB of data collected. Of note in Figure 2-10a is the server failure encountered in winter 2013. This failure resulted in a complete winter shutdown since access to the server module was limited during winter months. A more robust server configuration was designed to allow remote power toggling and receiver firmware reprogramming. Specifically, a power switch was integrated into the main power line using the WASP-S1 remote control system enabling hard power toggling to be performed from ground level at the TRB. In addition, a modification for remote reconfiguration of the receiver firmware was made by permanently installing an AVRISP MKII programming tool between the PC-104 single board computer and receiver and utilizing the AVRDUDE utility for remote flash programming.

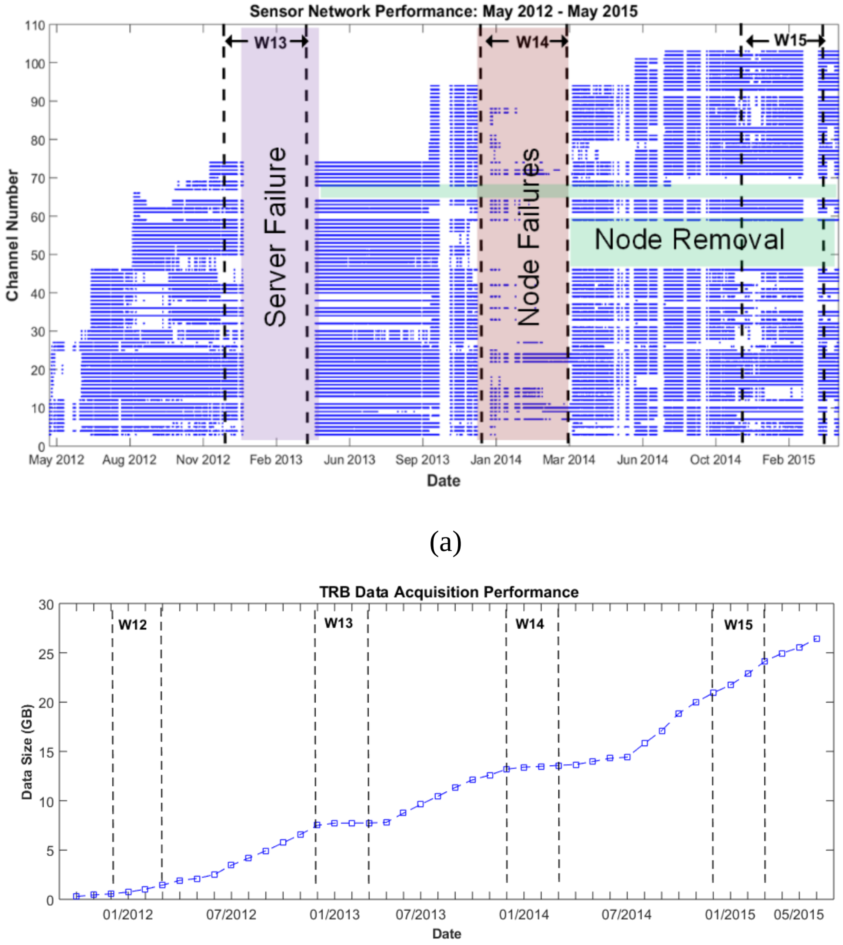

(a)

(b)

Figure 2-10. Long-term *Narada* network performance highlighting winter network failures and improved performance of 2015 winter: (a) channel network reliability (b) cumulative data collection.

Sleep state duty-cycling of the *Narada* coupled with MOSFET control of sensor power supply provided a power reduction of nearly 95% when compared to normal power operations, vastly extending the life of the wireless node. Absent of solar charging, the low-power modifications increase battery life from approximately one day to fifteen days. The extended life of the wireless node is essential for survival in the Michigan winter where it is not uncommon to experience extremely cold and overcast conditions for consecutive days or weeks.

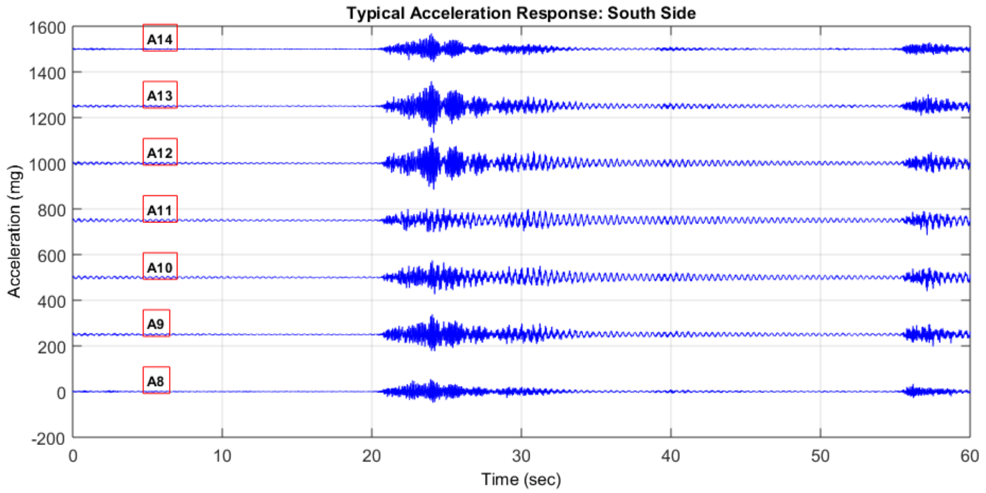

Figure 2-11. Acceleration time history at A8-A14 (vertical acceleration, Girder 1).

2.5 Long-Term Data Collection

2.5.1 Global Vibration

In this chapter, acceleration data collected from the TRB is shown to demonstrate long-term data collection, temperature sensitivity and an automation method for modal parameter extraction. Accelerometers installed around the perimeter of the main span have provided dynamic response data used for finite element (FE) model calibration and updating of the TRB previously [114]. In this thesis, vibration-based damage detection (VBDD) is not promoted as a long-term performance monitoring strategy for the TRB (described later in Chapter 5) but rather a focus on strain configurations believed to be highly sensitive to specific (and somewhat expected) damage scenarios and MDOT needs is utilized. Acceleration data is used in Chapter 3 to explore a data compression methodology and in Chapter 5 as a proxy measure for load magnitude.

Fifteen accelerometers (A1-A15) were installed to measure TRB deck vibrations. Figure 2-11 displays response from seven of the fifteen sensors (A8-A14) for a one minute duration sampled at 200 Hz. Responses are displayed in a stacked format to make easy observation of

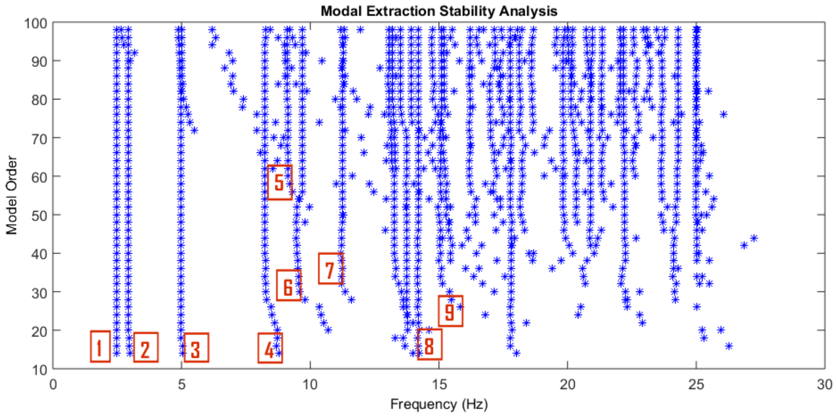

Figure 2-12. SSI stability plot generated from TRB acceleration data.

synchronized response across the bridge main span for a truck load near 21 seconds and a car load near 56 seconds. Accelerations up to ±150 mg have been observed for very large loads.

Stochastic Subspace Identification (SSI) methods are used for automated modal parameter extraction. SSI operates directly on time-history acceleration response with the assumption of white noise input. It is further assumed that bridge dynamics can be accurately described by the stochastic state space model

$$x_{k+1} = Ax_k + w_k \tag{2.1}$$

$$y_k = Cx_k + v_k \tag{2.2}$$

where $A \in \mathbb{R}^{2n\times 2n}$ is the state matrix containing system dynamics, $C \in \mathbb{R}^{l\times 2n}$ is the output matrix, $x_k \in \mathbb{R}^{2n\times 1}$ is the state vector, $y_k \in \mathbb{R}^{l\times 1}$ is the response measurement vector and w_k, v_k represent white noise inputs termed process noise and measurement noise, respectively; n is the number of poles. State space matrices (A, C) are calculated by techniques such as QR-factorization, Singular Value Decomposition (SVD) and least squares [115]. State space matrices define the system dynamics mathematically, leaving only eigenvalue decomposition to reveal modal parameters. A thorough discussion on SSI methods for modal extraction is omitted here but can be found in

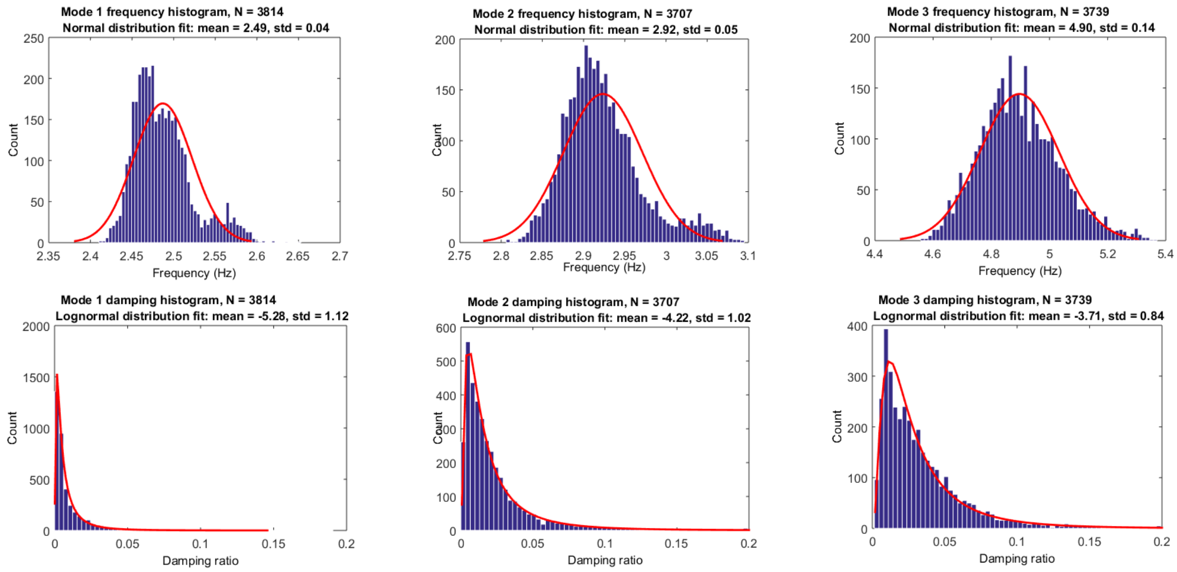

(a) (b) (c)

Figure 2-13. Modal extraction by SSI technique: frequency and damping for (a) 1st (b) 2nd and (c) 3rd modes.

classic literature [116, 117]. The particular algorithm used in this study is credited to Van Overschee and De Moor [117]. Output modes are not only physical modes but also mathematical modes, requiring a method to discriminate between the two for automation. Modal frequencies for physical modes are expected to remain fairly consistent with model order. Damping values for non-physical modes are often unreasonable, either much too large (*e.g.*, $> 10\%$) or much too small (*e.g.*, $< 0.1\%$) and are often used as a first filter when identifying physical modes. Several techniques for automating physical mode extraction from stability plots have been proposed including graph theory [118], clustering [119], relative difference between model orders for n times stable [120], and triangulation based methods [121]. Here, *a priori* knowledge is used for simplicity. Long-term test data informs us of frequency ranges to search in the stability plot for modes. SSI outputs for each model order within a frequency bin range are averaged to produce a frequency estimate. Figure 2-12 shows a stability plot generated with a TRB time-history with the first nine modes labeled. This automated extraction process was performed through *SenStore* on TRB data from December, 2011 to September, 2014. Figure 2-13 shows the long-term 1st, 2nd,

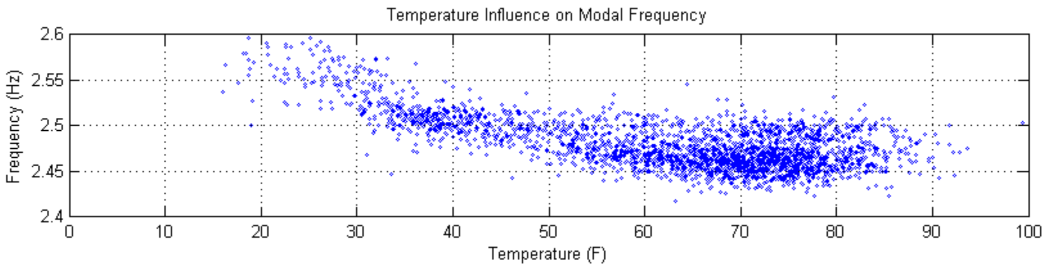

Figure 2-14. Modal sensitivity of TRB 1st mode frequency to yearly temperature variation.

and 3rd mode result of this process in histogram format for frequency and damping. Frequency and damping are fit to normal and log-normal distributions, respectively, as seen in Figure 2-13. The poor fitting of mode 1 and mode 2 can be explained by temperature sensitivity.

Environmental influence (especially temperature) on modal parameters has been shown in several studies [27, 34, 122-124]. The TRB is also significantly influenced by temperature as it may experience greater than 100°F temperature difference in a year. Figure 2-14 illustrates strong temperature dependence in the 1st mode with frequency changing up to 8% over the year. Strong bi-linear behavior with a pivot point near freezing temperature has also been shown in previous studies [120], attributed to asphalt overlay contributing to stiffness only when below near freezing temperatures; the TRB has no such overlay and demonstrates a much more gradual frequency shift throughout the TRB temperature spectrum, as seen in Figure 2-14.

2.6 Summary & Conclusions

The performance monitoring process for the TRB considers the primary deterioration processes associated with pin and hanger bridges as well as short-to-medium span stringer/multi-beam composite bridges. A top-down sensing strategy for the TRB was developed to monitor specific system behavior to live loads and temperature changes. The monitoring system is implemented in Monroe, Michigan exposed to a cold and overcast winter climate, requiring measures be taken to ensure the survivability of the network for long term deployment. Measures were taken to harden the solar powered wireless system against cold, overcast and wet conditions. A move to commercial solar controllers having low-voltage disconnect significantly improved the robustness of the wireless nodes to winter weather and improved the resilience of the system following long-term bouts of little solar energy. Power savings were realized by implementing a duty cycle power switching scheme on the radio of the *Narada* as well as buffering sensor connections with a MOSFET switch. These efforts reduced power consumption by 95%, significantly extending battery lifetime.

The Telegraph Road Bridge (TRB) instrumentation strategy is intended to extract dense amounts of information relevant to the needs of bridge managers and inspectors using top-down sensor strategies and automated processing tools towards modern preventative and performance-based bridge management. The current system operates extremely reliably with very little periodic maintenance or interaction. Sensor deployment has continually increased since September, 2011 producing approximately 25 GB of raw sensor data. Long-term modal data collected from the TRB is shown along with an automation procedure as an initial demonstration of DAQ and automated processing capability. Significant temperature variation in the primary bending mode (as compared to other modes collected) was shown. Modal parameters are not utilized in this thesis in a damage detection program but are routinely used in the SHM community for vibration-based damage detection schemes (*e.g.,* FE model updating). In Chapter 5, structural monitoring tools and analyses promoted in this thesis are described in detail, utilizing long-term data statistics from strain-based implementations presented in a statistical performance monitoring framework to serve as a convenient decision support tool for bridge managers and inspectors. Classification, regression and anomaly detection tools are implemented to automatically detect relevant loads, handle environmental and operational influences, and provide an objective and data-driven methodology for maintenance decision support.

CHAPTER 3.

COMPRESSED SENSING EMBEDDED IN AN OPERATIONAL WIRELESS SENSOR NETWORK TO ACHIEVE ENERGY EFFICIENCY IN LONG-TERM MONITORING APPLICATIONS

3.1 Introduction

The primary objective of this chapter is to propose a lossy approach of data compression to reduce transmission demand in an operational WSN and reduce its energy demand to enhance system scalability. Compressed sensing (CS) approaches compression with an entirely different framework than traditional compression methods. This approach does not enable higher compression ratios than traditional compression methods, but rather allows one to collect and process much less data prior to transmission. Traditional compression methods, whether lossy or lossless, require complete time-history data before compression can ensue, keeping computational and storage requirements at the sensor high. Compressed sensing [81-83] is an emerging technique which realizes compression at the sampling stage of the data acquisition process through a number of encoded measurements, having the effect of immediately reducing the amount of data handled at the sensor. The caveat to compressed sensing (as well as traditional compression methods) is the requirement that the target signal have a sparse or compressible representation in a known basis. The number of measurements taken is governed by the degree of signal sparsity rather than the signal bandwidth (*i.e.*, Nyquist rate), creating the opportunity for sub-Nyquist sampling. Wireless sensors engaged in CS would require minimal computational and storage capacity by integrating compression directly into the acquisition stage and relying on off-site resources (*e.g.*, at a WSN base station) for signal reconstruction. Given that most power at the wireless sensor is used during transmission [75], a reduction in data will have a positive impact on the power and bandwidth limitations currently associated with field deployed WSN. By reducing the effective sampling rate of a wireless sensor's analog-to-digital (ADC) converter and reducing the size of memory required for data storage and computation, CS further enables opportunities for the design of lower power nodes, that have lower costs and smaller footprints (*e.g.*, sensor size, harvester size). An additional advantage to compressed sensing in a wireless setting is the democratic and robust nature of the measurements taken [125, 126]. Essentially, each measurement carries an equally small amount of information about the target signal as all of the other measurements. The effect is that small percentages of packet losses during transmission will not result in large reconstruction errors.

A number of researchers have begun to explore CS for structural monitoring and structural health monitoring (SHM) applications. Bao *et al.* [85] studied the use of CS to compress accelerometer signals from the Shandong Binzhou Yellow River Highway Bridge SHM system. They explored the applicability of CS for cable-stayed bridge acceleration signals. Their study compared compression ratios for CS and traditional compression methods, using Fourier and wavelet bases, as well as static and Huffman coding. They concluded that CS was not very effective in reconstructing the acceleration signals due to a low degree of sparsity in the wavelet and Fourier bases. O'Connor *et al.* [127] explored using CS to reduce power consumption in wireless fatigue life monitoring of ship hulls. The CS implementation accurately reconstructed all but the signal peaks and valleys, thus inducing large errors in fatigue damage estimations. Bao *et al.* [86] explored the use of CS to address data loss common in wireless sensor networks. The authors showed improved signal collection from wireless sensors when compressed measurements are lost rather than time-history samples. These improvements, however, did not improve modal analyses much. Mascarenas *et al.* [84] showed a CS application for SHM damage detection using a laboratory testbed structure with a digital prototype of a compressed sensor embedded into a microcontroller. This implementation samples acceleration in the traditional manner (uniform, Nyquist) and computes compressed measurements on-board as random additions and subtractions of the sampled data. Their demonstration also shows the use of over-complete dictionaries to increase transform sparsity as well as a technique for damage detection performed in the low-dimensional compressed measurement domain by utilizing the smashed filter [128]. Cortial *et al.* [129] studied the use of CS for SHM to reduce the limited communication bandwidth available in sensor networks. In their proposed system, compressed difference measurements between sensed and predicted data is reconstructed at a numerical simulator and further processed for damage detection and computational model updating. Haile *et al.* [130] studied the use of CS in SHM for damage detection in composite materials. Their study exploits the sparsity of damage perturbations to reconstruct full-field strains from a limited number of sensors. Of relevance here are also studies in CS for networked data, typically exploiting correlations in network signals [131-133]; however, compression and reconstruction is limited to single sensor data in this body of work. Researchers in SHM are now beginning to develop wireless sensors having embedded CS sampling abilities that do not require large storage and computational ability so that they are more appropriate for resource constrained field deployments. This chapter describes one such implementation, utilizing traditional sampling hardware to acquire compressed measurements. More recently, Bao *et al.* [134] demonstrated CS sampling on the Imote2 wireless sensor using a random demodulator. Their implementation was validated on the Songpu Bridge in Harbin, China, and shown to be successful towards CS-based data loss recovery.

The study presented here is unique from the current literature by its implementation for field deployment. To the best of our knowledge, this is the first example of CS in a long-term WSN deployment for operational structural monitoring. This implementation realizes primary motivations for CS in SHM: energy efficiency and data reduction in power and bandwidth constrained systems. Long-term applications benefit from the power and data reductions realized by CS as most remote wireless applications run on battery power. The work in this chapter shows the positive impact that CS has on long-term health of WSNs. Most of the current literature quantify the accuracy of signal reconstruction only. The work in this chapter shows quantified energy savings and the impact of CS on battery levels and communication reliability for a long-term deployed WSN. Our implementation has been deployed since December, 2012, collecting and transmitting compressed measurements from five sensor nodes [135]. Second, this is among the first structural monitoring wireless sensors with true compressive sampling (*i.e.*, no digital processing is required to produce compressed measurements) embedded and field deployed. Compressed measurements in most of the current SHM literature require custom sampling hardware or digitally computed linear combinations of the full length signal. Here, a thoughtful implementation of CS sampling allows the use of traditional sampling hardware, making this study an easily repeatable example for researchers hoping to benefit from CS power and bandwidth reductions in field-deployed WSN's. Compressed measurements are taken as arbitrary time-history samples of actual bridge acceleration response, temporarily stored in memory and transmitted wirelessly. The CS strategy advocated does not require custom sampling hardware, significant on-board storage nor the execution of potentially large matrix operations by the wireless sensor microcontroller.

To evaluate the intrinsic trade-off of compression versus accuracy, emphasis is placed on quantifying the quality of reconstruction in terms of the downstream results rather than the target signal underlying the compressed measurements. Specifically, the figure of merit used in this work is the accuracy of the modal parameters extracted from CS reconstructions as compared to conventionally obtained modal parameters. Mode shapes are extracted from acceleration data collected at five bridge locations using the Frequency Domain Decomposition (FDD) method [136]. The CS procedure described here is the first field use of CS for infrastructure monitoring to the best of our knowledge, operating on field-deployed wireless sensors with compressive sampling routines embedded on-board. The sensing system is rid of off-site simulations or extensive on-board computations for obtaining compressed measurements, resulting in efficient sampling and actual energy and transmission reductions in the field-deployed monitoring system.

The compressive sampling scheme is embedded into five *Narada* wireless sensors [51] installed on the Telegraph Road Bridge (TRB) [137]. The existing wireless network includes fifteen *Narada* wireless sensors measuring bridge acceleration. The five CS sensor nodes are collocated with five of the fifteen existing sensor nodes as shown in Figure 3-1. Randomly sampled sub-Nyquist measurements from the CS nodes are transmitted back to a central server and reconstructed using the CoSaMP [138] matching pursuit algorithm. The reconstructed signals are compared to the signals at the collocated sensor performing traditional uniform Nyquist sampling. A comparison is done on the reconstructed time-history signal using a residual sum-of-squares metric, and more importantly done in terms of the downstream results, the mode shapes. The mode shapes extracted from the CS nodes (C1 – C5) are compared with the mode shapes

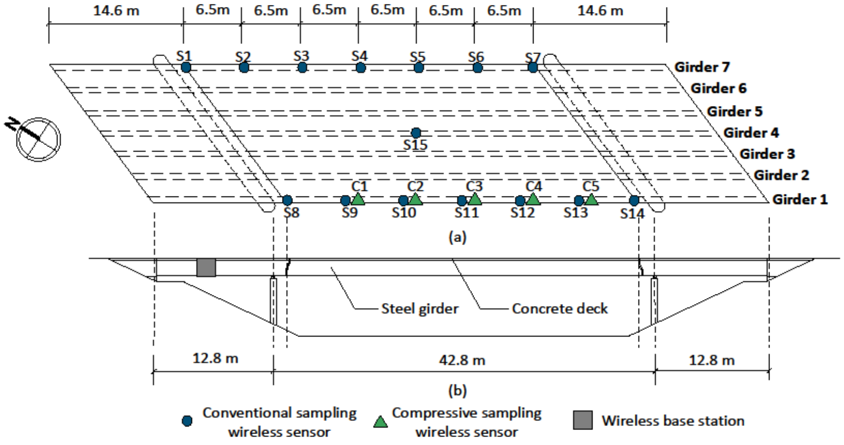

Figure 3-1. Sensor layout on the Telegraph Road Bridge: (a) top view; (b) side view.

extracted from the traditionally sampled nodes (S9 – S13) using the modal assurance criteria [139] (MAC) as the comparative metric. The TRB long-term monitoring effort suffers from the resource constraints described previously, relying entirely on solar power for sustained operations of the sensor network. This makes the TRB monitoring system an ideal candidate for the compressed sensing application and a willing recipient for potential energy savings.

3.2 Compressed Sensing

We consider the problem of acquiring an unknown signal $x \in \mathbb{R}^N$ that we assume to be sparse, or compressible, in a known basis. In our setting, we assume the sensor time-history signal, x, is compressible in the frequency domain. That is, if we express the signal as

$$x = \Theta s \tag{3.1}$$

where $\Theta \in \mathbb{C}^{NxN}$ represents the inverse discrete Fourier transform (IDFT), $s \in \mathbb{C}^N$ is the vector of corresponding Fourier coefficients, such that the nth term of x is:

$$x_n = \frac{1}{\sqrt{N}} \sum_{k=0}^{N-1} s_k \cdot e^{j2\pi kn/N} \tag{3.2}$$

where s_k is the k^{th} term in the Fourier coefficient vector s, then the vector s has only a few large (in absolute value) entries. Two typical acceleration responses from the TRB are shown in Figure 3-2, demonstrating the various levels of compressibility that can occur in a typical structural acceleration signal. Here, the signal in Figure 3-2a corresponds to a signal that is less compressible than the signal in Figure 3-2b. The assumption that x is sparse, or compressible, means that x can be exactly or accurately reconstructed with $k \ll N$ nonzero Fourier coefficients (termed k-sparse). The compressibility of the two signals is observed in Figure 3-2c, which displays the Fourier coefficients in order of amplitude (largest to smallest). Figure 3-2c shows possible k value estimates of the number of relevant coefficients for an arbitrary amplitude threshold at approximately $k = 500$ and $k = 50$ ($N = 3{,}000$) for the signals in Figure 3-2a and Figure 3-2b, respectively.

Traditional compressive techniques take advantage of quick-decaying sorted amplitudes similar to those shown in Figure 3-2c by generally performing the acquisition and compression procedure shown in Figure 3-3a. The full dimension target signal is acquired by uniform Nyquist sampling, where power is consumed proportional to the sampling frequency, and then processed through a transform to its compressible domain. The k most relevant values are selected by keeping all entries with amplitude above some declared threshold and discarding the rest. For a quick-decaying response, only few entries will lie above the threshold value and thus few entries need be kept for accurate reconstruction. In a WSN setting, the compressed signal is then transmitted from the wireless sensor where it is decompressed offline. The disadvantage of this procedure, particularly in a WSN where power and computational resources are limited, is that full dimensional storage and operations of the target signal are required before transmission, greatly increasing memory requirements and computation time for large signal transformation at the sensor node. Also, an algorithm to identify the salient parts of the signal (*i.e.*, the Fourier amplitudes above the threshold) prior to transmission is required as these methods are signal dependent.

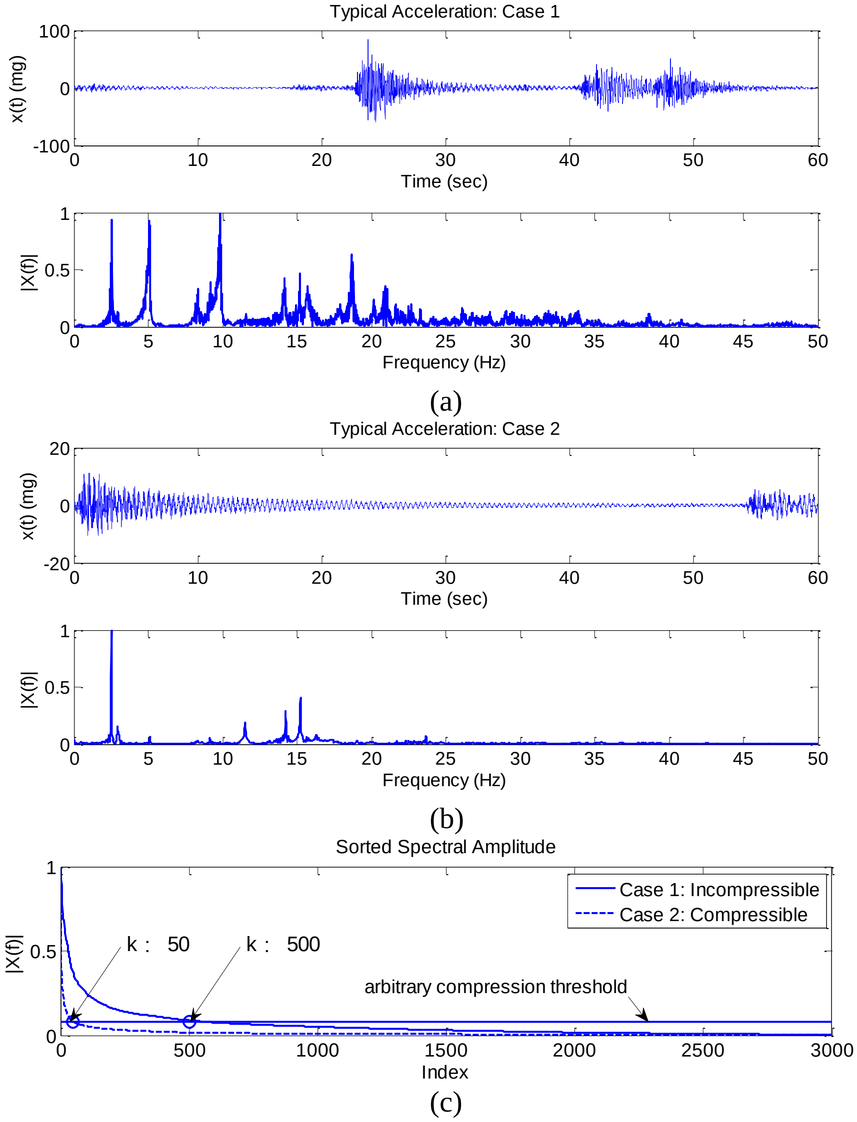

Figure 3-2. Typical acceleration signals from the Telegraph Road Bridge: (a) case 1 time, frequency response; (b) case 2 time, frequency response; (c) case 1, case 2 sorted frequency amplitudes w/ approximate sparsity levels

Instead suppose that it is possible to reconstruct x from a small number of linear, nonadaptive measurements, $y \in \mathbb{R}^M,\ k < M \ll N$. Initial work by Candès *et al.* [81], Donoho [82] and Candès and Tao [140], among others, showed that exact or approximate reconstruction is possible conditioned on the construction of the measurement vector y. This type of compressive sampling enables the general CS procedure as shown in Figure 3-3b. This strategy is not subject to the storage and computational disadvantages associated with traditional compression and is also signal independent (*i.e.,* it is a general procedure capable of handling *all* sparse signals without the need to identify the salient parts of the signal prior to transmission). Rather than *sample* the full dimensional signal followed by a transform and thresholding, CS collects *encoded measurements* which collectively contains all of the information in the most relevant parts of the target signal, with the number of measurements M close to k, the signal sparsity level, rather than N, the full signal dimension. Hence, compression is fundamentally built directly into the acquisition process. The M measurements are transmitted from the wireless sensor and reconstructed off-line. The CS procedure avoids memory intensive storage and operation, and also reduces the power consumed by the wireless sensor's analog- to-digital converter.

The linear measurements $y \in \mathbb{R}^M$ can be expressed as:

$$y_m = \langle x, \varphi_m \rangle, m = 1, \dots, M \quad \text{or} \quad y = \Phi x \tag{3.3}$$

where $\Phi \in \mathbb{C}^{MxN}$ is called a measurement matrix, consisting of M rows, φ_m. This represents an underdetermined system of equations, generally ill-posed. However, the assumption that x is sparse or compressible makes the solution feasible [141]. To enable the solution, first, the measurement matrix, Φ, should be designed such that the relevant information in x still exists in the lower dimensional measurements y and that unique k-sparse solutions are possible. Second,

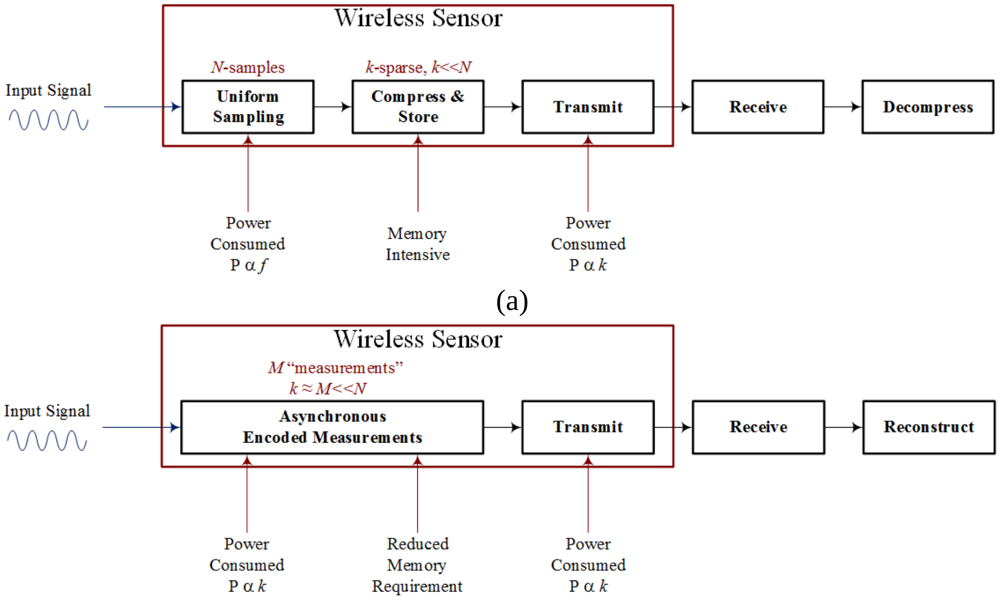

(a)

(b)

Figure 3-3. Acquisition and compression procedure for: (a) traditional compression; and, (b) compressed sensing

an efficient reconstruction algorithm to recover x from y should be designed [142]. By substituting (3.3) into (3.1), the measurements, y, can be observed in terms of the sparse vector, s

$$y = \Phi\Theta s = \Psi s \tag{3.4}$$

One approach to reconstructing s (or x) from y is to seek the sparsest vector s that satisfies $y = \Psi s$:

$$\min_{\tilde{s}\in\mathbb{R}^N} \|\tilde{s}\|_{l_0} \quad \text{subject to } \Psi\tilde{s} = y \tag{3.5}$$

where $\tilde{s}$ represents all possible solutions to s for $y = \Psi s$ and $\|\tilde{s}\|_{l_0}$ counts the number of non-zero entries in each solution, $\tilde{s}$. The difficulty in this approach is that in general, finding a solution is an NP-hard combinatorial problem. However, under certain conditions the solution to

$$\min_{\tilde{s}\in\mathbb{R}^N} \|\tilde{s}\|_{l_1} \quad \text{subject to } \Psi\tilde{s} = y \tag{3.6}$$

can be equivalent to (3.5) , in the sense that both produce an equivalent unique solution [141, 143, 144]. This is significant because (3.6) is a convex optimization problem which reduces to a linear program that is computationally feasible. Regardless of the solution methodology, in order for k-sparse $s \in \mathbb{R}^N$ (signals with only k non-zero entries) to be uniquely recovered from $y \in \mathbb{R}^M$, no two k-sparse vectors can be mapped by Ψ to the same y. The restricted isometry property (RIP) [81] imposes a restricted orthonormality condition on Ψ which enables exact recovery of sparse s from y. The description of the RIP used herein is adopted from Candès [141] with minor variable change to remain consistent with the above formulation. To start, a definition for the k-restricted isometry constant is given in [141, 143, 144] and expressed here.

Definition 3-2.1 (Restricted isometry constants) [141, 143, 144] *The k-restricted isometry constant, δ_k, of the matrix Ψ is defined as the smallest number such that*

$$(1-\delta_k)\|c\|_{l_2}^2 \leq \|\Psi_T c\|_{l_2}^2 \leq (1+\delta_k)\|c\|_{l_2}^2 \tag{3.7}$$

holds for all subsets $\Psi_T \in \mathbb{C}^{Mx|T|}$, with subset $T \subset \{1, \dots, N\}$, $|T| \leq k$ and coefficient sequences $\left(c_j\right)_{j \in T}$. The k-restricted isometry constant shows how close subsets of Ψ (i.e., Ψ_T) are to an orthonormal system when restricted to sparse linear combinations ($|T| \leq k$).

For the case $\delta_{2k} = 1$ in (3.7), $\Psi_T c = 0$ is possible. The subset T can be decomposed into two disjoint sets $T = T_1 \cup T_2$ where $|T_1| = |T_2| = k$ and by populating two zero vectors $s \in \mathbb{R}^N$ and $s' \in \mathbb{R}^N$ with coefficient sequences $\left(c_j\right)_{j \in T_1}$and $\left(c_j\right)_{j \in T_2}$ at the T_1 and T_2 indices of s and s', respectively, the following observation is made

$$\Psi(s - s') = 0 \quad or \quad \Psi s = \Psi s' \tag{3.8}$$

where Ψ is shown to map two k-sparse solutions (s and s') to the same measurement vector y. All k-sparse vectors cannot be uniquely solved for here resulting in the minimum requirement that $\delta_{2k} < 1$ for unique k-sparse solutions to (3.5). The RIP provides the stronger condition that $\delta_{2k} < \sqrt{2} - 1$ to ensure that the solution to (3.6) is that of (3.5) [141] and provides guarantees on the quality of the approximation solution s^* for $s \in \mathbb{R}^N$ in [141] and expressed here.

Theorem 3-2.1 [141] (*Noiseless recovery*): *Assume that* $\delta_{2k} < \sqrt{2} - 1$. *Then the solution* s^* *to*

$$\min_{\tilde{s} \in \mathbb{R}^N} \|\tilde{s}\|_{l_1} \quad \text{subject to } \Psi\tilde{s} = y \tag{3.9}$$

obeys

$$\|s^* - s\|_{l_1} \leq C_0 \|s - s_k\|_{l_1} \tag{3.10}$$

and

$$\|s^* - s\|_{l_2} \leq C_0 k^{-1/2} \|s - s_k\|_{l_1} \tag{3.11}$$

for some constant C_0*, where* s_k *is the best* k*-sparse approximation attainable with knowledge of the exact amplitude and location of the* k *largest entries of* s.

The solution s^* to (3.9) is the minimum l_1-norm of all $\tilde{s}$ satisfying $\Psi\tilde{s} = y$. The quality of the reconstructed signal, s^*, is compared to the actual solution, s, and the very best k-sparse solution, s_k, attainable if the locations and amplitudes of s were known *a priori*. It is observed that if s is k-sparse to begin with, then the recovery is exact [141] (*i.e.*, $s - s_k = 0 \therefore s^* = s$).

A theorem for noisy recovery is also given in [141] (since real sensor measurements are noisy) and expressed here. For measurements with added signal noise

$$y = \Psi s + e \tag{3.12}$$

where e represents the signal noise term, the solution to

$$\min_{\tilde{s}\in\mathbb{R}^N} \|\tilde{s}\|_{l_1} \quad \text{subject to } \|y - \Psi\tilde{s}\|_{l_2} \leq \varepsilon \tag{3.13}$$

where ε is an upper bound on the noise energy, $\|e\|_{l_2}$, stably reconstructs s under the same hypothesis as the *noiseless recovery* theorem [141].

Theorem 3-2.2 [141] (*Noisy recovery*): *Assume that* $\delta_{2k} < \sqrt{2} - 1$ *and* $\|e\|_{l_2} \leq \varepsilon$. *Then the solution to* (3.13) *obeys*

$$\|s^* - s\|_{l_2} \leq C_0 k^{-\frac{1}{2}} \|s - s_k\|_{l_1} + C_1\varepsilon \tag{3.14}$$

with the same constant C_0 *as before and some* C_1 *.*

Candès [141] emphasizes here that C_0 and C_1 are small. For example, when $\delta_{2k} = 0.2$, the error in (3.13) is less than $4.2k^{-\frac{1}{2}}\|s - s_k\|_{l_1} + 8.5\varepsilon$.

Fortunately, selecting a random matrix for Φ satisfies RIP with high probability [142]. Examples include matrices containing Gaussian measurements, where entries of Φ are independently sampled from a normal distribution; binary measurements, where entries of Φ are independently sampled from the symmetric Bernoulli distribution; and incoherent measurements, where Φ is comprised of randomly selected rows of an orthonormal matrix which maps the measurement domain to the sparse domain [145]. The first two largely satisfy RIP for $M = O(k\log(N/k))$. A specific variant of an incoherent sampling matrix is an incomplete Fourier matrix which is used in this work, where Φ is comprised of M rows from the $N \times N$ IDFT selected uniformly at random, resulting in a measurement vector, y, comprised of M time domain samples selected uniformly at random. The wireless sensor simply takes samples uniformly at random as dictated by an embedded pseudo-random number generator triggering the analog-to-digital converter. It has been shown that Φ is sufficiently constructed for $M = O(k(\log N)^4)$ [146], and it is believed that $M = O(k\log N)$. Observing the size of M, it is apparent that x (through s) can be reconstructed from far fewer measurements than the target dimension N, especially for large N and small k.

Several approaches to reconstructing x exist and often prove to be more economical in time and computational complexity than the above mentioned convex optimization solution including greedy pursuits [147-149] and combinatorial algorithms [150-153]. For this study, the iterative matching pursuit recovery algorithm termed CoSaMP proposed by Needell and Tropp [138] is used for signal reconstruction.

3.2.1 CoSaMP Algorithm

CoSaMP is an algorithm for reconstructing the target signal x from measurements y. CoSaMP is well suited for use with noisy measurements. CoSaMP guarantees that the output spectrum is sparse in contrast to a standard linear program (LP) solver which will reconstruct the entire signal. As a result, CoSaMP runs faster than the standard LP solver and provides de-noising that the standard LP solver would not. The acronym CoSaMP stands for Compressive Sampling Matching Pursuit, and is based on orthogonal matching pursuits [147] but also includes other variations for stronger convergence guarantees and faster computation. Specifically, Needell and Tropp [138] establish the following theorem.

Theorem 3-2.1.1 (CoSaMP) [138]. *Suppose that* Ψ *is an* $M \times N$ *sampling matrix with restricted isometry constant* $\delta_{2k} \leq \mathrm{c}$. *Let* $y = \Psi s + e$ *be a vector of samples of an arbitrary signal, contaminated with arbitrary noise. For a given precision parameter,* η, *the algorithm* CoSaMP *produces a 2k-sparse approximation, a, that satisfies*

$$\|s-a\|_{l_2} \leq C \cdot \max\left\{\eta, \frac{1}{\sqrt{k}}\|s-s_k\|_{l_1} + \|e\|_{l_2}\right\} \tag{3.15}$$

where s_k *is a best k-sparse approximation to* s. *The running time is* $O\left(\mathcal{L} \cdot \log\left(\|s\|_{l_2}/\eta\right)\right)$, *where* $\mathcal{L}$ *bounds the cost of a matrix-vector multiply with* Ψ *or* Ψ^*. *The working storage use is* $O(N)$.

The CoSaMP algorithm iteratively extracts the recoverable energy in the target signal. Under the assumption that the restricted isometry constant is much less than one, the multiplication of Ψ^* with the sample vector, y, can serve as a signal proxy in the sense that the largest entries of the proxy correspond to the largest entries of the target signal. The largest $2k$ entry locations are merged into a support set T at each iteration and used to cast a least-squares problem. Only the columns of Ψ corresponding to the support (Ψ_T) and the input sample vector, y, are used to solve for a preliminary approximation of the target signal. The preliminary approximation is trimmed to only the k largest entries to form the current iterations k-sparse solution and the residual vector is updated to reflect the current approximation. The updated residual will enter the next iteration and be evaluated further. The process will continue until a specified halting criteria is met. The algorithm has several potential stopping criteria, including thresholds on iteration count, relative

```
Algorithm: CoSaMP ($\Psi, y, k$)

Required: Sampling matrix $\Psi$, sample vector $y$, desired reconstruction sparsity level $k$
Output: A $k$-sparse approximation $a$ of the target signal

$a^0 \leftarrow 0$                          // initialize approximation vector
$v \leftarrow y$                            // initialize residual as input sample vector
Do
  $l \leftarrow l + 1$                      // iteration counter
  $p \leftarrow \Psi * v$                   // form signal proxy
  $\Omega \leftarrow \mathrm{supp}(p_{2K})$          // identify largest $2k$ entry locations
  $T \leftarrow \Omega \cup \mathrm{supp}(a^{l-1})$  // merge with existing support set
  $b \leftarrow \Psi_T^{\dagger} y$                  // least-squares solution by pseudoinverse
  $a^l \leftarrow b_K$                      // trim to largest $k$ entries ($k$-sparse solution)
  $v \leftarrow y - \Psi a^l$               // update residual
While halting criteria true (e.g., $\|v\|_2 > tolerance$)
```

Figure 3-4. Pseudo code for CoSaMP algorithm, adapted from Needel and Tropp '09

change in residual energy between iterations and total residual energy. CoSaMP uses the assumption of a small restricted isometry constant and algorithmic guarantee that $T \leq 3k$, to establish that Ψ_T is extremely well-conditioned and an iterative pseudoinverse method can be used for the least squares problem. The iterative pseudoinverse application addresses the major obstacle to fast implementation of the CoSaMP algorithm [138]. It can be seen in (3.15) that the performance of the CoSaMP algorithm is influenced by the sparsity level, k, and the signal noise energy, e. In particular, the bound on the residual energy increases as sparsity decreases (tending from sparse towards compressible) and signal noise energy increases. Pseudo code for the CoSaMP algorithm is adapted from Needell and Tropp [138] and is provided in Figure 3-4. The CoSaMP algorithm takes as input the sampling matrix,Ψ, the sample vector, y , and the desired reconstruction sparsity level, k. The output is a k-sparse approximation, a, of the target signal s.

3.3 Telegraph Road Bridge Implementation

The CS nodes installed on the TRB are shown in Figure 3-5 with sensor and solar panel installation. Each sensor is powered completely by a 10W UL-Solar 12V polycrystalline solar panel shown in Figure 3-5a mounted to the southern-most girder (Girder 1 in Figure 3-1). Two main factors were considered during the choice of solar panels: 1) specified peak power and 2) physical footprint. The chosen solar panels serve more than adequate for the summer months but are somewhat challenged during long periods of sustained overcast conditions, quite common during the Michigan winter. Sensor modules are mounted by magnets to the bottom flange of the girder shown in Figure 3-5b. Each sensor module (Figure 3-5c) contains a *Narada* wireless sensor, a solar charge controller based on the Linear Technology LT3652 battery charger, an accelerometer, and a PowerSonic PS-832 8V 3.2Ah sealed lead acid rechargeable battery capable of providing nearly two days of operation when the *Narada* is in active mode and nearly two weeks operation when the *Narada* is in sleep mode with periodic sensing.

A 100 Hz sampling frequency was considered in the TRB monitoring system for the CS study, dictated by signal bandwidth and standard practice. In particular, Figure 3-2a provides an example of significant signal energy manifesting in the 25 Hz range. For the given structural system it has been determined that the acceleration responses at all of the current sensor locations are band-limited to 25 Hz. The Nyquist-Shannon sampling theorem would immediately dictate at least 50 Hz sampling. Exact Nyquist rate is never used in application and significant oversampling is common practice as it reduces the effect of ADC quantization noise and effectively increases resolution. Here, a modest oversampling factor of 2 is used as a fair benchmark to the proposed CS sampling scheme. Sampling rate designs observed throughout the structural monitoring community [61, 63, 154-156] are often even more conservative. Five of the wireless nodes on girder line #1 (Figure 3-1) have compressive sampling routines embedded into their program software, labeled C1, C2, C3, C4, and C5. These units collect acceleration data asynchronously at effective sampling rates well below the 100 Hz rate, and often times below the observed 50 Hz

Nyquist rate. For the purpose of comparison, these sensors are collocated with Narada nodes (labeled S9, S10, S11, S12 and S13, respectively, in Figure 3-1) configured to collect acceleration data in a conventional manner (i.e., uniform sampling governed by the aforementioned a priori defined Nyquist rate).

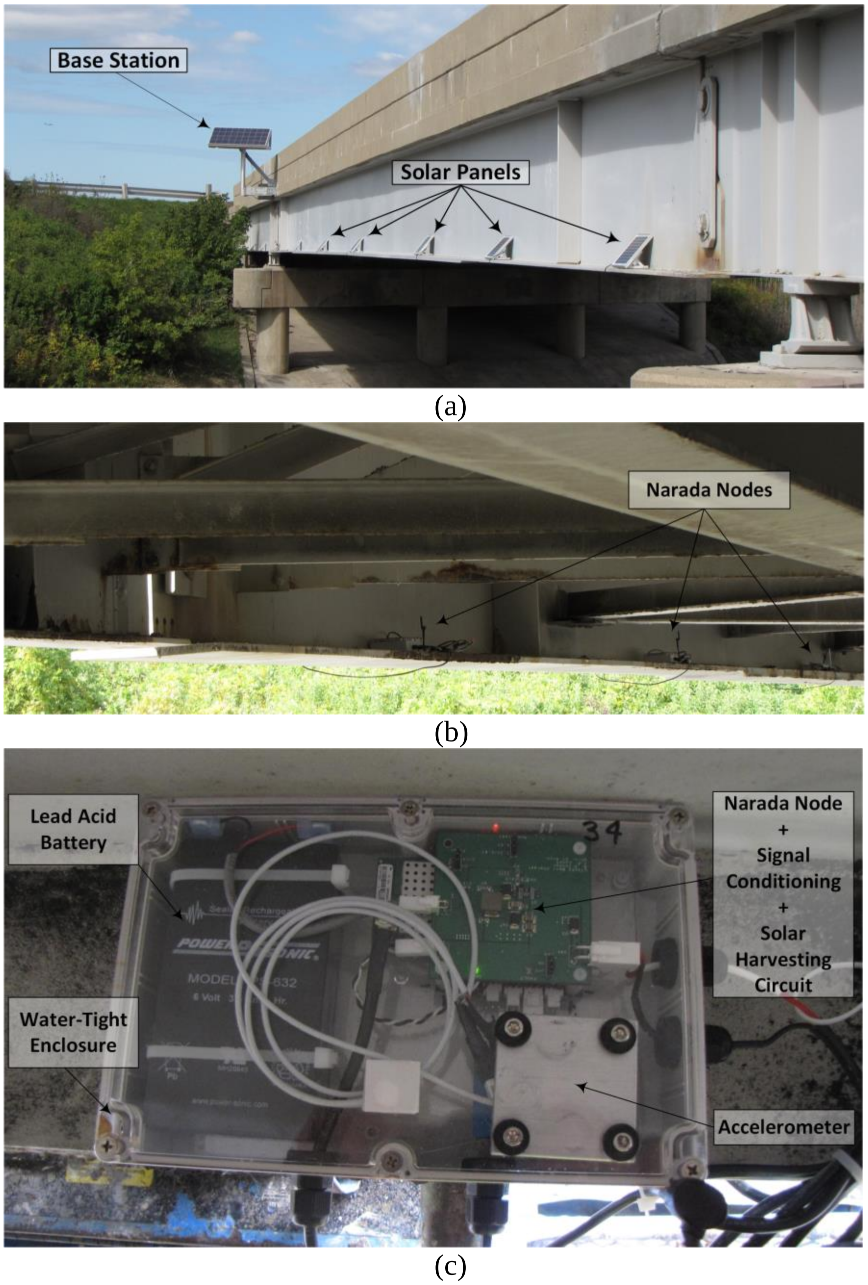

Figure 3-5. Telegraph Road Bridge system installation: (a) solar panels magnetically mounted to the girder flange on the southern exposure; (b) *Narada* sensor nodes magnetically mounted to the girder bottom flange; (c) close-up view of a typical *Narada* sensor module

3.4 *Narada* Compressive Sampling

Low power wireless sensors for structural monitoring are often implemented with limited energy, computational power, and communication payload. In order to reduce the amount of energy consumed at the wireless sensor, the CS procedure is used. The task of developing sampling hardware which can produce random linear measurements on the target signal prior to data acquisition and storage is a large one, which also delays data acquisition until the entire target signal has been realized. A software implementation for computing random projections from uniform samples can become a heavy burden on computational and storage limitations in wireless platforms, requiring target signal dimension matrix operations. When considering a measurement scheme that simply acquires random samples of the target signal rather than linear measurements, traditional sampling hardware can be used with very low computation and storage requirements. To achieve this, the *Narada* takes compressed measurements by randomly triggering the ADC. For comparison, a *Narada* in conventional mode takes uniform samples of the acceleration response at a fixed rate dictated by the signal bandwidth (Nyquist rate) and stores all of the samples in SRAM for future transmission. Figure 3-6 shows the step-by-step signal acquisition and reconstruction procedure implemented on the TRB. This process is summarized as follows:

1) The bridge under vibration induces an analog signal from the accelerometer.
2) The analog signal is digitized asynchronously at the ADC. A linear congruential (LCG) pseudo-random number generator [157] is embedded into the computational core of the *Narada* to dictate which samples are taken. The pseudo-random number generator generates times when the ADC should take a sample. Every clock cycle (using the *Narada* 8 MHz clock), the micro-processor determines if the current time coincides with the LCG

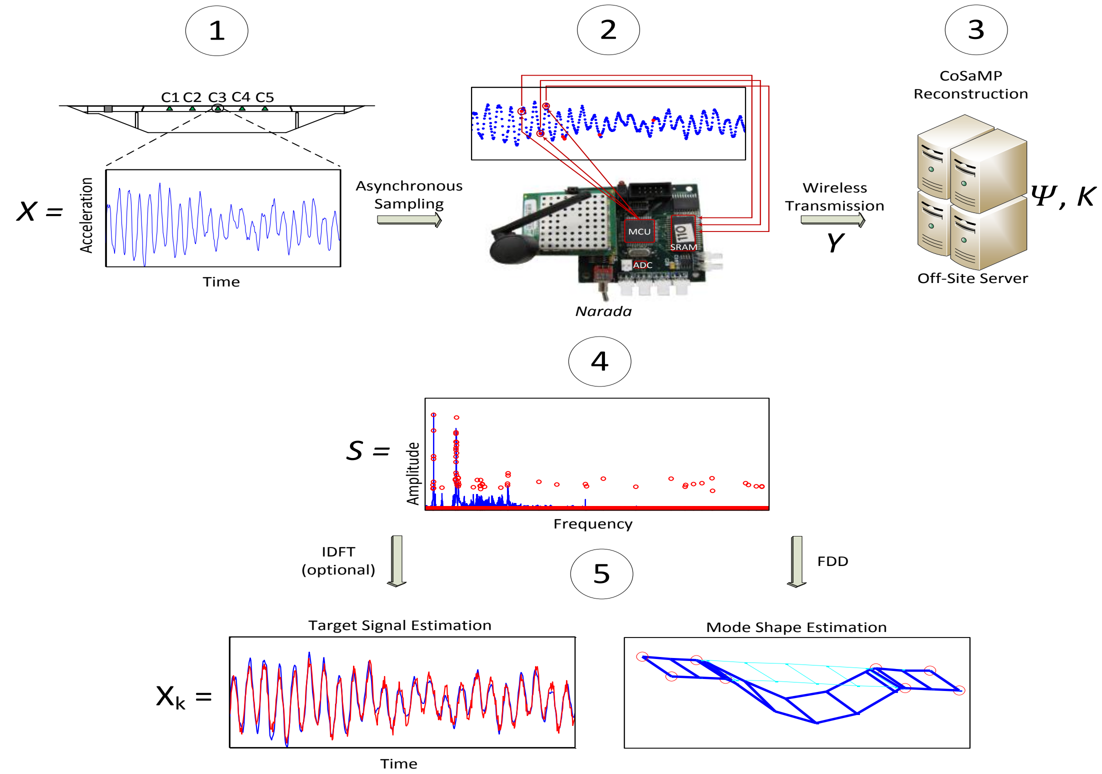

Figure 3-6. Step-by-step compressed sensing procedure: 1) analog sensor response to bridge acceleration; 2) sub-Nyquist random sampling; 3) transmission and off-line target signal reconstruction; 4) resulting CS approximation to target signal; 5) further processing (*e.g.*, time-history, mode shape approximation)

sample time, and acts appropriately on the ADC. The randomly sub-sampled version of the time-history is stored to memory.

3) Only the randomly sub-sampled data, y, is sent through the wireless channel and relayed further off-site to a computational server. The seed and function of the random number generator are known *a priori* and stored here for signal reconstruction. This information is used to build a measurement matrix consistent with the sub-sampled data vector.

4) The received measurement vector, y, the desired sparsity, k, and the pre-programmed measurement matrix, Ψ, are input to the CoSaMP algorithm to obtain the target signal, s, in the sparse domain.

5) The signal, s, is converted back into the time domain, x, through the use of a traditional inverse discrete Fourier transform and processed for mode shape extraction. The conversion back to the time domain is unnecessary for the modal analysis but is done for the purpose of comparison with the traditionally acquired time-history signal.

The inconsistency between theory and practice here should be noted. Pseudo-random sampling is not what the theoretical analysis of CoSaMP calls for. Although, in practice it doesn't matter, one can obtain similar theoretical results with pseudo-random number generators [152]. Figures 3-7a and 3-7c show the acceleration responses for a full one minute time-history sample taken from two of the five accelerometer locations performing compressed sensing. Data collected by conventional sampling at 100 Hz is displayed as a solid blue line. Randomly sub-sampled data at 10% of the original signal dimension (effective 10 Hz rate) are shown by red circle markers. Figures 3-7b and 3-7d show a ten second window chosen from Figures 3-7a and 3-7c, respectively, for a closer view of the compressed measurements being taken. Experimental results are obtained for several levels of compression and reconstruction sparsity. Specifically, the 100 Hz data was sub-sampled at 10%, 20% and 30% and reconstructed using desired sparsity levels of 50, 100 and 150 ($N = 6{,}000$). The sampling method is non-adaptive in that the measurements taken are not signal dependent, which is extremely efficient in this setting. The implication is that a uniform compressed sensing procedure can be implemented for all signal types (and all sensor locations) throughout the sensor network. Random sequences can easily be changed by sending new LCG seeds to the sensor nodes.

3.5 Results

The CS procedure described is intended to result in reduced data and sensor operation and thus ease power and bandwidth constraints. The quality of the reconstruction must be relevant to the end goal of the processing client. Signal reconstruction using the CoSaMP algorithm results in an approximation of complex Fourier coefficients and subsequent mode shape estimation. To assess the quality of the approximation, the metric of residual sum-of-squares (RSS) is used on the time domain representation, x_k, normalized by the traditional Nyquist sampled signal, x, given as

$$RSS = \frac{\|x - x_k\|^2}{\|x\|^2} \tag{3.16}$$

Due to varying load characteristics, RSS is presented for a large set of sensor data using box and whisker plots. The bottom and top of the box represent the first and third quartiles and the interior line represents the second quartile (i.e., the median value). The lower whisker extends to 1.5 interquartile range (IQR) of the lower quartile and the upper whisker extends to 1.5 IQR of the upper quartile, ignoring extreme outliers. Approximately 400 one minute time-history samples at each location were used for analysis; three of the five locations performing compressed sensing are shown in Figure 3-8. Time-history reconstructions were obtained for $M/_N = 0.10, 0.20, 0.30$ and $k = 50, 100, 150$. The expected result is observed; approximation residuals are reduced as the number of measurements, M, and desired reconstruction sparsity, k, are increased, provided M is sufficient for k-sparse reconstruction. For example, in Figure 3-8c, the approximation residuals improve from $k = 50$ to $k = 150$ for 20% and 30% sampled. However, at 10% sampled the

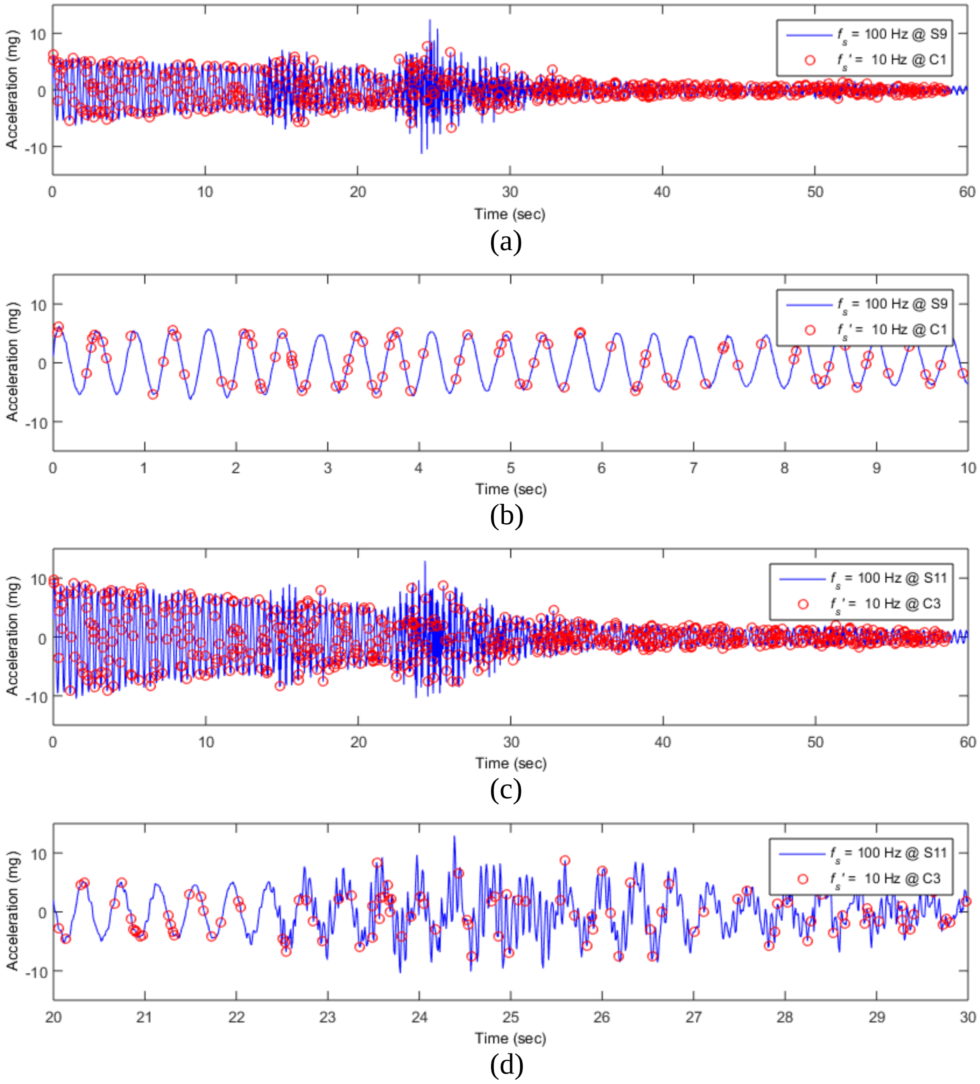

Figure 3-7. Conventional (line) and compressed (circle) data acquisition: (a) S9 versus C1 full time history; (b) S9 versus C1 zoom view; (c) S11 versus C3 full time history;(d) S11 versus C3 zoom view

approximation gets worse as reconstruction sparsity increases, indicating that an insufficient amount of information was acquired in the measurement process. This trend can be expected to continue, as the reconstruction can only be accurate up to as much information is provided in the measurements. Requesting high resolution reconstruction (high k) from insufficient input (low M) forces the reconstruction algorithm to approximate coefficients without sufficient guidance. The

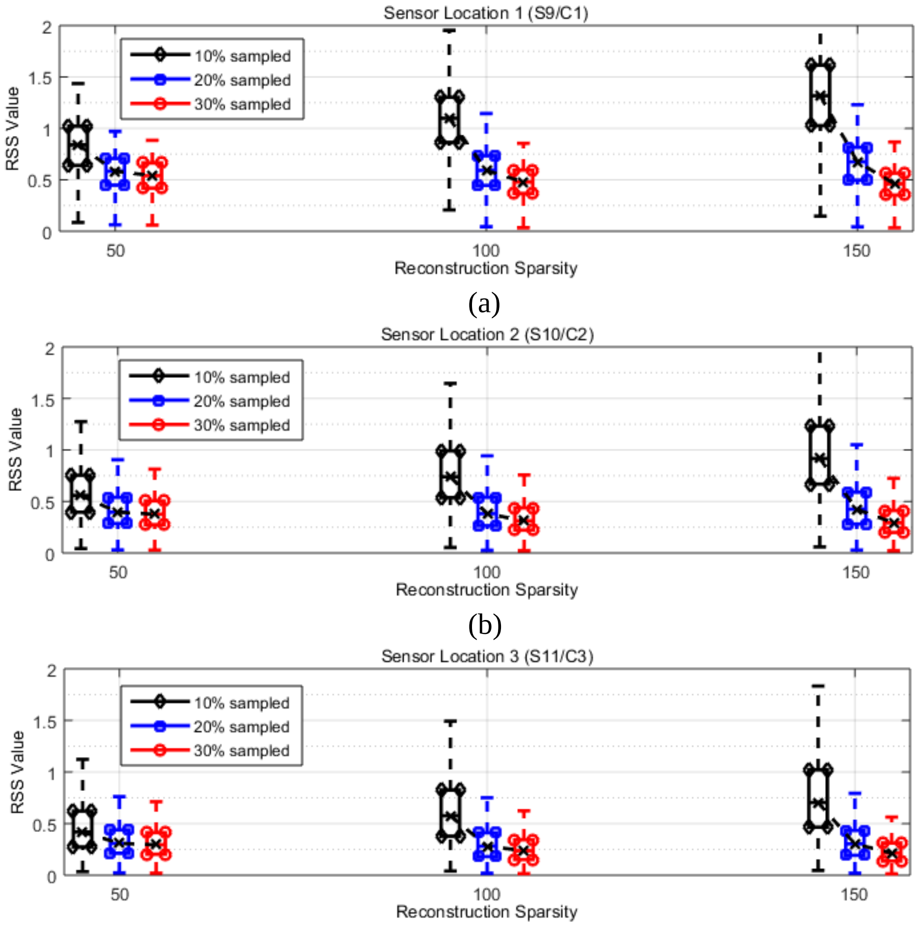
Sensor Location 1 (S9/C1)

Sensor Location 2 (S10/C2)

Sensor Location 3 (S11/C3)

(a)

(b)

(c)

Figure 3-8. Target signal reconstruction quality as measured by residual sum-of-squares (RSS): (a) S9 versus C1; (b) S10 versus C2; (c) S11 versus C3

excess of coefficients having low quality reconstruction contribute negatively to the overall approximation.

Since modal parameter extraction is the intended end goal in this study, it is appropriate to assess reconstruction quality in terms of the modal parameters of interest, specifically mode shapes in this study. The CS reconstructions are processed for mode shapes using the Frequency Domain Decomposition (FDD) technique [136]. Figure 3-9 shows the quality of the mode shape approximation given by the modal assurance criteria (MAC) [139], a measure of correlation between the mode shapes obtained from conventional sensing and compressed sensing. Similar

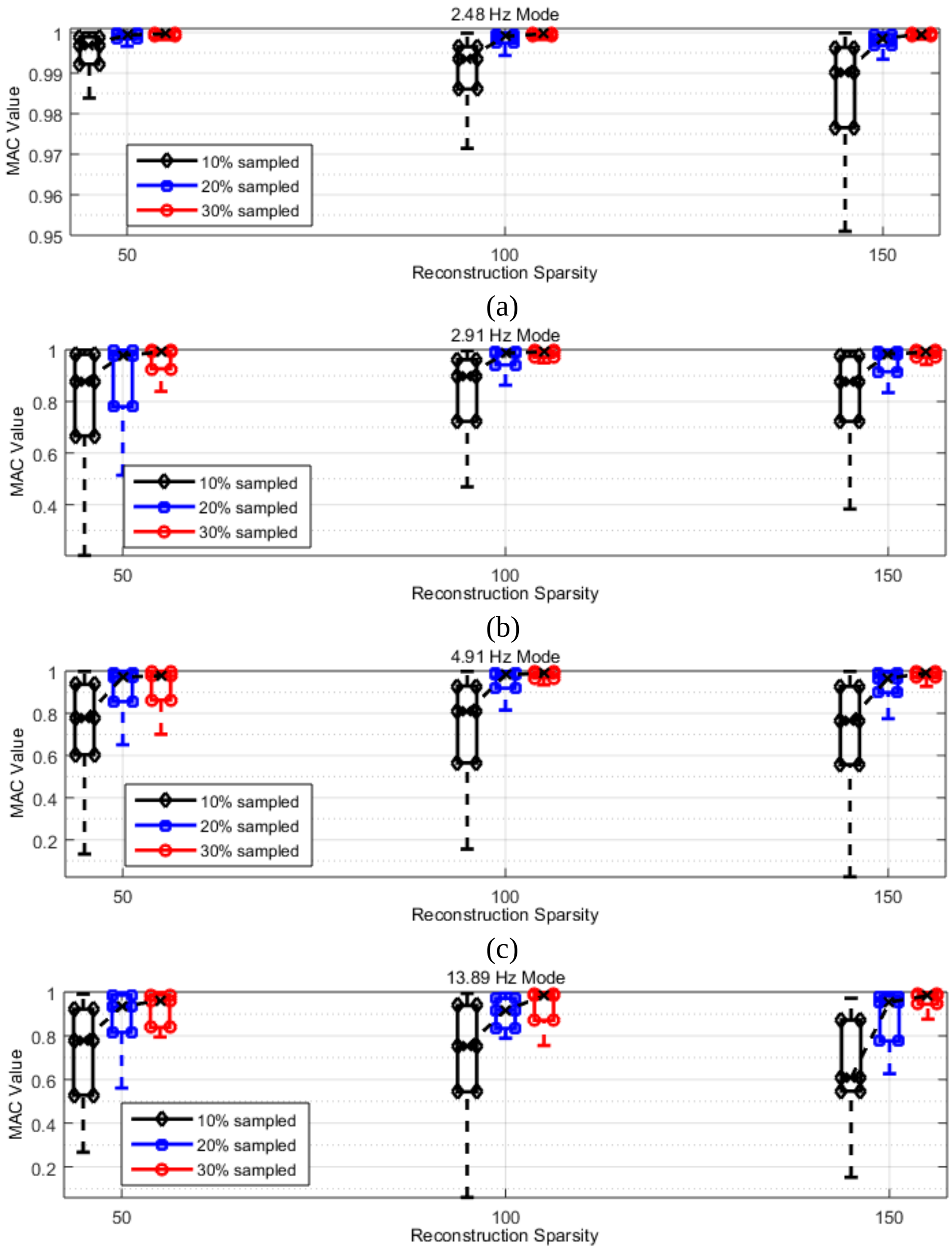

(a)

(b)

(c)

(d)

Figure 3-9. Modal reconstruction quality as measured by modal assurance criteria (MAC): (a) mode 1; (b) mode 2; (c) mode3; (d) mode 4

to the time-history reconstruction, a balance between the number of measurements taken and the desired reconstruction sparsity level is observed. When enough information is present in the lower dimensional measurements, M, there is an increasing trend in MAC value for increased reconstruction sparsity levels. If the desired reconstruction sparsity level is high, and not enough information is present in the measurement vector, coefficient assignment will be inaccurate and start to degrade the approximation. This kind of behavior is evident in Figure 3-9d, where median MAC values increase with reconstruction sparsity level at 30% sampling and decrease with increased reconstruction sparsity level at 10% sampling. If a goal threshold of 0.90 for MAC is made for quality reconstruction, then the first mode is shown to be well approximated with very little effort, as seen in Figure 3-9a. MAC values of approximately 1.0 are observed for all sampling percentages and all desired reconstruction sparsity levels. The energy in the first mode far exceeds the other modes for most loading scenarios, and thus is the easiest to identify by matching pursuit. For all other modes, at least 20% sampling is required for quality mode shape reconstruction, as seen in Figures 3-9b, 3-9c, and 3-9d. Desired reconstruction sparsity levels of $k = 50$ are sufficient for the abovementioned MAC goal. Tradeoffs between computation time and MAC must be made when higher reconstruction sparsity levels are desired.

The assessment of the CS procedure also includes the energy efficiency gained. The reduced sampling requirements and reduced transmission payloads translates into lower energy consumption at the wireless sensor. Figure 3-10 shows the calculated energy efficiency achieved through the compressed sensing implementation on the TRB and the resulting improvement in communication reliability during harsh weather. Figure 3-10a shows the total energy reduction as a function of network size (*i.e.*, nodal count). Total energy calculations include the one minute sampling period, followed by the entire network transmission time. The *Narada* operates in a sleep-mode state during standby periods (*i.e.*, when not collecting or transmitting data) and thus contributes minimally to the total energy consumption between sampling intervals. The TRB sensing program has a 4 hour measurement period that consists of ~4 hours of sleep (sleep mode), 1 minute of sampling (active mode), and a transmission time of 0.76 seconds (Tx/Rx mode) for a

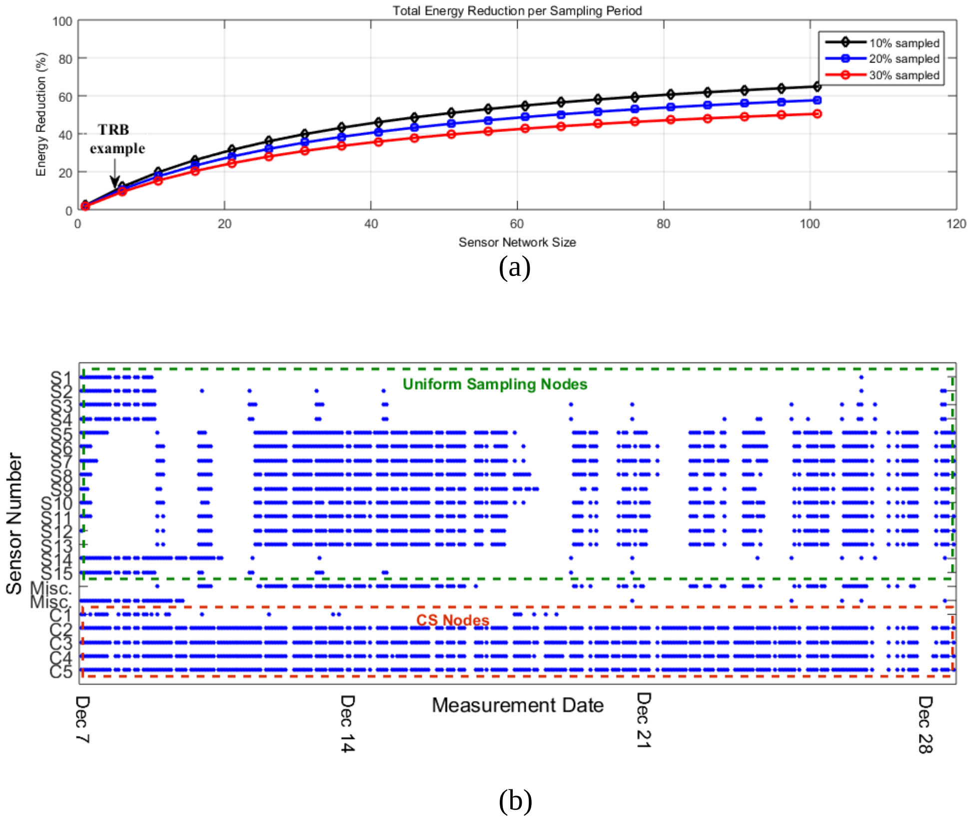

Figure 3-10. Compressed sensing energy efficiency for the TRB implementation: (a) energy reduction as a function of network size; (b) winter weather sensor performance

6,000 point sample from one node. Because of a time division multiple access (TDMA) network protocol used, all sensors remain in a transmit state until all of the network's sensor data is received as they await a network success acknowledgement and the command to re-enter sleep mode from the base station. In this case, the impact of the transmit time increases as the size of the sensor network increases. For the TRB study, five CS nodes were deployed. The energy reduction attained by CS is approximately 8%, 9% and 10% for 10%, 20% and 30% sampled data, respectively. The larger network sizes depicted in Figure 3-10a are estimated using the power consumption of the *Narada* wireless nodes. For low network sizes the overall energy reductions are modest but not insignificant. Figure 3-10b shows *Narada* wireless sensor availability during the month of December, 2012. The energy savings realized by the CS implementation help to make the sensor nodes more sustainable to the cold and overcast Michigan winter conditions. The

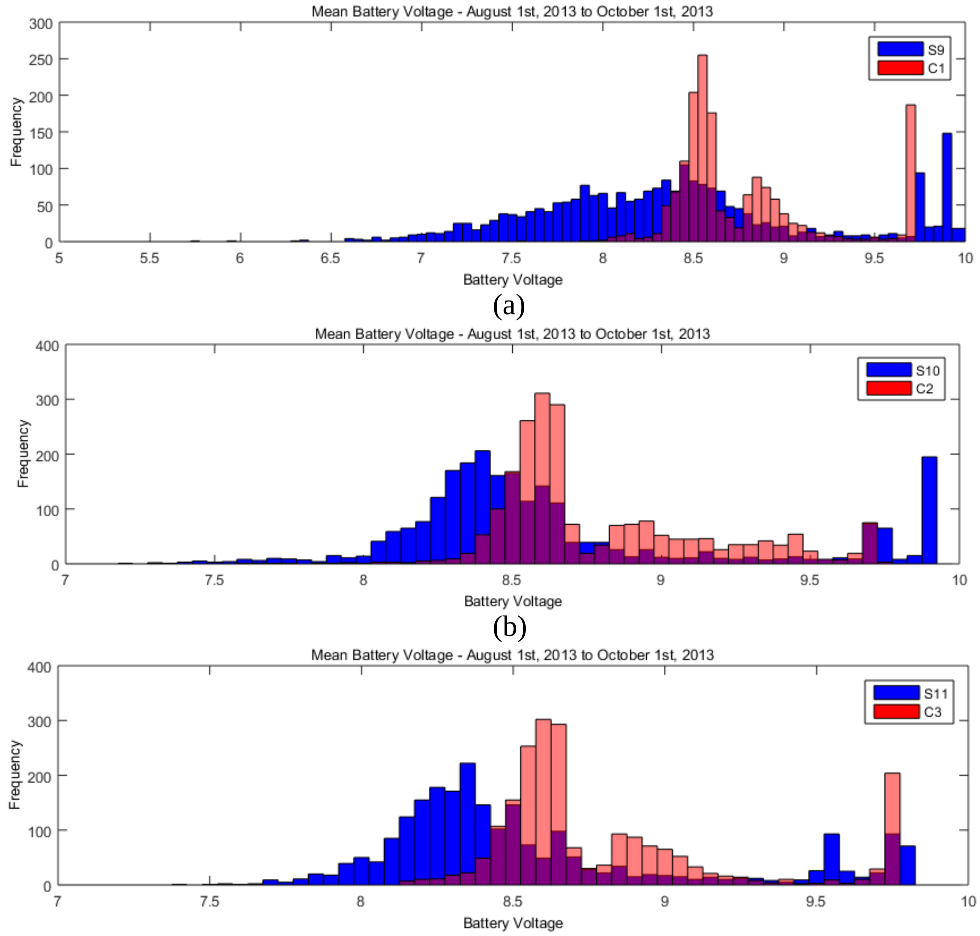

(a)

(b)

(c)

Figure 3-11. Mean battery voltage: (a) S9 versus C1; (b) S10 versus C2; (c) S11 versus C3

figure shows a dot for each successful data acquisition and transmission instance. Blank spaces in the figure signify a failed transmission. It is evident in Figure 3-10b that the CS nodes, labeled C1 – C5, outperform their traditional sensing counterparts, labeled S1-S15 (with the exception of faulty sensor C1), due to higher energy reserves.

These energy savings in the CS nodes can be shown directly by measured battery voltage. In addition to each sensor node collecting acceleration data, the sensors also measure battery voltage. Shown in Figure 3-11 are measured voltages from the 8V sealed lead acid batteries at three of the five paired sensor locations between December, 2012 and June, 2013. Battery voltages from the CS nodes are consistently higher than their counterparts. This figure reinforces the result in Figure 3-10b and demonstrates the direct positive impact that the CS implementation has had on the TRB monitoring system, and the real importance that the reported implementation can have on system reliability for resource constrained systems.

3.6 Conclusions

In this chapter, a CS strategy is proposed for energy efficiency in wireless sensors engaged in monitoring operational structures. The CS implementation is embedded into five wireless sensors on the TRB monitoring acceleration. The reconstructed acceleration responses are used to approximate modal parameters (*i.e.,* mode frequency and shape). MAC values above 0.90 are obtained for all four bridge modes shown when the CS procedure operates with at least 20% sampling. The goal of reducing the amount of data through the wireless channel is achieved at a cost of modal accuracy. A lack of strong sparsity in the acceleration signals limits the potential of the CS procedure for drastic compression. Energy reductions are shown to be significant in the TRB structural monitoring system for large sensor networks and have improved battery health. The energy savings realized by compressed sensing via reduced transmission payload are also achieved through traditional compression techniques. However, several aspects of the compressed sensing framework are attractive and should be considered. First, the immediate reductions in data collected on-board the wireless sensor results in lower computational and storage needs which may enable the design of very low power nodes. Second, the compressed sensing procedure is non-adaptive, meaning that a uniform compression procedure can be implemented at all sensors for all signals (assuming they are compressible), and reconstructed in a uniform manner. Third, the democratic and robust nature of the measurements increases the reliability of the wireless network against random packet losses since all measurements contain a relatively equal amount of information about the underlying signal.

CHAPTER 4.

EMBEDDED FATIGUE LIFE MONITORING IN WIRELESS SENSORS FOR ENERGY EFFICIENCY AND SCALABILITY

4.1 Introduction

Structural failures where fatigue damage has been cited as the root cause are widespread throughout modern history spanning from the Versailles train crash in 1842 to the more recent destruction of China Airlines Flight 611 aircraft in 2002. Fatigue damage is induced under cyclic loading which causes an accumulated degradation of the subjected material, leading to eventual fracture at points of stress concentration. The progressive nature of fatigue damage lends itself well to structural health monitoring applications (SHM). If the application proves itself reliable, it can provide an invaluable tool towards structural management procedure (i.e., maintenance and inspection) as well as forewarning of pending structural failure. Fatigue damage is of specific concern to the Navy today in their efforts to incorporate aluminum into hull structures for high performance speed and maneuverability [158]. High performance aluminum in the ship hull will lead to higher incidences of fatigue cracking [159] and once cracks initiate they will grow much faster in aluminum than in steel [160]. Not only is a reliable tool necessary to quantify fatigue damage, but also a means of high density deployment without sacrificing sensitive design criteria such as hull weight. Fatigue “hot spots”, or points of stress concentration, may be easy to predict but many locations exist throughout an entire hull structure. Traditional tethered monitoring may not be feasible due to the high costs of extensive cabling and installation labor (as well as the obtrusiveness of wiring) [39]. Therefore, a decentralized wireless structural health monitoring system is proposed to meet the challenges associated with centralized tethered systems. Numerous wireless sensing platforms have emerged in the last decade for SHM [72]. Wireless sensors combine the functionality of data acquisition, analysis, and wireless transmission within a single device. Among their many advantages, wireless sensing channels can be installed at a fraction of the cost of a wired channel. This allows dense sensor networks to be affordably deployed throughout large structural systems. This affordability increases the reach of the system to a larger set of users since cost is almost always a main parameter when deciding to monitor a structure or not. Another advantage of wireless sensors is that they are capable of processing data locally. Directly transmitting massive amounts of raw strain data via wireless sensing would consume the limited communication bandwidth available and result in significant power consumption during communication.

In Chapter 3, a data compression approach for WSNs was proposed as a generic raw data compression procedure to be fully reconstructed and analyzed after the compressed data has been transmitted to a more resource plentiful location. The primary objective of this chapter is to take advantage of embedded computing available on-board wireless sensors for the specific SHM purpose of fatigue assessment, retaining strain cycle information relevant to fatigue analyses in lieu of raw strain sensor time-history information; the time-history information is permanently discarded. A strategy for fatigue life estimation by a WSN installed in a structure for autonomous health monitoring is proposed. Decentralized RFC [161] and Dirlik [162] procedures are embedded in a wireless sensor network to convert raw time-history strain response into cycle information (mean and amplitude), producing a more meaningful and compressed form of the original time-history data. Cycles are stored on-board a wireless sensor in external memory in the form of a histogram, providing fixed *a priori* knowledge of memory requirements and allowing for long-term monitoring without a requirement for frequent data transmission. Histograms are continuously updated with cycle information in real-time, ready for transmission any time at the system end-users request. Huge power savings are realized by this point, as the wireless radio is responsible for consuming more power than any other hardware component [75]. The RFC method first introduced by Matsuishi and Endo [161] is a continuous time domain approach which converts a variable amplitude load history into a number of constant amplitude events. The Dirlik [162] procedure is a periodic frequency domain approach, embedded as an alternative more appropriate for stationary signals. Periodic approaches reduce data acquisition and analysis effort. The Dirlik procedure is based on spectral moments computed from the strain response power spectral density (PSD). Spectral moments are considered constant for the length of the period, so a sense of stationarity is important in selecting the length of the period. The output of the Dirlik procedure is a stress range probability density function (pdf), resulting in stress cycle information as before with the RFC procedure. Again, cycle information or cumulative damage is stored on-board the wireless sensing unit requiring transmission only upon user request. The proposed embedment of the RFC and Dirlik procedures address two major constraints in wireless networks; power consumption and transmission bandwidth.

The embedded system is validated by two experimental investigations. In an effort to verify the accuracy of the embedded RFC procedure, an aluminum bar specimen is cyclically loaded in a closed-loop electrohydraulic load frame. A strain gage attached to the aluminum specimen provides strain-time data to both a wired and wireless data acquisition system. Data acquired by wired means is processed off-line after testing as a single time-history. In contrast, wireless data is periodically processed on-board the wireless sensor and stored cumulatively in an on-board histogram. Results from the wired system processed in MATLAB are compared with the wireless system processed on-board using the one-pass rainflow algorithm provided by Downing and Socie [163] that allows for real-time RFC without the need to rearrange the time-history data prior to cycle extraction; this makes for a convenient embedded routine. Second, experimental tests are conducted on an aluminum hull stiffened element specimen as part of the Monitored Aluminum Hull Integrity (MAHI) test program. Testing is carried out at the Naval Surface Warfare Center, Carderock Division (NSWCCD) structures laboratory. Among the major focuses of the MAHI test program are the demonstration and evaluation of SHM technologies. A tethered strain gage monitoring system with 16 channels is employed for laboratory data collection. A network of *Narada* wireless sensors [51] is used to collect 12 strain gage channels performing continuous data collection as well as the embedded RFC and Dirlik procedures. Comparisons are made between the *Narada* wireless data and NSWCCD data. Embedded fatigue validation was limited to the MAHI specimen as TRB strain gages serve multiple functions (*e.g.*, neutral axis estimation, hanger bending, etc.). In addition, the MAHI testing combined with the small-scale University of Michigan laboratory testing showed sufficient validation results.

4.2 Fatigue Life Analysis

The fatigue life procedure employed here is illustrated in Figure 4-1. Strain response data from an operating structure is acquired by a data acquisition system and submitted for RFC or PSD processing. The result is a stress cycle representation; either a histogram format or a probability distribution format. A stress-life relation is used to determine the amount of incremental damage done by each individual stress cycle, and then individual damages are summed according to the Palmgren-Miner linear damage approach.

Many methods exist for extracting cycles from complex load histories including RFC [161], range pair counting [164], and racetrack counting [164]. These methods are designed to transform a complex load history into a number of constant amplitude events that can be easily applied to some stress/strain-life relation. Rainflow counting has shown to be among the best methods for extracting cycles from these variable amplitude load histories and is chosen as the method for embedment here. The RFC method has been shown to accurately extract closed hysteresis loops from the stress-strain domain. The more traditional way to view cycle extraction is to turn the strain-time history vertically to give the look of a Pagoda roof. The manner in which "rain" would "flow" down the roof describes the cycle extraction, given formally by the following rules (for rain flowing towards peaks/valleys, the same rules apply) [161]:

a) rain flow stops if it meets an opposing peak/valley origin larger than its own

b) rain flow stops if it meets the path of another flow starting form an origin larger than its own

c) rain flow stops at the end of the time history

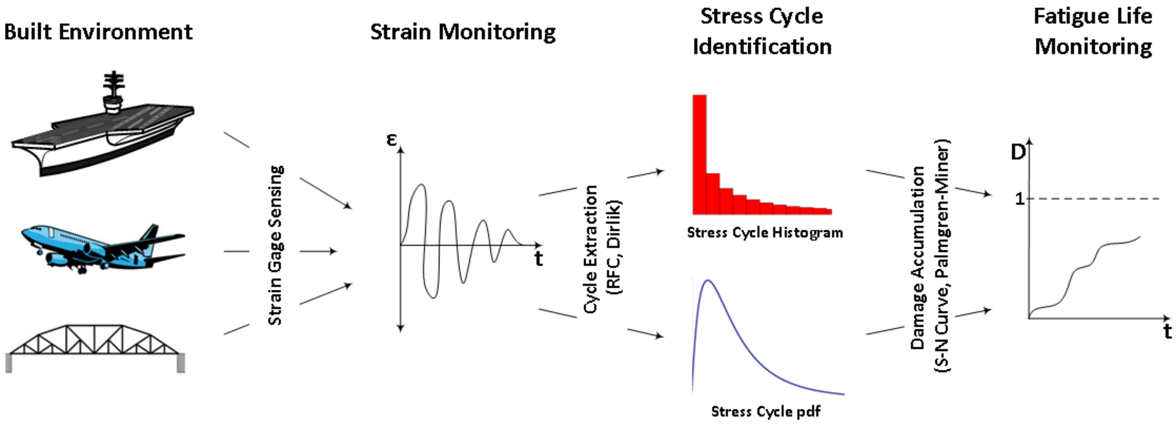

Figure 4-1. Illustration of fatigue life procedure used in this study for embedment into a decentralized wireless monitoring system

Figure 4-2 shows a strain response viewed vs. stress and vs. time and an example of cycle extraction. Original algorithms developed for RFC require the analysis to begin at the maximum peak or minimum valley of the time history. More suitable algorithms for on-line data processing do not require the entire load history or the rearrangement of the load history, allowing data to be processed exactly how it is acquired [163, 165]. One such algorithm is the "one-pass" RFC algorithm, developed by Downing and Socie [163] and modified later by Okamura, *et al*. [166] to account for half cycles. The "one-pass" algorithm allows for analysis to begin at any point in the time history, allowing cycle extraction processing to begin as soon as some specified size time history strain data is recorded.

In Figure 4-2a, ranges AD, CB, GH, and FE are identified as closed loops in the stress-strain response and are recorded as cycles. Regarding the Figure 4-2b point of view, the horizontal distance that each rain flow travels represents a half-cycle of a constant amplitude event. Half cycles of the peak and valley sides of the same range are paired as a complete cycle of a constant amplitude event. Applying this methodology towards Figure 4-2b, complete cycles for ranges AD, CB, GH, and FE are again produced. Significant data compression is achieved when converting time-history strain data to a number of constant amplitude events. Since only the turning points are retained, a significant amount of compression is realized during peak-picking alone (assuming the signal has been filtered for high frequency noise). Histogram cycle storage architecture provides *a priori* memory allocation for continuous cycle accumulation without the need for transmission. Whenever a cycle is identified, it is extracted from the data and logged in the appropriate histogram bin.

Since many loading environments arise as stochastic processes (live loads, wind, waves), it is sometimes more appropriate to use a statistical function to describe operational loading. The main motivation here is to use only a few statistical parameters from the response PSD to estimate fatigue life rather than doing continuous cycle counting in the time domain. Many results exist for the case of narrow band stationary and ergodic random signals [167, 168], most likely having a Rayleigh stress range distribution; however, a procedure capable of handling wide band loading is desired. The Dirlik [162] approach provides a closed form expression linking any given power spectral density (PSD) to a probability density function (pdf) of rainflow ranges when the random process is stationary and ergodic. The Dirlik formulation was derived using a Monte Carlo approach to generate stress time histories from various PSD shapes. Time domain RFC was subsequently performed and resulting probability density functions of rainflow ranges were linked to the corresponding PSD shape. Dirlik's solution is thus empirically derived by fitting rainflow range distributions to simulated data and is technically restricted to Gaussian processes. Theoretically based solutions exist under certain conditions, e.g., Bishop and Sherrat [169]; However, Dirlik's method remains among the most frequently employed techniques due to its simplicity in implementation and accuracy under its required conditions.

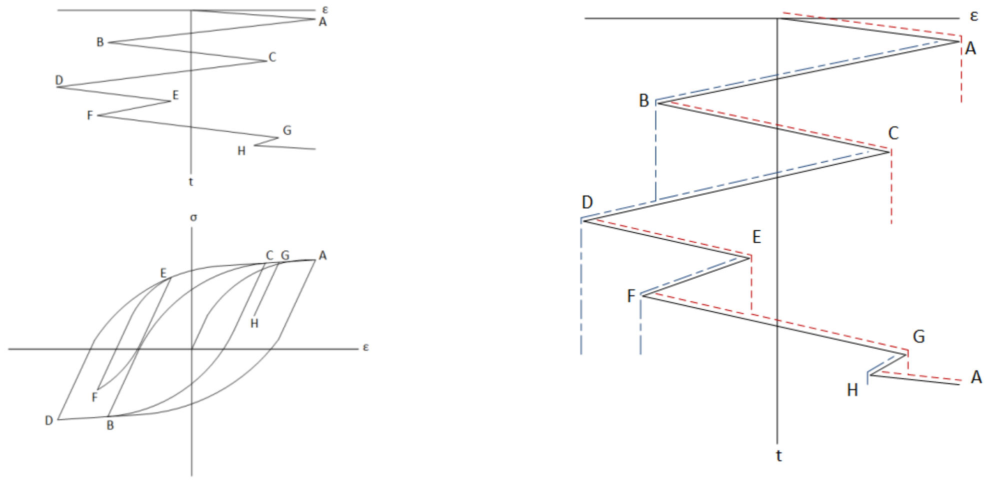

(a) (b)

Figure 4-2. Cycle identification via rainflow counting methods (a) closed hysteresis loop analogy (b) pagoda roof analogy

The brunt of the computation in this procedure lies in the Fourier transform which is embedded in the computational core of the *Narada* wireless sensor. From the Fourier representation, a PSD estimation is made using Welch's method of averaged periodograms [170]. In the Dirlik formulation, the PSD is the base of the analysis. Specifically of interest are the spectral moments, m_n, where the n^th^ moment is defined as

$$m_n = \frac{1}{\pi}\int_0^{\infty} \omega^n G(\omega) d\omega \tag{4.1}$$

or, in the case of a discrete PSD

$$m_n = \sum_{f=0}^{F_{max}} f^n G(f) df \tag{4.2}$$

where $G(f)$ represents the 1-sided power spectral density at frequency f. An illustration of a spectral moment calculation is given in Figure 4-3. Many probabilistic characteristics of the strain signal arise from these moments. In 1945 Rice [171] provided the relationship for the number of upward zero crossings and peaks per second based solely on spectral moments, paving the way for a fatigue life estimation based on power spectral density. The relations are seen below as expected number of zero crossings per unit time, λ_0:

$$\lambda_0 = \sqrt{\frac{m_2}{m_0}} \tag{4.3}$$

expected number of peaks per unit time, μ:

$$\mu = \sqrt{\frac{m_4}{m_2}} \tag{4.4}$$

and irregularity factor, γ:

$$\gamma = \frac{\lambda_0}{\mu} = \sqrt{\frac{{m_2}^2}{m_0 m_4}} \tag{4.5}$$

Irregularity factor is the measure of expected ratio of zero-crossings to peaks, approaching zero for the wide band case and one for the narrow band case. Other important characteristics arising from the spectral moments include

rms, σ_X:

$$\sigma_X = \sqrt{m_0} \tag{4.6}$$

and mean frequency, X_m:

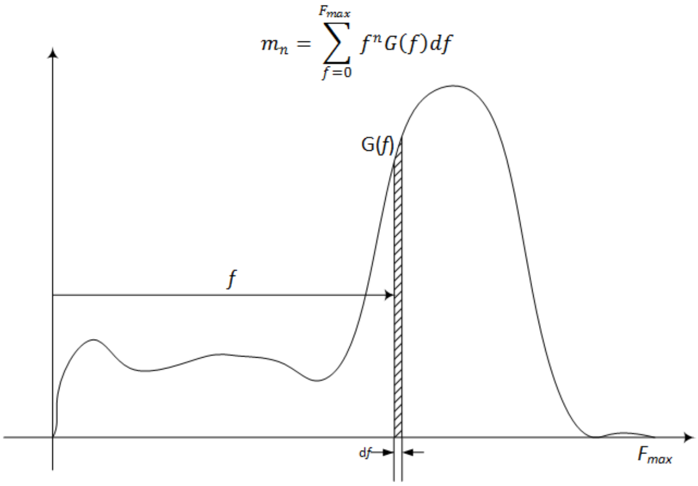

Figure 4-3. Illustration of discrete spectral moment calculation

$$X_m = \frac{m_1}{m_0}\sqrt{\frac{m_2}{m_4}} \tag{4.7}$$

From the above variables, Dirlik's rainflow – range probability density function, P_{RR}, is given as:

$$P_{RR}(z) = c_1 \frac{1}{\tau} e^{-z/t} + c_2 \frac{z}{\alpha^2} e^{-z^2/2\alpha^2} + c_3 z e^{-z^2/2} \tag{4.8}$$

where

$$z = \frac{x}{2\sigma_x} \tag{4.9}$$

$$c_1 = \frac{2(x_m - \gamma^2)}{1 + \gamma^2} \tag{4.10}$$

$$\alpha = \frac{\gamma - x_m - {c_1}^2}{1 - \gamma - c_1 + {c_1}^2} \tag{4.11}$$

$$c_2 = \frac{1 - \gamma - c_1 + {c_1}^2}{1 - \alpha} \tag{4.12}$$

$$c_3 = 1 - c_1 - c_2 \tag{4.13}$$

$$\tau = \frac{1.25(\gamma - c_3 - c_2)}{c_1} \tag{4.14}$$

The probability density function, P_{RR}, gives the empirically derived RFC distribution from the measured PSD.

4.3 Palmgren-Miner Damage Accumulation

The Palmgren-Miner damage hypothesis [172] is a linear damage accumulation strategy for summing the individual effects of stress cycles. The Palmgren-Miner approach does not consider cycle mean or cycle sequence, although many times these assumptions are acceptable given the ease of implementation. Each cycle recorded is associated with some amount of cycles to failure, N_f, by way of some chosen stress/strain-life relation, typically a readily available S-N curve. Palmgren-Miner accumulation considers a normalized amount of damage induced by each cycle to be equal to $D_i = \frac{1}{N_f}$, and assumes failure occurs when $\sum_i^n D_i = 1$ for n cycles. Failure here is considered the onset of a fatigue crack; the method is not valid for crack propagation.

For the RFC procedure, a stress-life relation that includes mean stress effects is used. The linear log-log form of the Wöhler fatigue-life relation, or S-N curve, is given as

$$N = \frac{K}{S^b} \tag{4.15}$$

where N represents cycles to failure at stress amplitude S, and K, b are material constants obtained through experimental testing. Since the RFC procedure used on the *Narada* also retains mean information, the modified Goodman relationship [173]

$$\frac{\sigma_a}{\sigma_{ar}} + \frac{\sigma_m}{\sigma_u} = 1 \tag{4.16}$$

is used to account for mean stress, where σ_{ar} is referred to as an *equivalent completely reversed stress amplitude*, expected to cause the same fatigue life as stress amplitude, σ_a, at mean stress, σ_m. Substituting the equivalent stress, σ_{ar}, for S in (4.15), the corresponding fatigue life is calculated. The fatigue life corresponding to each calculated equivalent stress is an indication of the amount of damage induced in the specimen. The Palmgren-Miner damage hypothesis sums the damage incurred by each stress cycle in a linear manner seen below as

$$D = \sum_{i=1}^{k} \frac{1}{N_i} \tag{4.17}$$

where

$D =$ accumulated damage

$k =$ total number of cycles in a loading spectrum

$i = i_{th}$ applied stress/strain level

N_i = number of cycles to failure at stress/strain level i

For the Dirlik procedure, expected damage can be calculated for any kind of S-N relation by the expected damage per unit time, $E(D)$:

$$E(D) = \mu \int_{0}^{\infty} \frac{1}{N(S)} P_{RR}(S) dS \tag{4.18}$$

where $N(S)$ is the number of cycles to failure for a stress range S. For the case of a straight line log-log scale representation of the S-N curve, the relation

$$N(S) = \frac{K}{S^b} \tag{4.19}$$

can be used where K and b are material constants. Substituting (4.19) into (4.18), for the total damage expected from time t=0 to T, gives

$$E(D)_T = TK^{-1}\mu \int_0^\infty S^b P_{RR}(S)dS \tag{4.20}$$

The complete flow of operation from sensing to fatigue life monitoring for embedment into the *Narada* wireless sensor is shown in Figure 4-4 for the RFC and Dirlik methods.

4.4 Embedded Procedures

Time domain RFC requires continuous data acquisition and processing, and as such our sensing unit is required to complete the RFC procedure in a timely fashion so that there is no back up with simultaneous data collection. The embedded procedure operates in 128kB of external SRAM. External memory is divided into two 64kB halves denoted as low and high (Figure 4-5a). Data acquired is stored on the low side in three separate blocks with a capacity of nearly 20kB each. This allows for the acquisition and processing of data sets containing nearly 10,000 2-byte points. The three stage data acquisition guarantees the continuous acquisition of strain data in one block while fatigue life procedures (such as RFC and damage accumulation) are performed simultaneously on a previously attained set of strain data.

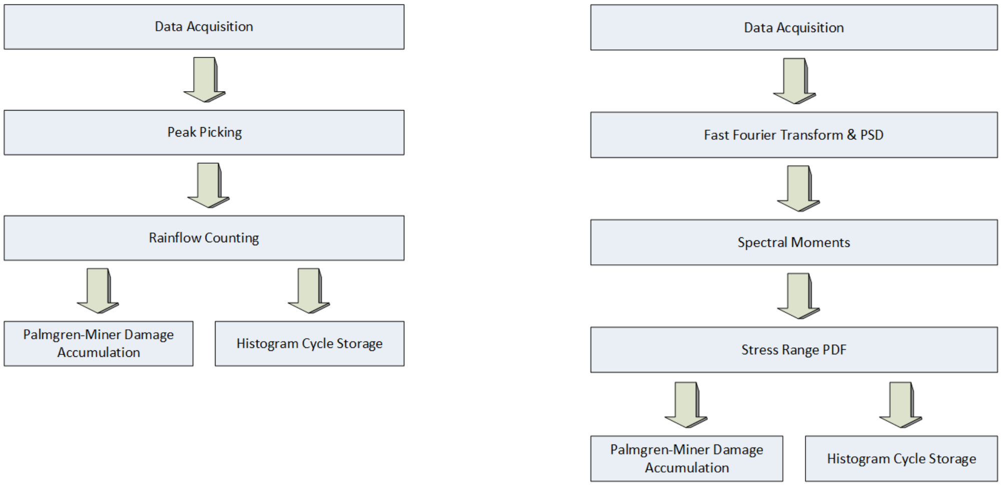

(a) (b)

Figure 4-4. Flow of operation for embedded fatigue analyses in the (a) time domain and (b) frequency domain

After a stack of memory is filled, a peak picking algorithm is performed on the set of strain data. A set of only peaks and valleys are stored in a specific location on the high side of the external SRAM. The extreme condition considered for sizing memory allocation occurs when all points acquired during sampling result in peaks or valleys of the strain response signal, requiring an equally sized 20kB memory allocation. The RFC procedure is carried out on the set of peaks and valleys and stored on the high side of the external SRAM. Extreme conditions here would see less than half the number of peak/valley points as the maximum number of cycles, requiring 10kB of memory allocation for strain amplitude and mean strain each. The remaining 20kB of external SRAM on the high side is used as a continuously updated histogram. In the case where the number of cycles is represented as a 2 byte integer, 10,000 unique strain amplitude-mean strain combinations are available. Any m-by-n product of amplitude bins, m, by mean bins, n, less than 10,000 are admissible. In this test, cycles are accumulated in a 2 byte memory slot, limiting the maximum number of cycles that can be accumulated for a specific strain amplitude and mean strain to 65,535 cycles. All processing procedures carried out on the high side of the external SRAM allow for continuous strain gage data acquisition on the low side by way of an interrupt on the analog-to-digital converter. The external SRAM layout from the RFC method is shown in Figure 4-5a.

The Dirlik procedure requires less of a scheme for memory use as it is not a continuous process. Data is collected periodically and stored in external SRAM, limited in size only by the memory requirements of the Fast Fourier Transform (FFT) which is to follow. For this study a 4096 point FFT, is performed on approximately 8.2 kB of data. The FFT algorithm produces a real and imaginary floating point (4-byte) component for each complex number, requiring approximately 33kB of SRAM for storage. The Dirlik procedure relies on spectral moments, so a one-sided power spectral density is stored in 16.5kB of SRAM. Most of the high side of the memory bank remains to store the results of the Dirlik procedure in the form of a stress range pdf. The pdf can be scaled for a histogram type of storage or directly applied to the Palmgren-Miner rule for damage accumulation. The histogram and/or damage result can be stored long-term on-board the *Narada*, providing another method for decentralized fatigue life monitoring having minimal transmission requirements. A memory map of the external SRAM for the embedded Dirlik procedure is shown in Figure 4-5b.

By decentralizing the fatigue life monitoring process, great savings in communication can be realized. Table 4-1 shows an analysis of communication requirements of a centralized RFC implementation and a decentralized computing implementation. The hypothetical example in Table 4-1 considers 10 minutes of continuous data acquisition at a sampling frequency of 50 Hz. The decentralized implementation sends one histogram at the end of the ten minutes resulting in a transmission reduction of approximately 67%. Fatigue life monitoring though, will require much longer periods of data acquisition and will further exploit the transmission reduction.

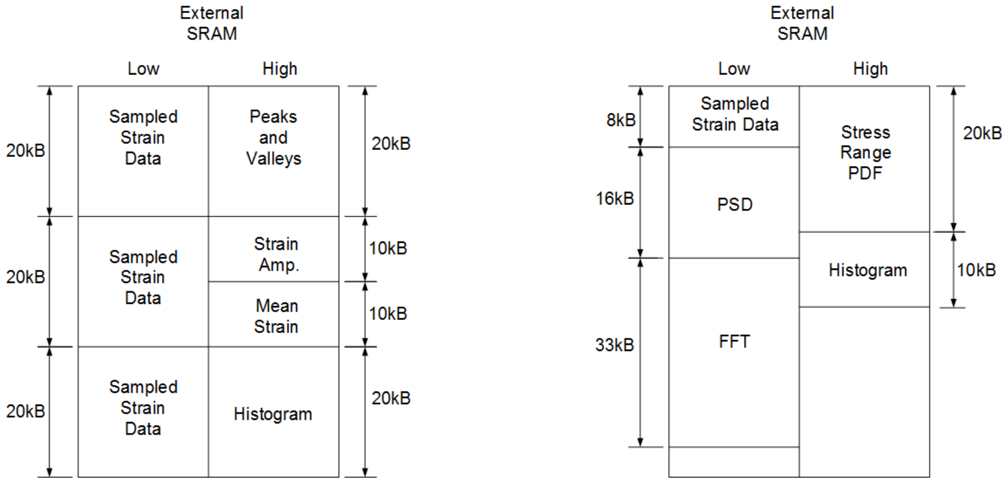

(a) (b)

Figure 4-5. Memory map of external SRAM for embedded (a) rainflow and (b) Dirlik procedures

Table 4-1. Analysis of communication requirements of centralized and proposed decentralized fatigue life monitoring methods

Methods	Transmission payload byte
Centralized *Rainflow counting performed on central server after all time history data is received*	$N_{data} * 2\ byte = 60\ kbyte$
Decentralized *Rainflow counting conducted on wireless sensing nodes with cycle histogram sent to server*	$Histo * 2\ byte = 20\ kbyte$
	Transmission reduction = ~ 67 %

Note: Time history data length, N_{data} = 30,000 points
Histogram size, $Histo$ = 10,000 bins

Figure 4-6 shows another hypothetical example of transmission payload over a 5 hour period for both the centralized implementation (where raw data is continuously streamed) and the decentralized implementation (where fatigue histograms are locally updated and occasionally transmitted). Raw strain gage data increases as a linear function of time for any given sampling frequency in the centralized implementation. The number of unique strain amplitude and mean strain cycles sent by the histogram in the decentralized implementation remain fixed, and thus increase by the same amount at each request. Histograms are sent once each hour. At the end of the 5 hour example, the decentralized computation produces 1700 less kB for transmission than the centralized implementation, resulting in a 94% transmission reduction. Further increase in time between histogram transmissions will result in even greater transmission savings. By receiving compact amounts of meaningful data transmitted upon request as opposed to receiving vast amounts of unprocessed data transmitted frequently, faster and more efficient analysis of the structural member under observation can be conducted.

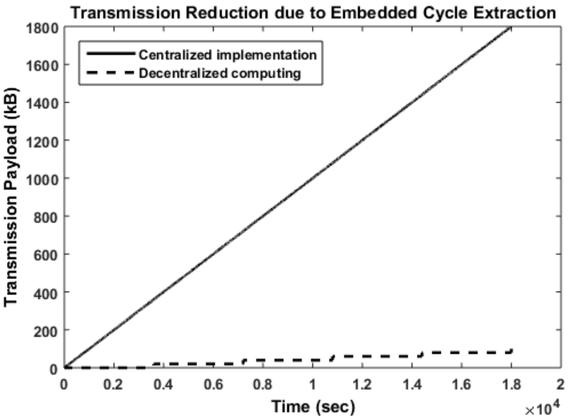

Figure 4-6. Transmission payload reduction due to embedded processing

4.5 Experimental Validation Testing

4.5.1 Small-scale Laboratory Coupon Testing

An aluminum coupon specimen was tested to validate the RFC implementation to the *Narada.* Specimen material 6061-T6 aluminum alloy is used; mechanical and physical properties can be found in Mil-HDBK-5H [174] and ASM Material Data Sheet [175]. The aluminum bar specimen being tested measured 17 in x 3 in x 1/8 in (43.2 cm x 7.6 cm x 0.3 cm). A 0.4 in (1 cm) Tokyo Sokki Kenkyujo Co., Ltd. TML PFL-10-11-1L 120Ω strain gage was used at the mid-section of the bar. Bonding areas were removed of grease and oils and lightly polished before adhering strain gages. Fatigue loading was done using an MTS Series 318 electrohydraulic closed loop load unit. Hydraulic grips hold the specimen in place during loading. Specimens are subject to variable amplitude uniaxial tensile cyclic loading. The loading pattern consists of 100 randomly generated peaks and valleys, shown in Figure 4-7a. Load sets are looped continuously during testing. In an effort to compare a wired rainflow analysis with the ‘one-pass’ rainflow analysis embedded in the *Narada* wireless sensing node, the specimen strain gage was split with its output interfaced to both the wired and wireless systems as shown in Figure 4-7b. Strain gage lead wires were attached to a quarter-bridge Wheatstone and op-amp circuit. The output signal was provided

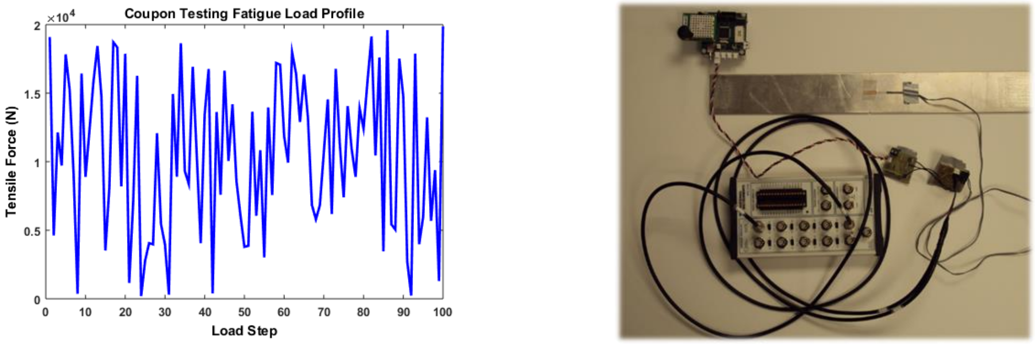

(a) (b)

Figure 4-7. Coupon specimen load profile and DAQ instrumentation

to the wired and wireless DAQ systems. In the case of the wired system, data collection is done using the National Instruments BNC-2110 DAQ at a sampling frequency of 100 Hz. In the case of the wireless system, the *Narada* wireless sensor uses a sampling frequency of 50 Hz. Data collected from the wired system is post-processed for cycle extraction after testing by RFC methods.

For the sake of comparison between the wired and wireless fatigue monitoring system, the wireless sensing system was set to transmit all cycles, giving strain amplitude and mean strain for each cycle at the end of each sampling block. Cumulative on-board histograms were also transmitted periodically during testing upon user request. Figure 4-8a compares wired and wireless rainflow cycle counting amplitudes, plotting all amplitudes calculated during RFC, reordered lowest to highest. It can be seen that the wired system produces more low amplitude cycles than the wireless system. Additionally, the wired DAQ system sampled twice as fast as the wireless system resulting in more peaks and valleys to consider during RFC. Figure 4-8b shows how the larger amplitudes compare by using a threshold strain amplitude for the wired system;

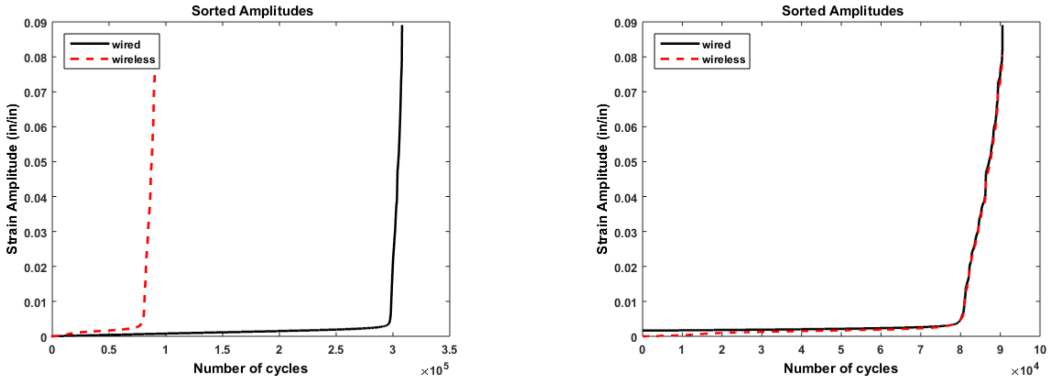

(a) (b)

Figure 4-8. Sorted cycle extraction for wired and wireless systems including (a) all cycles and (b) the wired system filtered by a threshold strain

similar amplitude outputs are extracted by both systems. Figure 4-9a focuses on the most relevant higher amplitudes to give a close-up comparison of the RFC result for the wired, wireless and embedded wireless procedures. The wired and wireless plots are calculated by post-processing on raw strain time-history data. The embedded wireless plots are made from the on-board histogram calculated by embedded RFC. The Palmgren-Miner rule is used to accumulate damage for the wired and wireless systems, as seen in Figure 4-9b. Damage accumulation for the three sets of results shows excellent agreement between the wired and wireless systems.

The laboratory coupon testing was performed to verify the performance of the *Narada* for strain gage sensing and embedded RFC procedure. Simultaneous strain sensing and on-board RFC were conducted at individual wireless sensors and compared with wired test results. It can be seen by Table 4-2 that the embedded wireless procedures reside within 5-6% difference (and is growing) in damage accumulation due to a slightly lower strain response than the wired system; the signal difference could be attributed to gain uncertainty in the signal conditioning circuitry.

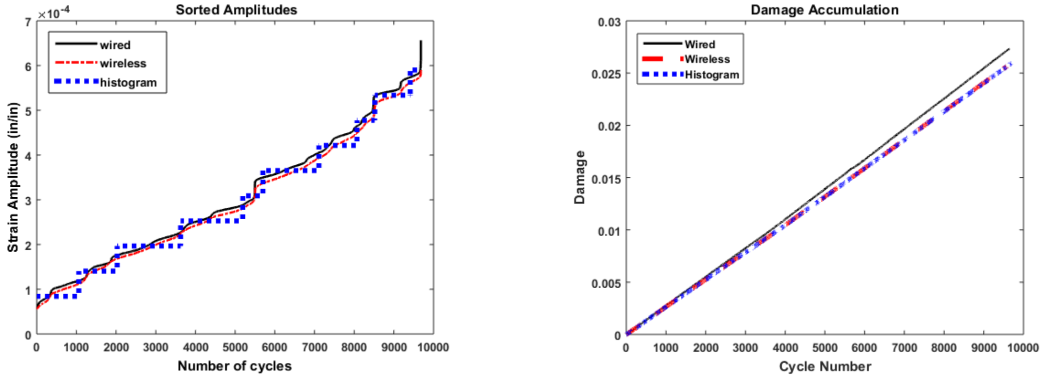

(a) (b)

Figure 4-9. Final comparison of the wired, wireless and embedded wireless systems by (a) relevant strain amplitudes and (b) damage accumulation

4.5.2 Monitored Aluminum Hull Integrity (MAHI) Task

The MAHI fatigue test program is focused on the design, fabrication and fatigue testing of aluminum hull stiffened-plate structural specimens. Fatigue testing was performed in the NSWCCD Fatigue Testing Laboratory in Carderock, MD. Among the main focuses of this testing program is for the demonstration and evaluation of structural health monitoring (SHM) technologies, such as the proposed embedded fatigue procedures.

The NSWCCD fatigue laboratory contains six uniaxial servo-hydraulically controlled load frames of varying capacity, all having full tension and compression cyclic loading capability. An Instron 220-kip machine was used in the experimental tests for this study. The Instron fatigue testing machine is computer-interfaced with analog controllers to allow for complex test loadings. Test machines are also equipped for data acquisition of up to 12 channels, including applied load, displacement, and strain gage response, capable of sampling rates up to 50 kHz.

Table 4-2. Fatigue Life Results

	Total Cycles	Cumulative Damage	% difference
Wired	9642	.00273	------
Wireless	9570	.00256	6.22
Binned Wireless	9684	.00259	5.13

The aluminum hull stiffened-plate structural fatigue test specimen shown in Figure 4-10 is used in this study. The specimen consists of a 5083-H116 aluminum plate, a tee stiffener machined from an A16061-T6 aluminum wide-flange beam extrusion, and a bulkhead detail made from A15083-H116 plate, as well as a vertical tee stiffener on the bulkhead machined from the above 6061-T6 stock extrusion. The specimens were fabricated according to generally accepted shipyard practice so as to respond with typical crack initiation behavior.

The stiffened plate specimen was subject to a zero mean random loading consisting of a computer-simulated sequence of 10,000 endpoints of Rayleigh distributed extrema generated using a first order auto-regressive technique [176]. Endpoints are connected by haversine curves

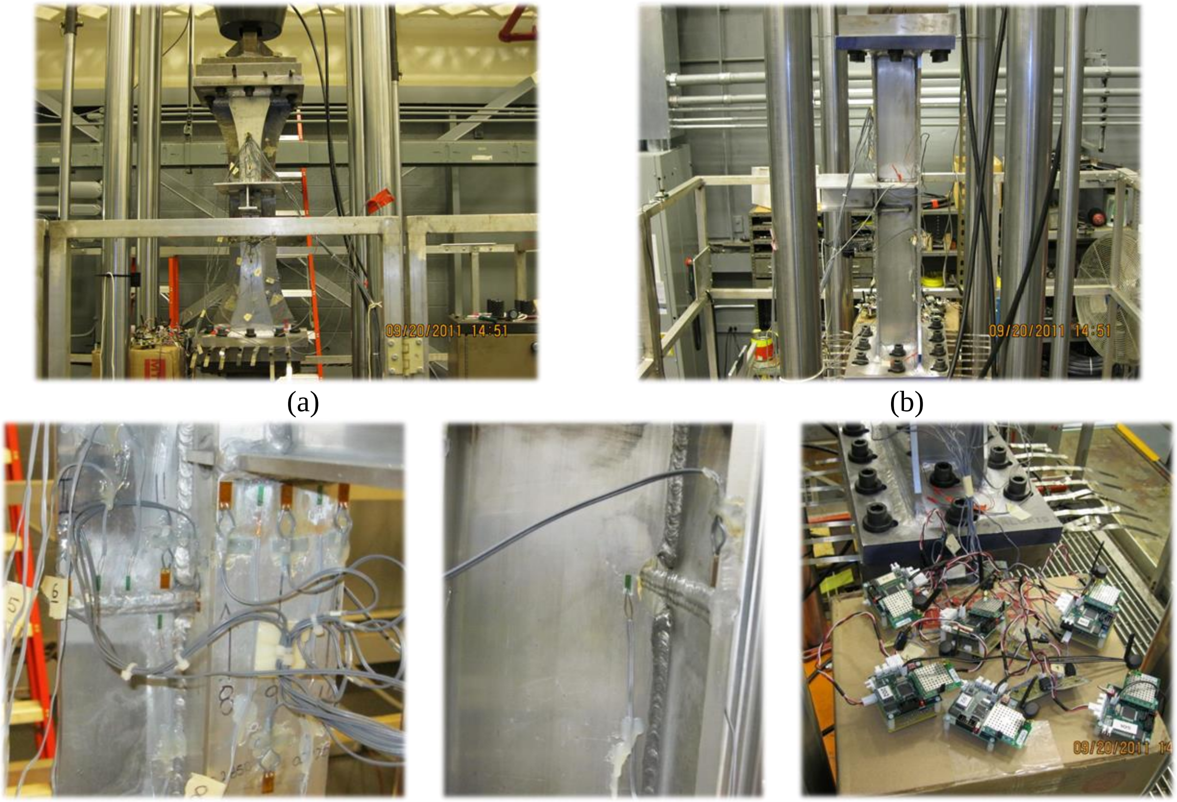

(a) (b)

(c) (d) (e)

Figure 4-10. Aluminum hull stiffened fatigue test specimen (a) front and (b) side view w/ strain gages installed for *Narada* wireless sensing units (green gage) & NSWCCD (yellow gage) near (c) weld joints and (d) plate notch (e) and with installed *Narada* WSN shown.

to produce a continuous waveform of unit root mean square (RMS) value. Loading is customized by multiplying each endpoint of the load sequence by the product of desired RMS stress and average cross sectional area of the specimen. Specifically, 3 ksi RMS loading was used in the tests reported in this study. All peaks are followed by an equal and opposite trough. All loading is performed under load control. The 10,000 point load sequence was continuously repeated 20 to 30 times during day time hours and rested at night. The stiffened plate specimen was axially loaded at a load rate of 400 to 500 kips per second.

A total of 12 *Narada* channels collected strain gage response at various locations on the aluminum hull specimen. Figure 4-11 provides a drawing of the test specimen with the installed strain gage sensor layout for both the *Narada* wireless system as well as the laboratory data acquisition. Several channels were dedicated to raw strain gage data acquisition as well as the embedded RFC and Dirlik fatigue life monitoring procedures described in this chapter. Strain gages were connected to one of two Wheatstone bridge configurations, differing only in amplification, shown configured with the *Narada* in Figure 4-10e near the test specimen. All *Narada* data acquisition was conducted at a sampling rate of 100 Hz. Raw strain data acquisition was performed continuously as well as the embedded RFC procedure (except when loading was suspended). Raw strain data was transmitted from the *Narada* to a receiver base station after 10,000 samples were collected (roughly every 100 seconds) and routed to a server (laptop) via USB for long-term storage. Processed RFC data was collected periodically for updates. Data for the embedded Dirlik procedure was collected for one minute duration every hour. Therefore, the resulting stress range pdf was applied to a one hour time period when calculating the accumulated damage given in (4.20). Processed data from the Dirlik procedure was also transmitted

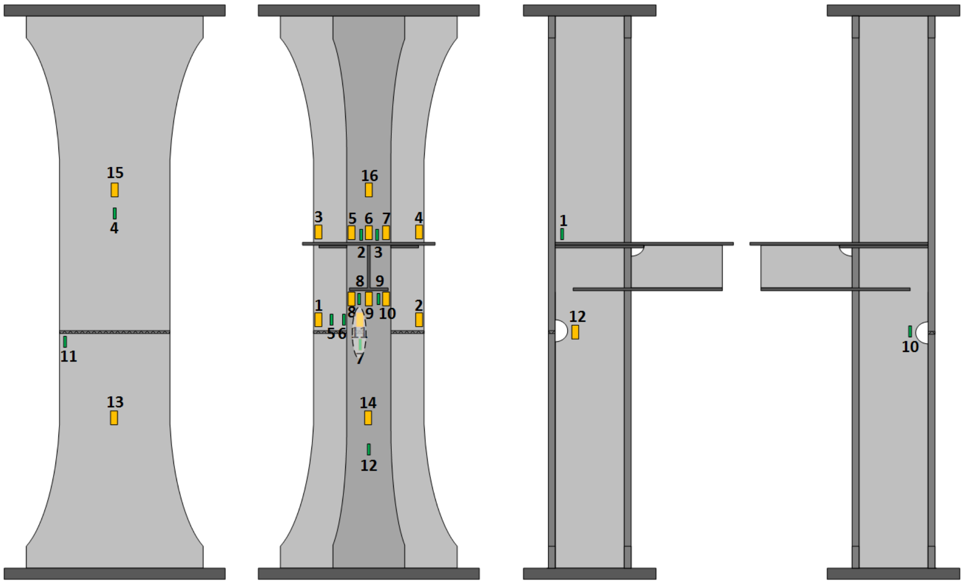

Figure 4-11. Aluminum hull stiffened fatigue test specimen diagram with *Narada* (green) & NSWCCD (yellow) strain gages labeled

periodically. Efforts were made to sample the complete range of the 10,000 point load cycle so as to acquire all aspects of the load signal.

Results from strain gages corresponding to *Narada* wireless sensing unit channels and NSWCCD laboratory data acquisition channels are compared for raw strain gage response, RFC histograms, and stress range pdf's. Effort was made to compare strain gages in areas assumed to experience similar stresses under uniaxial tension - compression. According to Figure 4-11, *Narada* gage # 8 and NSWCCD gage # 8 could be expected to have similar strain gage response. Figure 4-12 shows that the *Narada* wireless sensing unit first and foremost acquires accurate strain data necessary for reliable and accurate embedded fatigue life procedures. In Figure 4-13, histograms from RFC show the cycle extractions of *Narada* strain gage #6. For the purposes of comparison, this particular unit transmitted raw strain data as well as the embedded histogram

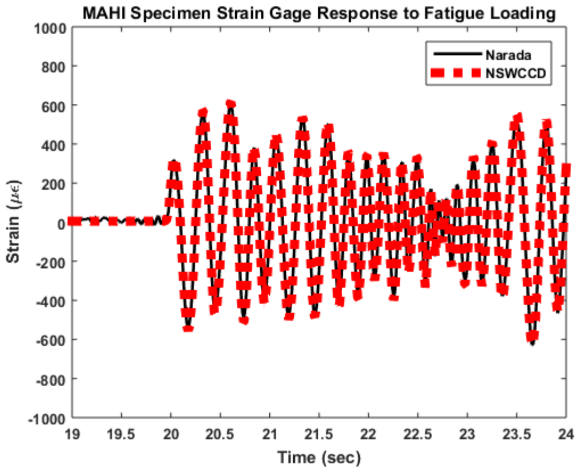

Figure 4-12. Comparison plot of raw strain time-history collected from the *Narada* wireless (solid) and NSWCCD wired (dashed) to demonstrate DAQ accuracy prior to embedded procedures

periodically. Figure 4-13a shows the histogram output from the embedded procedure after four days of continuous fatigue life processing while Figure 4-13b shows the output from RFC on the raw strain gage data in post-processing. As Figure 4-12 helps to validate the *Narada* DAQ against the NSWCCD DAQ, Figure 4-13 attempts to show the validity of the embedded RFC routine for the same strain gage response. Final damage estimates compare well but relatively (2.16% difference) poorly reflect absolute damage values required for crack initiation monitoring. This is due to the use of an arbitrary aluminum S-N curve; future NSWCCD laboratory research for this

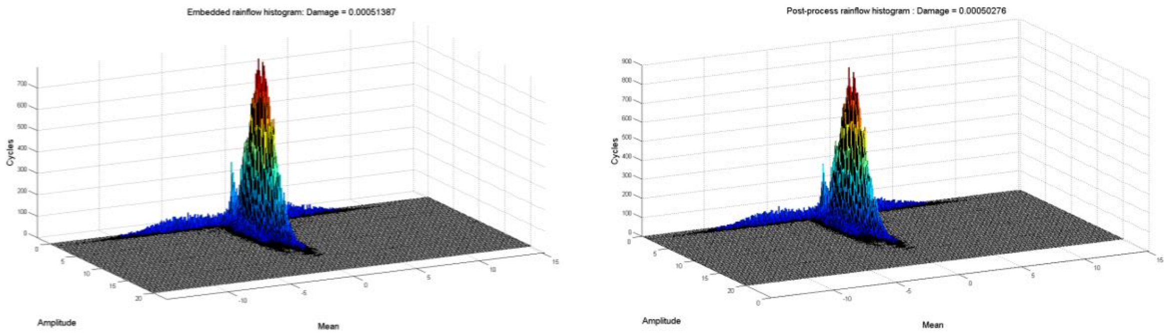

(a) (b)

Figure 4-13. Four-day rainflow counting histograms for (a) embedded *Narada* and (b) MATLAB post-processing of NSWCCD wired system

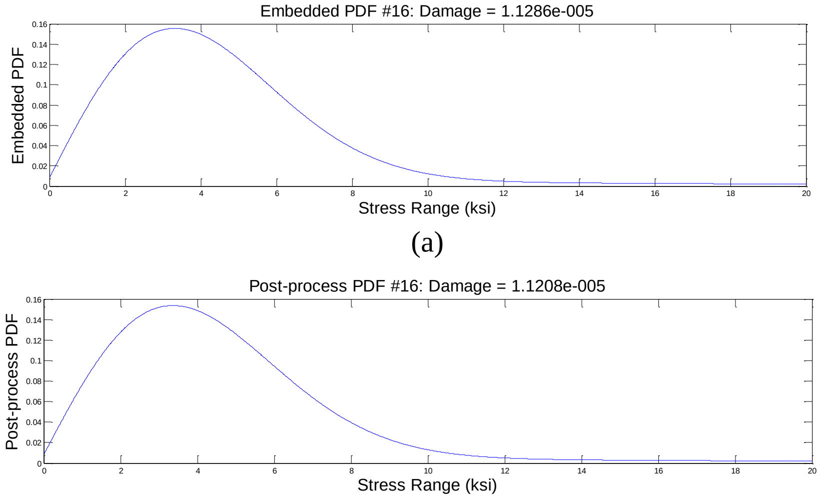

(a)

(b)

Figure 4-14. Stress range pdf obtained by Dirlik formula for (a) embedded procedure (b) raw data in post processing

project includes constructing system specific S-N curves so that final damage estimates would more accurately reflect crack initiation ($D = 1$).

To validate the embedded Dirlik procedure, the stress range pdf produced by *Narada* strain gage #7 is observed. The pdf was calculated and stored on-board, and compared with raw strain data post-processed for P_{RR}. Figure 4-14 shows stress range pdf's generated at strain gage #7 with the one hour damage accumulation from each pdf. The generated pdf's show very close agreement, resulting in a damage accumulation difference of 0.69%.

Damage accumulation comparisons between *Narada* and NSWCCD strain gages was difficult as all strain gage channels were placed at unique positions on the specimen and complex strain fields are expected due to the specimen geometry. However, damage accumulation for NSWCCD strain gage #9 and *Narada* strain gage #9 are shown due to their close proximity. The resulting transmission payload and damage accumulation are shown in Figure 4-15. Very similar damage accumulation can be seen in Figure 4-15a for the NSWCCD and *Narada* strain gages, measured on separate DAQ networks and processed by centralized and decentralized systems,

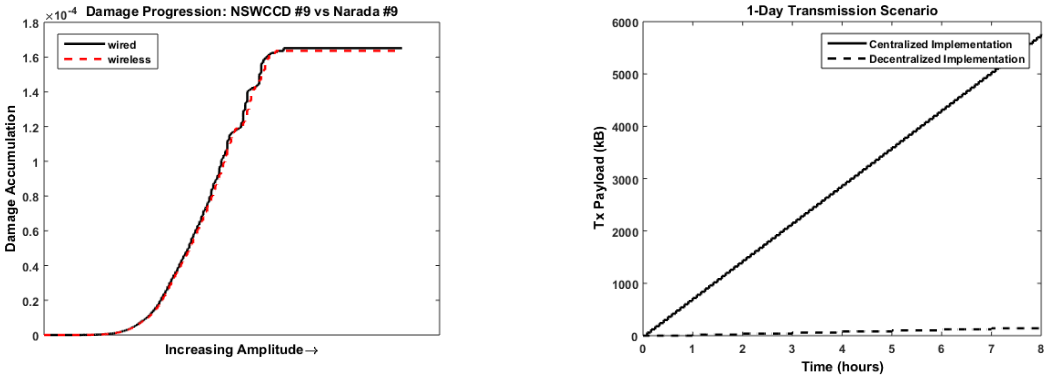

(a) (b)

Figure 4-15. (a) Damage accumulation for two closely situated strain gage sensors (NSWCCD #9 & *Narada* #9) (b) 1-day transmission requirements of typical acquisition system vs. proposed decentralized system

respectively. Results for transmission requirements for the RFC procedure for one day of testing, collecting rainflow histograms once per hour, can be seen in Figure 4-15b. The figure assumes 60 kB of data transmitted (max capacity in external SRAM) every five minutes (sampling frequency @ 100 Hz) for the centralized implementation and a 20 kB histogram every one hour for the decentralized implementation. The observed reduction in transmission requirements shows the potential of the decentralized embedded RFC procedure to greatly ease power and bandwidth constraints on the wireless network.

Observation of the two embedded procedures in Figure 4-13 and Figure 4-14, along with the accuracy of the *Narada* wireless system against the NSWCCD tethered system as shown in Figure 4-12 demonstrates the ability of proposed decentralized wireless system to perform reliable fatigue life monitoring leveraging the embedded computing power available on-board the *Narada* wireless sensor.

4.6 Summary and Conclusions

Proposed in this chapter are two decentralized fatigue life monitoring schemes for embedment and implementation in a wireless network. The *Narada* wireless sensing unit provided strain gage response consistent with wired NI-DAQ and NSWCCD-DAQ systems. On-board histograms, pdf's and damage accumulations were in very close agreement with post-processed data from wired and wireless systems. The ability of the *Narada* wireless system to accurately acquire and process data for fatigue evaluation presents an extremely valuable tool for structural asset managers requiring high sensor density without obtrusive installation and high costs. The decentralized procedure shows great reductions in transmission payload, directly related to power and bandwidth constraints thus making long-term wireless applications more sustainable.

CHAPTER 5.

LONG-TERM CONDITION MONITORING OF THE TELEGRAPH ROAD BRIDGE FOR PERFORMANCE-BASED MANAGEMENT

5.1 Introduction

Among the main goals of this thesis is to add to, and perhaps transition from, current state-of-practice long-term monitoring strategies, such as global vibration-based damage detection. To be more informative as a bridge management tool (rather than simply a damage detection tool), assessment of the performance of a bridge according to specific typical damage modalities should be made. In this chapter, a novel long-term wireless structural monitoring system for a very representative highway bridge class is demonstrated for statistical performance-based structural monitoring. Several data processing techniques for sensor data are shown for specific damage modalities common to steel multi-girder concrete deck composite sections with pin and hanger assemblies. These concerns have been voiced by MDOT [7] and drive the sensor layout and processing strategy. Further, the proposed processing algorithms are automated through the *SenStore* cyberinfrastructure framework by a variety of techniques machine learning and regression techniques. Long-term data is collected on specific damage modalities to model dependencies on environmental and operational conditions (EOCs) using Gaussian Process Regression (GPR) methods. The statistical behavior of each process is further characterized using a statistical process control (SPC) anomaly detection framework to monitor the consistency of an assumed healthy process and quickly identify process changes. Outlier detection methods (*e.g.*, SPC) previously used in bridge SHM typically evaluate single sensor time-history data directly (*e.g.,* acceleration) or features such as auto-regressive model residuals [35]. Here, targeted system behavior responses driven by owners needs such as neutral axis position, link plate bending and deck strain are evaluated. The goal of the top-down strategy is to position the WSN to make capacity measures often ignored or assumed. Specifically, sub-system capacity can be largely affected by boundary conditions (*e.g.*, pin and hanger rotation, steel-concrete interaction, free thermal expansion); as such these capacities are specifically monitored to set the stage for future data-driven reliability-based monitoring (included in Chapter 6). Analysis methods are designed for automated information extraction, utilizing support vector machine (SVM) classifiers trained on supervised field data to detect important bridge traffic events (*i.e.*, heavy truck crossings) without user intervention. Data-driven performance-based condition monitoring is demonstrated as a complement to current practice of VI and to promote SHM systems as a tool for performance-based management.

5.2 Decision Support Tools

Statistical process control (SPC) is the proposed decision support tool for this paper utilizing response statistics to ensure expected response mean and variation. Statistical process control is common in manufacturing quality control for example, where high volume production outputs failing to meet stringent specifications need to be identified and fixed immediately to ensure customer satisfaction as well as mitigate material, labor and overhead losses. Bridge owners can similarly benefit from a quality control framework where performance criteria are demanded. Deviation from normal process behavior can be an indication that further evaluation of the bridge may be required. The use of SPC has been demonstrated previously for vibration-based damage detection [35]. Here, targeted strain-based performance processes are cast into a SPC monitoring framework for automated real-time performance assessments. Automated SPC requires tools of its own to identify relevant loads (*e.g.*, truck loads) and account for signal dependencies (*e.g.*, temperature and load influence). In this study, two methods used to enable automated performance monitoring are support vector machines (SVM) for classification and Gaussian Process Regression (GPR) to model environmental and operational influences on target responses. Once the GPR model is built, it is used to predict target response given new EOCs. Difference measures (measured values – predicted values) are evaluated for SPC in this paper, with the hopes that the differences process being monitored is stable under changing EOCs for a normal process (in context here as normal bridge performance). A brief description of the tools utilized for decision support is made below. The evolution of the development and use of these tools for automated long-term SPC monitoring is shown by illustration in Figure 5-1.

5.2.1 Support Vector Machine

The majority of the data processing performed in this study stems from truck load events. Truck loads provide the largest sensor response and thus best signal-to-noise ratio, thereby reducing the uncertainty involved in downstream results. As such, a method is needed to distinguish truck response from small cars, free-vibrations, ambient response and signal faults. In this case, a two-class problem of isolating truck response signals from non-truck response signals requires attention {truck, no truck}. Support vector machines (SVM) [177] are a popular technique for this type of data classification. The goal of the SVM is to separate the two classes with an optimal seperating hyperplane rule based on training data that generalizes well for test data. A linear classifier has the form

$$f(x) = w^T x + b \tag{5.1}$$

where w is known as the weight vector normal to the line and b is the bias or offset. The classifier is a hyperplane of dimension $n-1$ for feature vectors of dimension n (*e.g.*, line in 2-D, plane in 3-D). Given training information on input vectors $x_i \in \mathbb{R}^n$ and corresponding class labels $y_i \in \{+1,-1\}$, for number of training sets $i = 1, \dots, l$, the goal is to determine which w and b result in the best decision hyperplane $(w^T x + b = 0)$. Several decision functions (hyperplanes) may separate the two classes but the hyperplane resulting in maximum margin is desired for SVMs [178]. An example is shown in Figure 5-2 for two-dimensional inputs where the seperating hyperplane $(f(x) = 0)$ is normalized for $f(x) = +1$ and $f(x) = -1$ for the points closest to the hyperplane from each class; these points are termed support vectors [178].

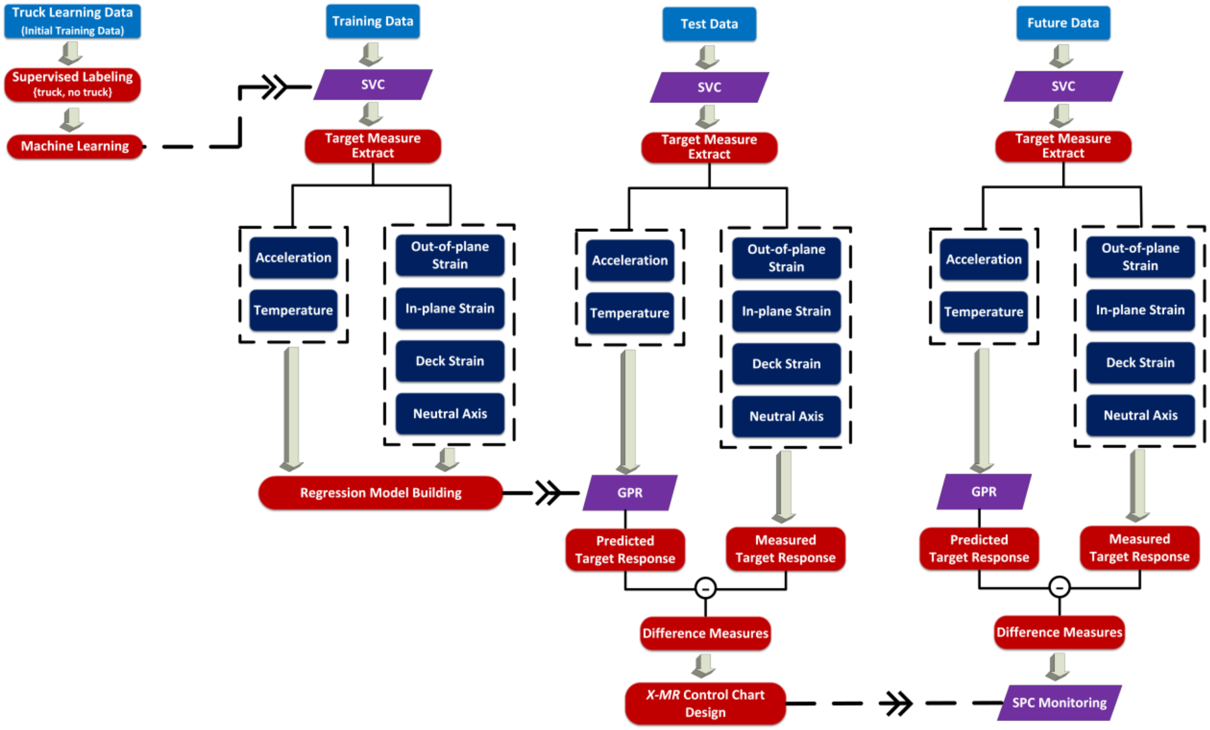

Figure 5-1. Decision support tool development over long-term data acquisition, beginning with SVC building for automated truck-load response detection, GPR modeling for response predictions under EOC influence, and ending with X-MR control chart building for SPC performance monitoring.

It is very possible that good classificiation in the input-space may require a more complex decision rule than a hyperplane (*i.e.*, non-linear classifier). One approach is to project data from the input-space into a higher dimension where linear classifiers are again good seperators. In this case, the classifier takes the form

$$f(x) = w^T \phi(x) + b \tag{5.2}$$

where $\phi(x)$ is a feature-space transformation mapping input vectors into a higher dimension. If the transformation is successful, a simple hyperplane in the feature-space will produce good seperation again. The use of kernel functions, which are low-dimensional but behave like inner products in higher dimensions, are advantagous here. Kernel functions given as

$$K\left(x_i, x_j\right) = \phi(x_i)^T \phi\left(x_j\right) \tag{5.3}$$

are used to solve the abovementioned problem in a dual form more conveniently (less computationally intensive). Many popular kernel functions are available; in this study, the radial basis function (RBF) is used, defined as

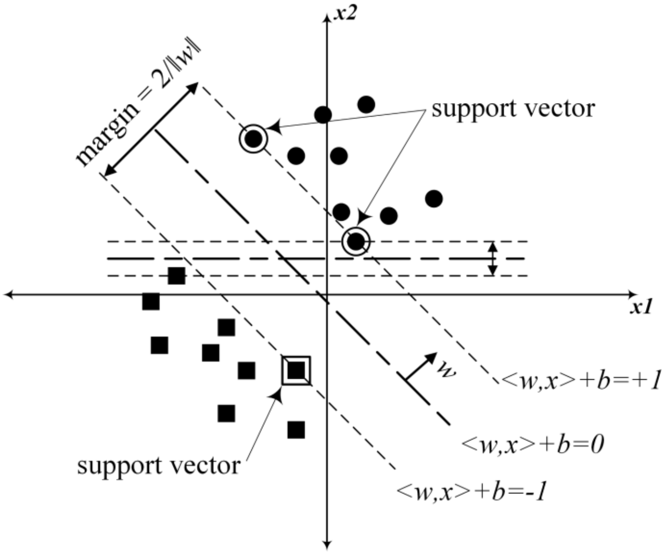

Figure 5-2. SVM classifier with optimal and sub-optimal separating hyperplanes shown; support vectors coincide with optimal (maximum-margin) hyperplane.

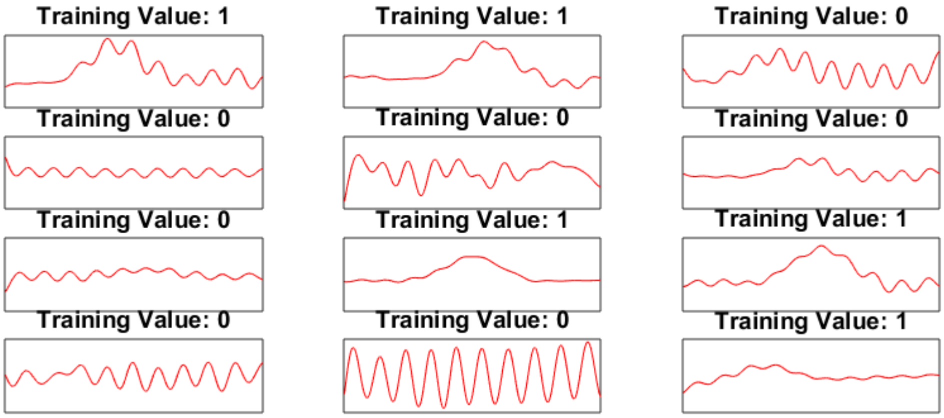

Figure 5-3. SVM training sets for truck load event detection.

$$K(x_i, x_j) = \exp\left(-\gamma \|x_i - x_j\|^2\right), \qquad \gamma > 0 \tag{5.4}$$

TRB training data examples chosen from finite time intervals on strain gage data include skewness, number of zero-crossings, range, spectral moments, and integration. These examples are meant to distinguish truck load response signals from small car, free-vibration, ambient and fault signals. Figure 5-3 shows twelve sample time-history signals from the TRB and their classification given during training. Signals are paired with class labels (the algorithm used here utilizes 1 and 0 as class labels) to distinguish truck load response from non-truck load response. Support vector classification (SVC) is performed using the LIBSVM software [179] through MATLAB. In particular, the SVM requires the solution to the following optimization problem [177]:

$$\begin{aligned} &\min_{w,b,\xi} \quad \frac{1}{2} w^T w + C \sum_{i=1}^{l} \xi_i \\ &\text{subject to} \quad y_i(w^T \phi(x_i) + b) \geq 1 - \xi_i, \\ &\qquad\qquad \xi_i \geq 0 \end{aligned} \tag{5.5}$$

where C is a relaxation (penalty) term to allow points inside the margin as well as misclassified points and ξ_i is a slack term representing the distance from an inside margin or misclassified point to its actual margin boundary (*e.g.*, $0 < \xi_i < 1$ in margin and $\xi_i \geq 1$ when misclassified). For more information on the SVC algorithm utilized for this paper, the interested reader should reference [179].

5.2.2 Gaussian Process Regression

In-situ data often requires normalization to account for environmental and operational influences on sensor signals. Here, Gaussian Process Regression (GPR) is used to model dependencies (*e.g.*, temperature, load magnitude) and "de-sensitize" data prior to evaluation for anomalous behavior. GPR is a non-parametric regression model built using data statistics [180]. GPR is capable of handling multi-dimensional inputs, accounting for noise effects, mapping non-linear feature vectors into linear data in higher dimensional spaces, and providing prediction of system outputs (*e.g.*, peak strain). In addition, GPR produces confidence ranges on its predictions which is very convenient when the prediction is used in a statistical analysis. GPR is briefly described in this paper; more comprehensive references are readily available [180-182]. The tools and algorithms used for GPR in this work are credited to Rasmussen and Nickisch [183].

Similar to most regression problems, the system is modeled as,

$$y = f(\boldsymbol{X}) + \varepsilon \tag{5.6}$$

where $\boldsymbol{X} \in R^{n \times d}$ is the input, *n* is the number of data sets, *d* is the dimension of different input features, $y \in R^n$ is the output and ε is process noise, which is modeled as Gaussian distribution with zero mean and a standard deviation of σ.

$$\varepsilon \sim \mathcal{N}(0, \sigma) \tag{5.7}$$

The distribution of the function f is a Gaussian process,

$$f \sim \mathcal{GP}(m, k) \tag{5.8}$$

where *m* is the function mean and *k* is the function covariance. Assuming the mean is zero for the given input *x*,

$$f \sim \mathcal{N}(0, K) \tag{5.9}$$

where *K* is the covariance function, then for $\boldsymbol{f} \coloneqq \{f(\mathrm{x}) \colon \mathrm{x} \in \boldsymbol{X}\}$, $\boldsymbol{f}^* \coloneqq \{f(\mathrm{x}) \colon \mathrm{x} \in \boldsymbol{X}^*\}$,

$$\begin{bmatrix} \boldsymbol{f} \\ \boldsymbol{f}^* \end{bmatrix} \Bigg| \boldsymbol{X}, \boldsymbol{X}^* \sim N\left(0, \begin{bmatrix} K(\boldsymbol{X}, \boldsymbol{X}) & K(\boldsymbol{X}, \boldsymbol{X}^*) \\ K(\boldsymbol{X}^*, \boldsymbol{X}) & K(\boldsymbol{X}^*, \boldsymbol{X}^*) \end{bmatrix}\right) \tag{5.10}$$

Therefore, when considering (5.6), the following is obtained:

$$\begin{bmatrix} y \\ y^* \end{bmatrix} \Bigg| \boldsymbol{X}, \boldsymbol{X}^* \sim N\left(0, \begin{bmatrix} K(\boldsymbol{X}, \boldsymbol{X}) + \sigma^2 I & K(\boldsymbol{X}, \boldsymbol{X}^*) \\ K(\boldsymbol{X}^*, \boldsymbol{X}) & K(\boldsymbol{X}^*, \boldsymbol{X}^*) + \sigma^2 I \end{bmatrix}\right) \tag{5.11}$$

After conditioning a joint Gaussian distribution of $\begin{bmatrix} y \\ y^* \end{bmatrix}$,

$$y^* \sim N(\mu^*, (\sigma^*)^2) \tag{5.12}$$

the mean and covariance are then defined as,

$$\mu^* = K(\boldsymbol{X}^*, \boldsymbol{X})(K(\boldsymbol{X}, \boldsymbol{X}) + \sigma^2 I)^{-\mathbf{1}} y \tag{5.13}$$

$$(\sigma^*)^2 = K(\boldsymbol{X}^*, \boldsymbol{X}^*) + \sigma^2 I - K(\boldsymbol{X}^*, \boldsymbol{X})(K(\boldsymbol{X}, \boldsymbol{X}) + \sigma^2 I)^{-1} K(\boldsymbol{X}, \boldsymbol{X}^*) \tag{5.14}$$

Covariance function *K* is defined using a kernel trick. There are many different kernels to use but this study will use the squared exponential (SE) kernel:

$$K(x, x') = \exp\left(-\frac{1}{2l^2} \left|\left|x - x'\right|\right|^2\right) \tag{5.15}$$

In this kernel, the hyperparameter *l* can be determined by optimizing the marginal likelihood function.

5.2.3 Statistical Process Control

Statistical process control (SPC) is the method used in this paper for comparing baseline statistical characteristics from targeted performance behaviors with future statistical characteristics. Assuming that normalized performance responses follow normal distribution behavior, statistical monitoring of the mean and variance can be used to indicate process change (possibly due to structural performance change). In particular, mean and moving range value control charts commonly referred to as $X - MR$ charts [184] are constructed from long-term TRB data and used as an automated statistics-based decision support tool. Charting sample averages (referred to as $\bar{X}$ charts) rather than individual values is preferred when a logical grouping of samples is present [185] as averages have less variance than single point collections and are more sensitivity to outlier detection in the monitoring procedure. Here , individual values are used as there is no logical grouping consideration for periodically collected bridge data. Moving range of two successive observations is often used as a measure of variability for individuals control charts [184]. Control charts on the individual observations and moving ranges are established by defining charting parameters of mean value, upper control limit (UCL) and lower control limit (LCL). For the individuals control chart, parameters are given as

$$\begin{aligned} UCL &= \bar{X} + 3\frac{\overline{MR}}{d_2} \\ LCL &= \bar{X} - 3\frac{\overline{MR}}{d_2} \end{aligned} \tag{5.16}$$

with the centerline at $\bar{X}$ being the mean of the individuals values and $\overline{MR}$ being the mean of the moving raing values. For moving range of size $n = 2$, $d_2 = 1.128$. For the moving range control chart, parameters are given as

$$\begin{aligned} UCL &= D_4 \cdot \overline{MR} \\ LCL &= D_3 \cdot \overline{MR} \end{aligned} \tag{5.17}$$

with centerline at $\overline{MR}$. Again, for moving range of size $n = 2$, $D_3 = 0$ and $D_4 = 3.267$ [184]. The data in the moving range control chart follows a skewed distribution and thus have non-

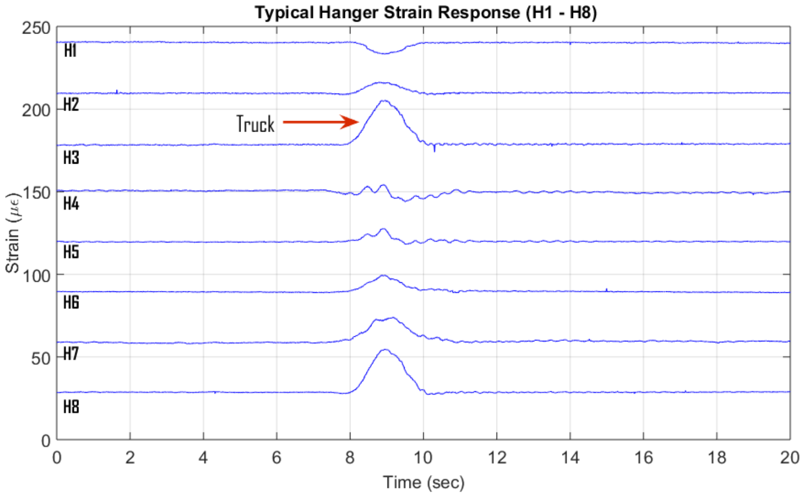

Figure 5-4. Link plate strain time-history at H1-H8 (rosette horizontal, rosette 45° rosette vertical, near-hole axial, out-of-plane north, in-plane east, out-of-plane south and in-plane west).

symmetric control limits. In-plane bending, out-of-plane bending, neutral axis position, and thermal strain difference measures (measured value – predicted value) are computed for mean and moving range values to develop $X - MR$ control charts proposed for automated long-term performance monitoring.

5.3 Results

5.3.1 Pin and Hanger Bending

Figure 5-4 shows typical hanger strain response for the eight strain gages detailed in Figure 2-6. Axially oriented gages (H3 – H8) all show a positive response to a predominantly axial load. The horizontal component of the rosette gage (H1) responds with negative strain due to Poisson effect. In-plane bending is calculated as $H6 - H8$, where the axial strain components and temperature effects negate and any weak axis bending effect is small as the strain gages are placed near the weak-axis neutral axis. It is easily noticeable in Figure 5-4 that H8 has a larger response than H6 which would calculate as a non-zero in-plane strain and indicate some degree of strong axis plate bending. Ideally, vertical acceleration in the center span would result in axial strain only

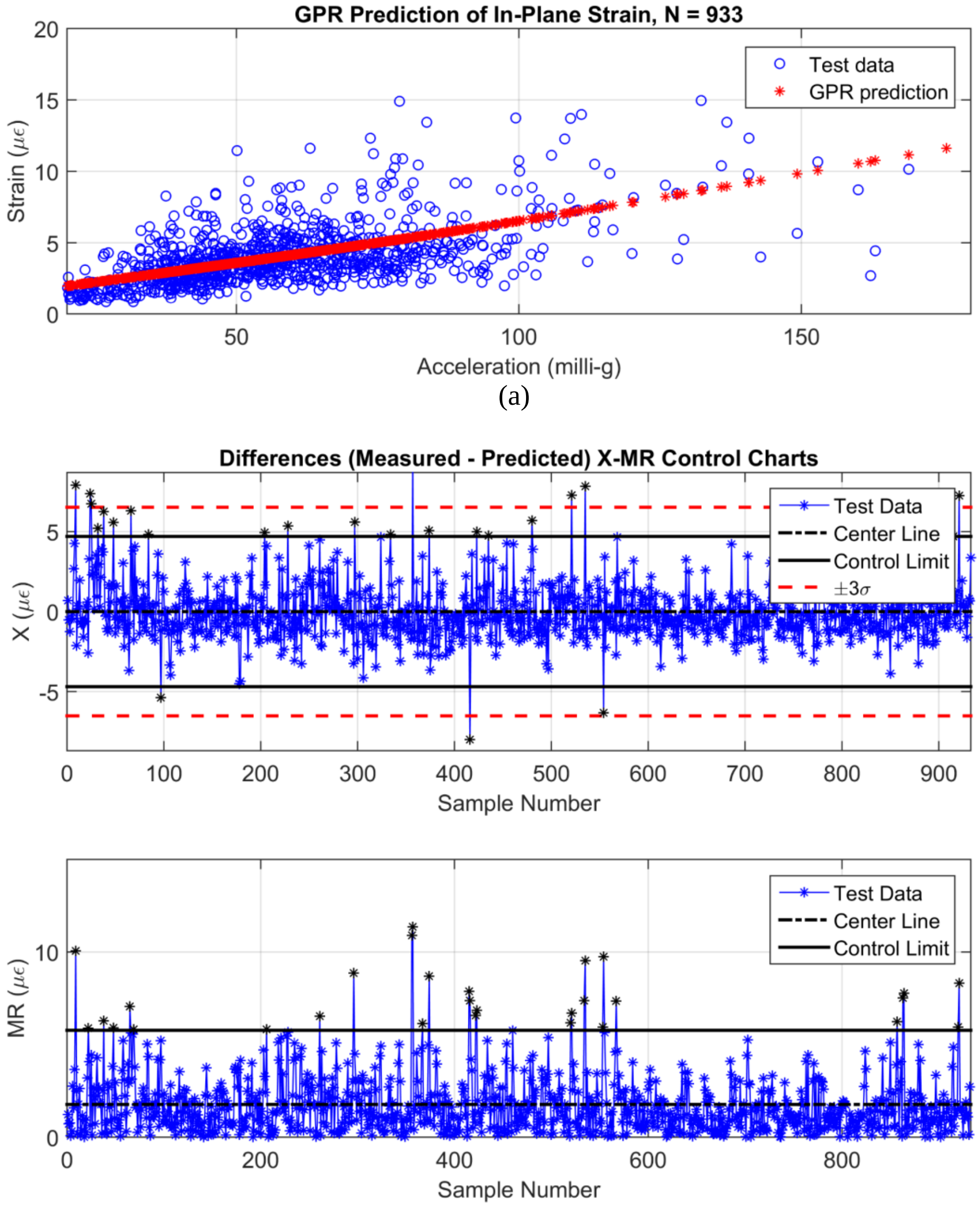

(a)

(b)

Figure 5-5. In-plane strain statistical modeling and evaluation by (a) GPR prediction of peak strain from peak accelerations and (b) X-MR control chart of peak in-plane difference measures (measured – GPR predicted).

in the link plates. Additional in-plane bending strains could indicate reduced rotational performance of the pin and hanger hinge mechanism. In the case of a frozen pin and hanger joint, in-plane strain magnitude in the hanger would be dependent on load magnitude. The dependence of in-plane strain on deck acceleration is modeled by GPR as shown in Figure 5-5a. A training set of peak in-plane strains with corresponding peak accelerations is used to develop the relationship model between in-plane bending and deck acceleration (proxy for load magnitude). Test data for in-plane peak strains from truck load events, as shown by blue circle markers in Figure 5-5a, are displayed versus the corresponding deck acceleration measured at each peak sample time. GPR predictions of in-plane strain for test data using acceleration data as input are shown by red star markers in Figure 5-5a. The GPR predictions resemble the main trend in measured test data well over the acceleration range and more clearly highlight the positive correlation of acceleration and in-plane strain. This type of correlation should be expected for partially frozen pin and hanger mechanisms, giving an indication of an in-plane bending stress state in the hangers during truck loading. Difference measures between the measured in-plane strains and the predicted in-plane strains are shown in the $X - MR$ control charts in Figure 5-5b. The difference measures (X) are zero-centered and rid of temperature dependence. Difference measures are plotted in chronological order. As can be seen by the X chart, LCL and UCL performance thresholds generated by X fit the majority of the test data. Standard limits as defined previously in (5.16) and (5.17) are given as solid lines near $\pm 5\mu\varepsilon$. Additionally, $\pm 3\sigma$ limits as defined by a normal distribution fit on the X data set are shown by dashed lines near $\pm 6\mu\varepsilon$, indicating 99.7% coverage. A different choice of control limits can significantly affect the decision support being given, especially when some outliers are expected for blindly automated data that may at times be misinterpreted, misclassified or even faulty. Several difference measures seen in Figure 5-5b suffer from this exact problem and can be seen as outliers to one or both potential control limits (UCL, LCL, ±3σ). The ability of the measurement system to provide consistent results should be an important consideration when making decision rules. The main goal of the X chart here is to indicate a slow changing mean value signifying progressive locking in the hanger plates due to corrosion buildup. The complementary MR chart shows the moving range from the X chart for consecutive points, serving primarily as a measure of process variation. Again, the majority of the moving range values lie within the control limits with the exception of few examples where extreme loads, faulty signals, misclassification or misinterpretation of automated data is the most likely culprit.

Out-of-plane (weak axis) motions are observed similarly to in-plane motions. Out-of-plane bending strain is calculated as $H5 - H7$, where axial strain, temperature effects and in-plane bending all negate. The TRB has a tendency to sway outward under vehicle loading, due in large part to its skew geometry. Larger loads often result in larger out-of-plane deformation. Figure 5-6a shows out-of-plane strain versus sway acceleration; again here, a weak but positive correlation exists. Out-of-plane bending was truncated at 20 με due to heavy grouping of low amplitude strains at low level accelerations. Strong oscillatory behavior can often be seen in out-of-plane measures due to low stiffness in the weak-axis, even for smaller vehicle crossings. Since automated classification occurs in the strain domain, high amplitude free vibrations can be misclassified as truck load events and associated with lower accelerations. The observed truncated relationship between acceleration and strain is expected (Figure 5-6a) as sway displacements must cause an out-of-plane bending in the hanger proportional to the vertical load being applied. Even though it is not unexpected, it is important to accurately characterize this behavior as a baseline measure to compare to potentially changed boundary conditions in the future from corrosion build-up. A $X - MR$ control plot (Figure 5-6b) is constructed by the same procedure as the in-plane strain procedure mentioned previously. Again several outliers can be seen in both charts but the majority of the process data lies within the control limits and appears to be random. Again, $\pm 3\sigma$ would be a more relaxed performance threshold, shown by dashed lines in the $X - MR$ control

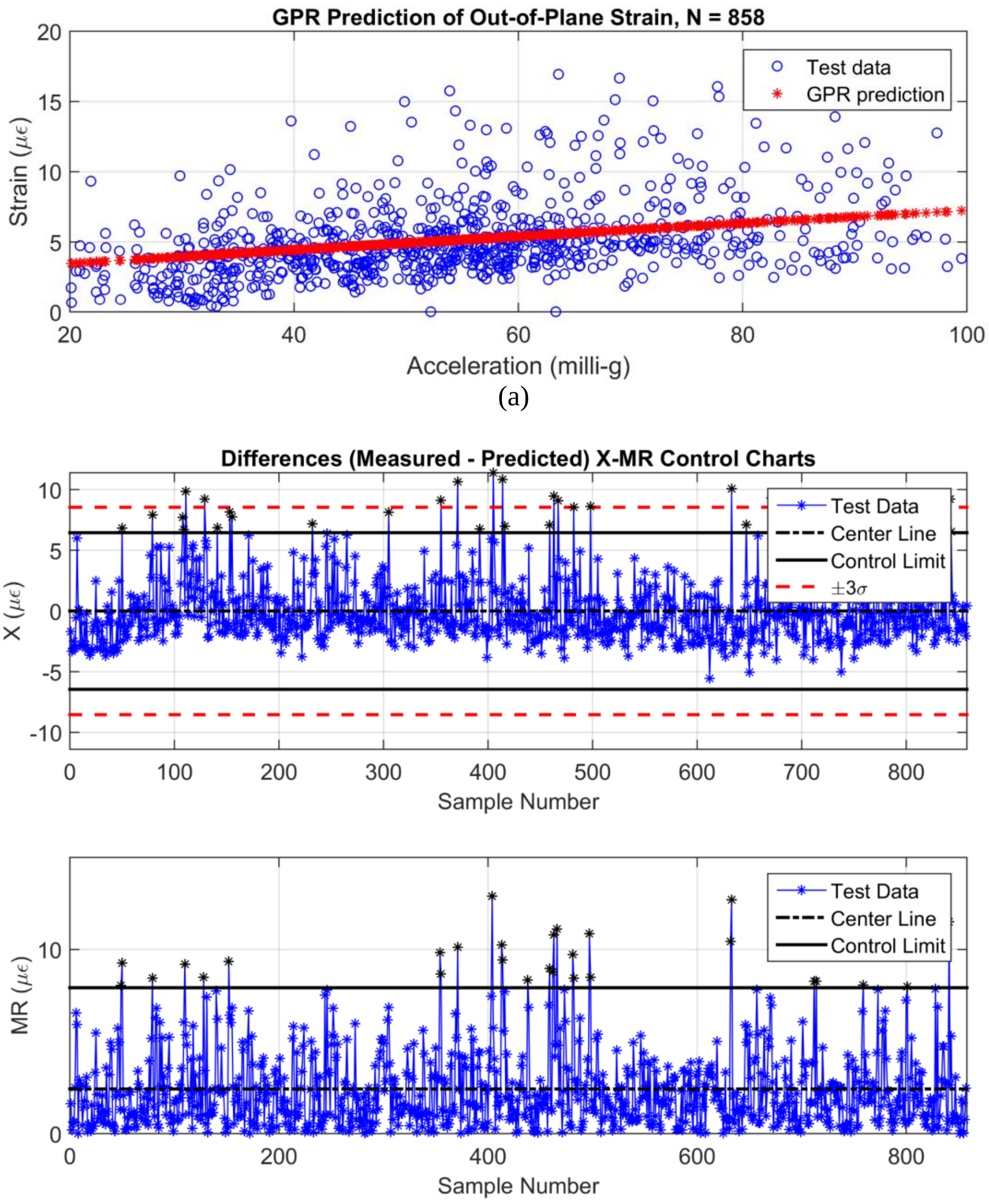

(a)

(b)

Figure 5-6. Out-of-plane strain statistical modeling and evaluation by (a) GPR prediction of peak strain from peak accelerations and (b) X-MR control chart of peak out-of-plane difference measures (measured – GPR predicted).

charts in Figure 5-6b, to account for outlier data as well as misclassified and faulty data. Long-term monitoring of the mean trend for out-of-plane bending can assist bridge managers to answer questions regarding the state of stress being introduced as well as the level of corrosion buildup in the hanger-pin interface region.

5.3.2 Fatigue

Fatigue life monitoring of link plate elements is a high priority for fracture critical bridge components. The first step in fatigue life analysis is to extract cycle information from time-history data. Here, strain gage measurements are processed for strain cycle information using time domain rainflow counting procedures [161]. Rainflow counting procedures are embedded on the *Narada* for an added benefit of data reduction and energy savings in the wireless network. Strain cycle histograms accumulated and stored on the *Narada* are used to evaluate remaining fatigue life according to AASHTO guidelines [186]. As all fabricated steels have some amount of flaws, fatigue failure is usually the result of slow crack growth from an existing discontinuity. As such, AASHTO takes a fracture mechanics based approach to the remaining fatigue life calculation [187]. The AASHTO requirement for fatigue life is modeled by theoretical fracture mechanics and supported by testing data. Specifically, detail categories were experimentally developed to characterize crack growth for typical structural geometries and configurations (*e.g.,* tension element with hole, end-welded cover-plated beam, etc.) by modeling the Paris equation

$$\frac{da}{dN} = A\Delta K^{m} \tag{5.18}$$

using regression analysis on test data. These constants are reliable for similar materials, loading and environments and are presented in AASHTO for various detail categories [187]. The design life is based on the number of stress cycles expected over 75 years. Estimated remaining life can be the sole piece of information transmitted to decision makers upon request, virtually eliminating the wireless payload associated with these sensors [188]. Figure 5-7a and Figure 5-7b show strain cycle histograms from the TRB for strain gages #4 and #3 (see Figure 2-6), axial strains recorded near the net-section at the pin hole and at the gross section at mid-plate, respectively. Stronger oscillatory response near the pin hole strain gage than at the mid-plate rosette, as shown by the higher cycle counts in Figure 5-7a, is typically observed in time-history data, as previously mentioned with the out-of-plane bending results. Again, the inference here is that the plate regularly experiences out-of-plane bending associated with traffic load events, which contributes largely to the near-hole response but very little to the mid-plate gage. The mid-plate gage sits near the inflection point for out-of-plane bending while the near-hole gage sits near the maximum moment location. The measured data also showed that the near-hole strain gage did not lie close enough to the pin hole to experience significant stress concentration. The cross-sectional area ratio of the pin-hole net-section as compared to the mid-plate gross section is approximately two which also factors into the larger responses seen at the near-hole gage.

In the AASHTO Guide Specifications for Fatigue Evaluation of Existing Steel Bridges [186] framework, fatigue evaluation begins with an effective stress calculation, S_r , calculated from the stress cycle histogram as

$$S_r = \left(\sum_{i=1}^{n} f_i \, S_{ri}^3 \right)^{1/3} \tag{5.19}$$

where

f_i = fraction of stress ranges within an interval

S_{ri} = midwidth of the interval

n = number of histogram bins

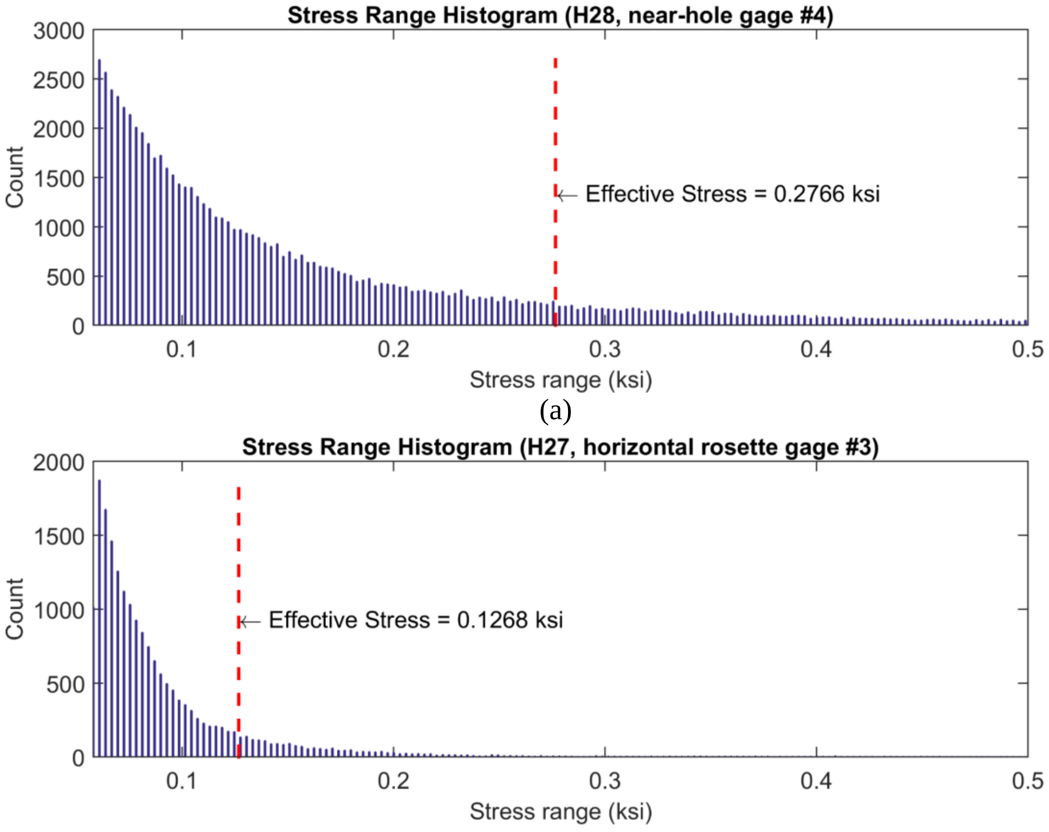

(a)

(b)

Figure 5-7. Stress cycle histograms via Rainflow counting procedure for (a) the axially oriented H28 near-hole gage (labeled #4 in Figure 2-6) and (b) the transversely oriented H27 mid-plate rosette gage (labeled #3 in Figure 2-6).

The effective stress is first used to evaluate if fatigue is a concern to be monitored at all by evaluating if the inequality

$$R_s S_r < S_{FL} \tag{5.20}$$

is true or false, where

R_s = reliability factor associated with calculation of stress range

S_{FL} = limiting stress range

If $R_s S_r > S_{FL}$, then fatigue effects can be ignored, or no crack growth can be assumed. Otherwise, further evaluation is required. To calculate remaining fatigue life for an estimated lifetime average daily truck volume, the following equation is used

$$Y_f = \frac{fK \times 10^6}{T_a C (R_s S_r)^3} - a \qquad (5.21)$$

Where

Y_f = remaining fatigue life in years

K = detail constant

T_a = estimated lifetime average daily truck volume in the outer lane

C = stress cycles per truck passage

S_r = stress range in ksi

R_s = reliability factor

a = present age of bridge in years

f = 1.0 for safe life calculation, 2.0 for mean life

The limiting stress range, S_{FL}, is given as 1.6 ksi (approximately 35% of the 4.5 ksi constant amplitude fatigue limit (CAFL)) for detail category E corresponding to link plates as specified in AASHTO Bridge Specifications. Figure 5-7 indicates effective stresses of approximately 0.27 ksi and 0.13 ksi for the near-hole and mid-section gages, respectively, on girder lines G2 and G6, well below the prescribed threshold of 1.6 ksi. The conclusion for these histograms is that fatigue is not a concern in these link plates, resulting in infinite fatigue life for link plate elements under normal traffic conditions. It is noted, however, that link plates on G3, G4 and G5 may experience strains larger than G2 and G6 due to load distribution. In the future, additional instrumentation may be placed on the these link plates or strain observations from G2 and G6 may be projected to other locations through FE modeling to make the most conservative remaining fatigue life calculation.

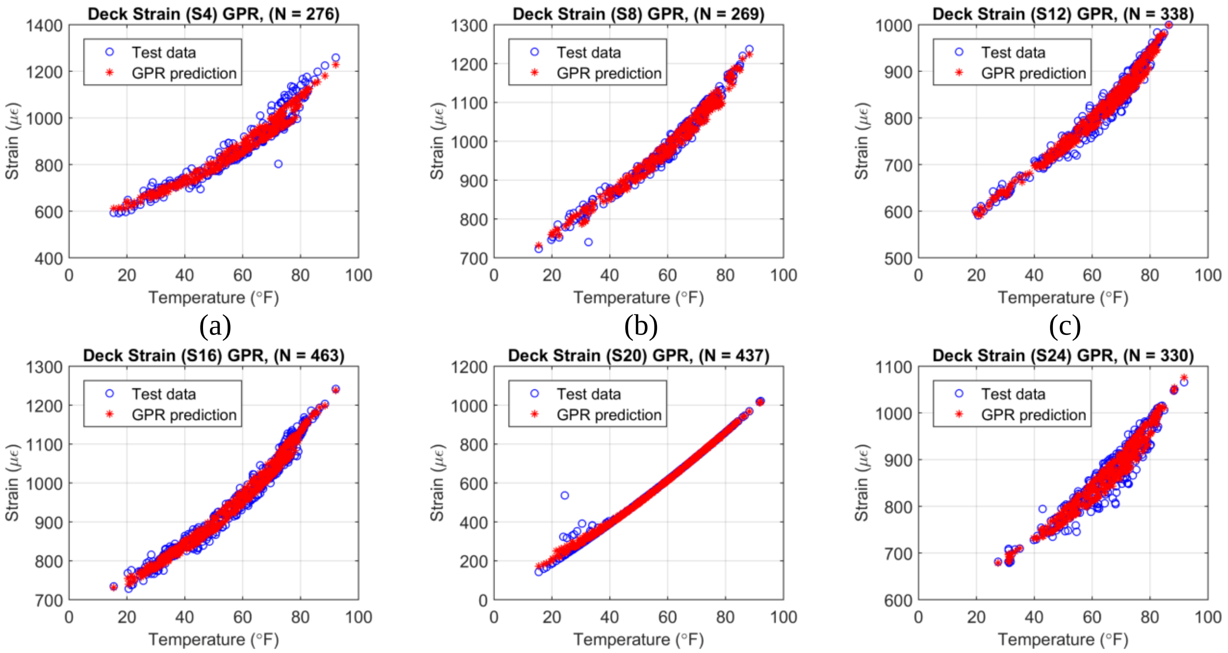

(a) (b) (c)

(d) (e) (f)

Figure 5-8. Deck strain averages (circle marker) versus temperature with GPR prediction (star marker) for (a) S4 (b) S8 (c) S12 (d) S16 (e) S20 (f) S24.

5.3.3 Beam End Contact

It is expected that the deck will thermally expand and contract with temperature increase and decrease, respectively. Figure 5-8 shows strong deck strain sensitivity to temperature as well as deck strain predictions via GPR modeling. Figure 5-8e shows the deck strain results for the S20 sensor, which has been a faulty sensor for the majority of the sensing program; it is included here for completeness. Good characterization of thermal influence is necessary for SPC monitoring. An interesting observation in thermal expansion was made when observing the data plotted one point at a time in chronological order. Daily fluctuations in deck strain did not increase and decrease along the same line, but rather around the line, exhibiting a hysteresis like behavior. Whether this is a physical function, a sensor function or an electronic function is an interesting question, but for the study here it is only important that this behavior be captured for better accuracy in the predicted values and thus better removal of temperature influence on static deck

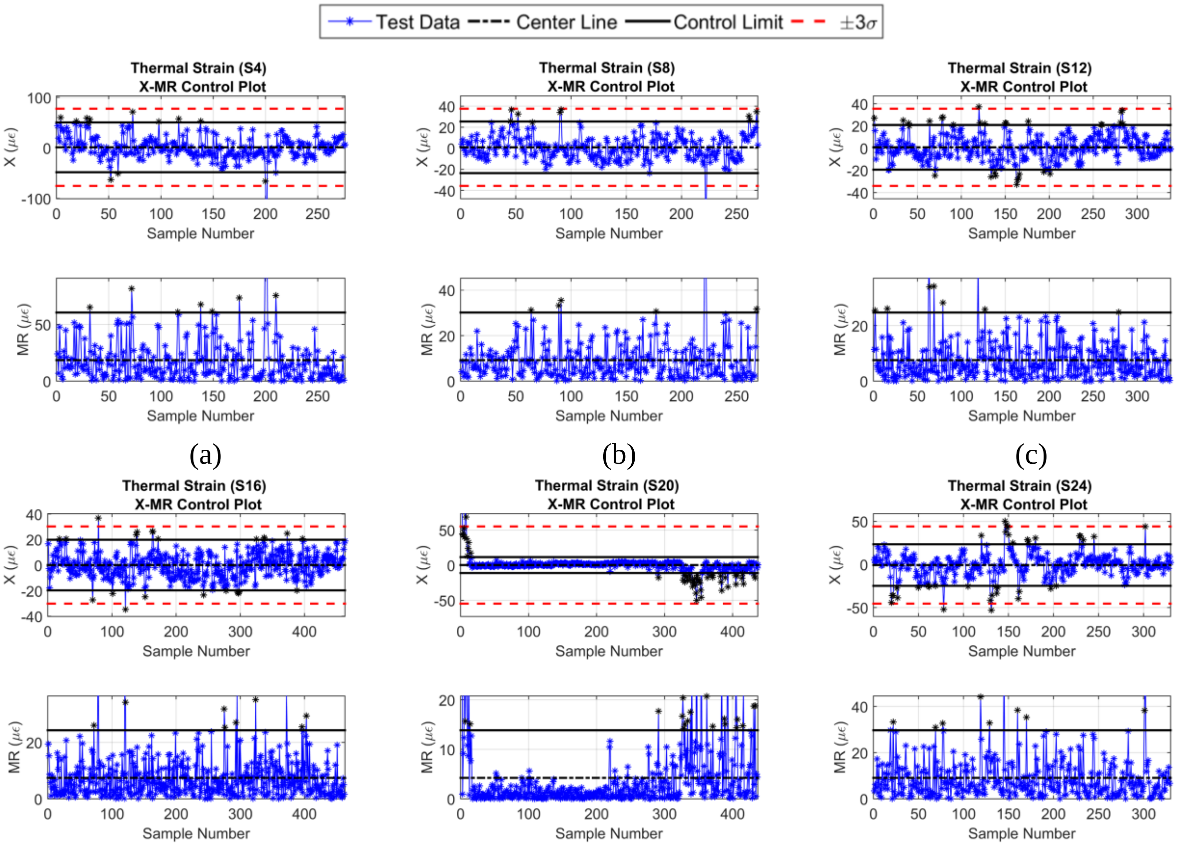

(a) (b) (c)

(d) (e) (f)

Figure 5-9. *X-MR* control charts of deck strain difference measures (measured – GPR predicted) for (a) S4 (b) S8 (c) S12 (d) S16 (e) S20 (f) S24.

strain. As such, time of day (hour) inputs were included with temperatures for each deck strain in the training data. Introduction of this second input improved deck strain predictions, removing an autocorrelation behavior previously present in the single input (temperature) case (undesirable for SPC). Previously shown GPR predictions for bending strain resulted in smooth line estimations due to a single input variable (acceleration). Here, the effect of the second input is evident as scattered predictions are produced. Figure 5-9 shows the difference $X - MR$ control plots for all six deck strain locations (S4, S8, S12, S16, S20, S24), with control limits. To save room in the plots here, a generic legend is provided at the top of Figure 5-9 which applies to all subplots (MR charts do not use the $\pm 3\sigma$ limits). Less outlier behavior is observed for these control plots than for the bending strain plots. Several explanations are possible: 1) two input features observed to

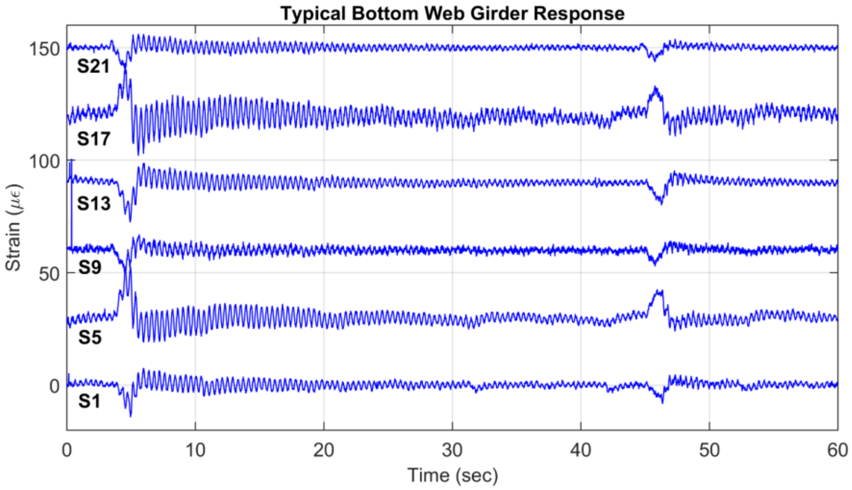

Figure 5-10. Girder strain time-history for bottom strain gage (3" above bottom flange) at all six center and end span measurement locations, highlighting positive bending response at center span (S5, S17) and negative bending response at end span (S1, S9, S13, S21) locations.

describe the strain behavior well are used; 2) static measures don't have the same variability and potential for extreme measures as live-load measures; 3) no classification takes place (*i.e.*, no potential for misclassification exists); 4) deck strain measures are mean values from time-history data, resulting in lower variability. Some outliers do exist in the $X - MR$ charts but again most of the data lies within the control limits. The targeted degradation is beam-end contact which would result in a strong mean shift. A strong mean shift or trend would be very effectively observed by the X control charts even in the presence of occasional outliers. Primarily linear response behavior in strain versus temperature for the complete temperature envelope at each of the monitored locations is a strong indication that the main span is free to expand year-round and that beam-end contact is not currently a concern.

5.3.4 Composite Action Assesment

Figure 5-10 shows one-minute strain gage response at strain gages positioned 3 in. (7.62 cm) from bottom flange for each of the six composite action sections evaluated (as seen in Figure 2-5). Positive bending is seen at the center span sections (S5 and S17) while negative bending is

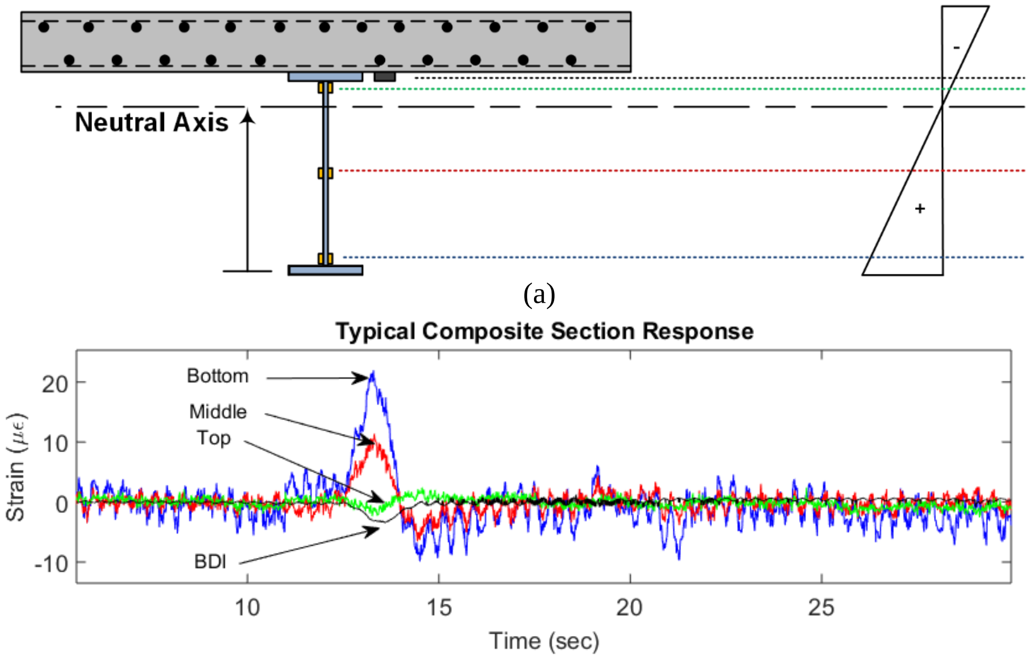

(a)

(b)

Figure 5-11. Composite action assessment: (a) illustration of instrumentation goal to construct live load strain profiles from longitudinal oriented strain transducers and (b) typical strain response for truck-load crossing showing expected relative magnitude and direction for composite action.

seen at the four end span sections directly over the pier caps. These time-history responses display expected responses in direction, magnitude and time. Three additional strain transducers (mid-web, top-web, bottom-concrete) at each section are used to evaluate composite action (see Figure 2-7). Figure 5-11a shows an illustration of the instrumentation goal for estimating neutral axis position using the four strain transducers at the section. Each sensor helps to build a live load strain profile where the neutral axis can be estimated as the zero-crossing location. TRB response data for the sensor configuration is shown in Figure 5-11b for a sample time-history of strain gage data acquired at the S17- S20 composite section location. As expected, response magnitude grows with distance from the expected neutral axis and responses are opposite in direction on either side of the neutral axis.

For neutral axis estimation, large load events are targeted as they have best signal-to-noise ratio in the time history, keeping variability in the neutral axis estimation low. Machine learning

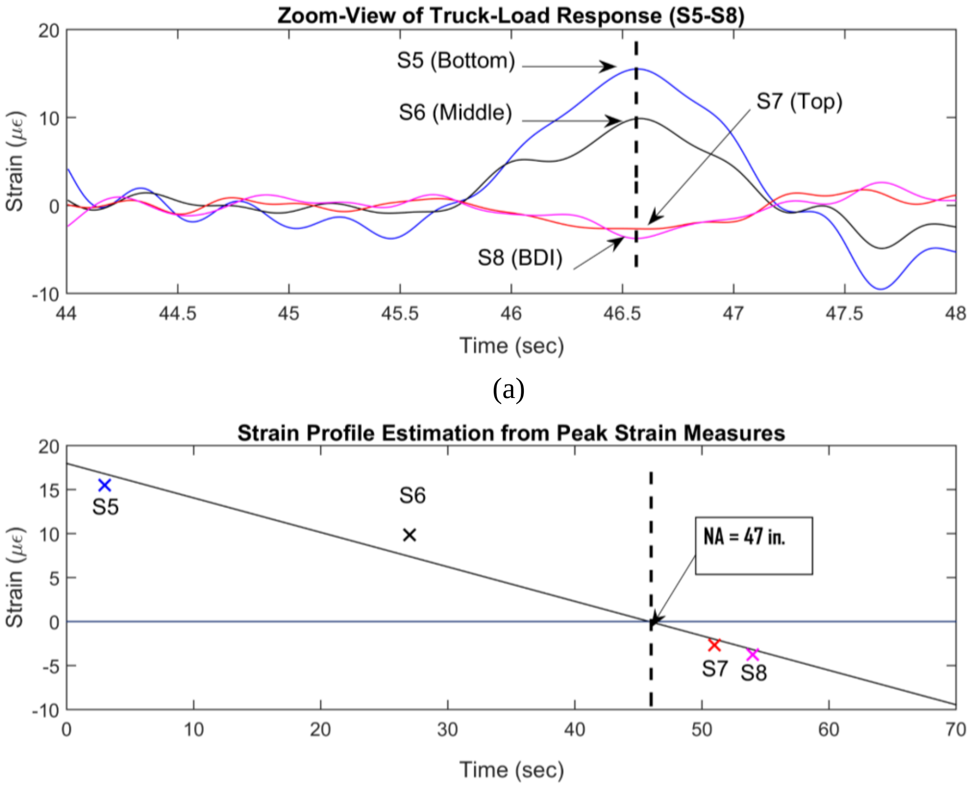

(a)

(b)

Figure 5-12. Neutral axis estimation: (a) zoom-view of strain response at deck section during truck crossing with localization of peak response (dashed line) and (b) corresponding strain profile estimation using linear fit on peak strain measures (BDI gage is not included in fit).

SVC is used to automate truck load event identification. Once the load events are found, the time of peak strain in the bottom gage is identified. Strain gage response for each of the four sensors (*e.g.*, S1 - S4) at the section are recorded at the peak time, as shown in Figure 5-12a for a zoom-view of a truck strain response. The peak responses from the steel gages are used to develop a best fit linear strain profile using least squares methods, as seen by Figure 5-12b. The concrete gage is mainly used for verifying strain continuity. Also, if composite action is not present, the concrete gage would be inappropriate for the line fit. If the fit is good (*e.g.*, $r^2 > 0.95$), the neutral axis is recorded as the height corresponding to zero strain (indicated at 47 inches in Figure 5-12b). Goodness of fit is used as a filter against the inevitable processing of faulty signals during automation as well as misclassified signals. The long-term result of neutral axis estimation is

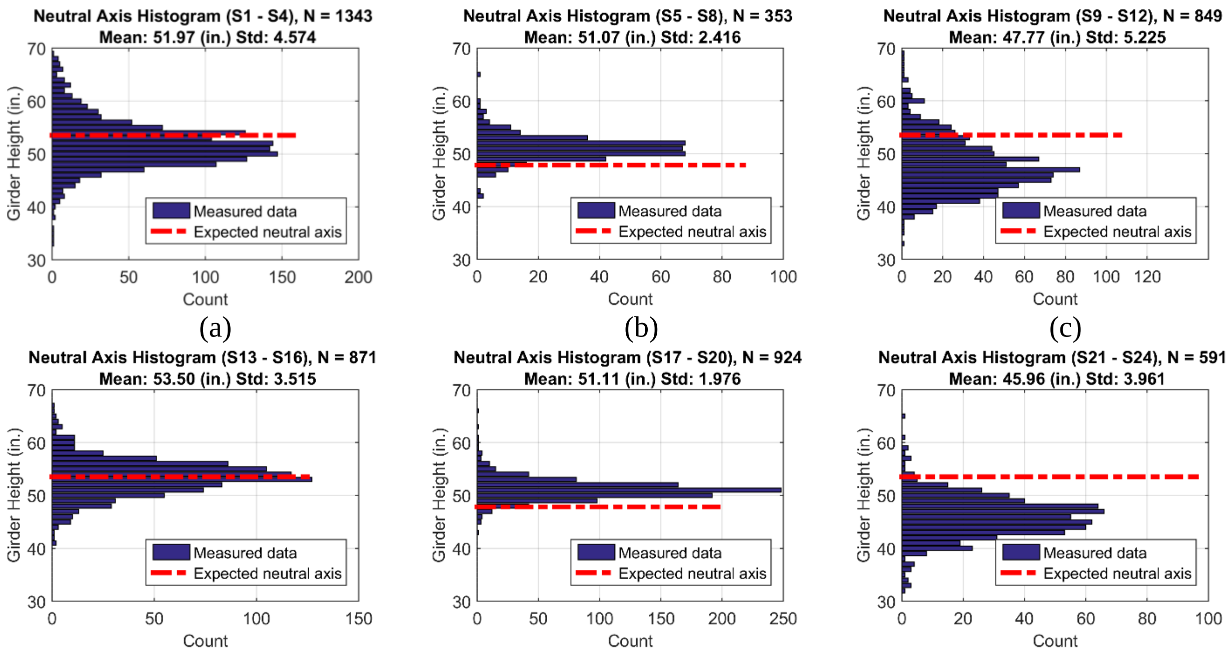

(a) (b) (c)

(d) (e) (f)

Figure 5-13. Neutral axis estimation histograms shown with expected neutral axis (dashed line) at all six measurement locations (a) S1-S4 (b) S5-S8 (c) S9-S12 (d) S13-S16 (e) S17-S20 (f) S21-S24.

shown in Figure 5-13 by histograms in relation to the expected neutral axis position as calculated from design drawings assuming complete composite action; expected neutral axis is shown by dashed lines. The following observations are made: 1) center span locations (S5 – S8 and S17 – S20) show the lowest variance in neutral axis estimation and consistently measure above the expected neutral axis position; 2) end-span locations show higher variance in the neutral axis estimation. Deck sections S1 – S4, S9 – S12 and S21 – S24 measure neutral axis estimations lower than the expected; 3) the S13 – S16 location measures neutral axis near the expected height for full composite action. Time-history data at S13 – S16 consistently reinforces good composite action behavior as well. A reasonable explanation for lower mid-span uncertainty is that the TRB is designed with shear studs in the mid-span section only. End-spans were not designed with shear studs due to low anticipated stresses and negative bending regions. Also, the mid-span gages

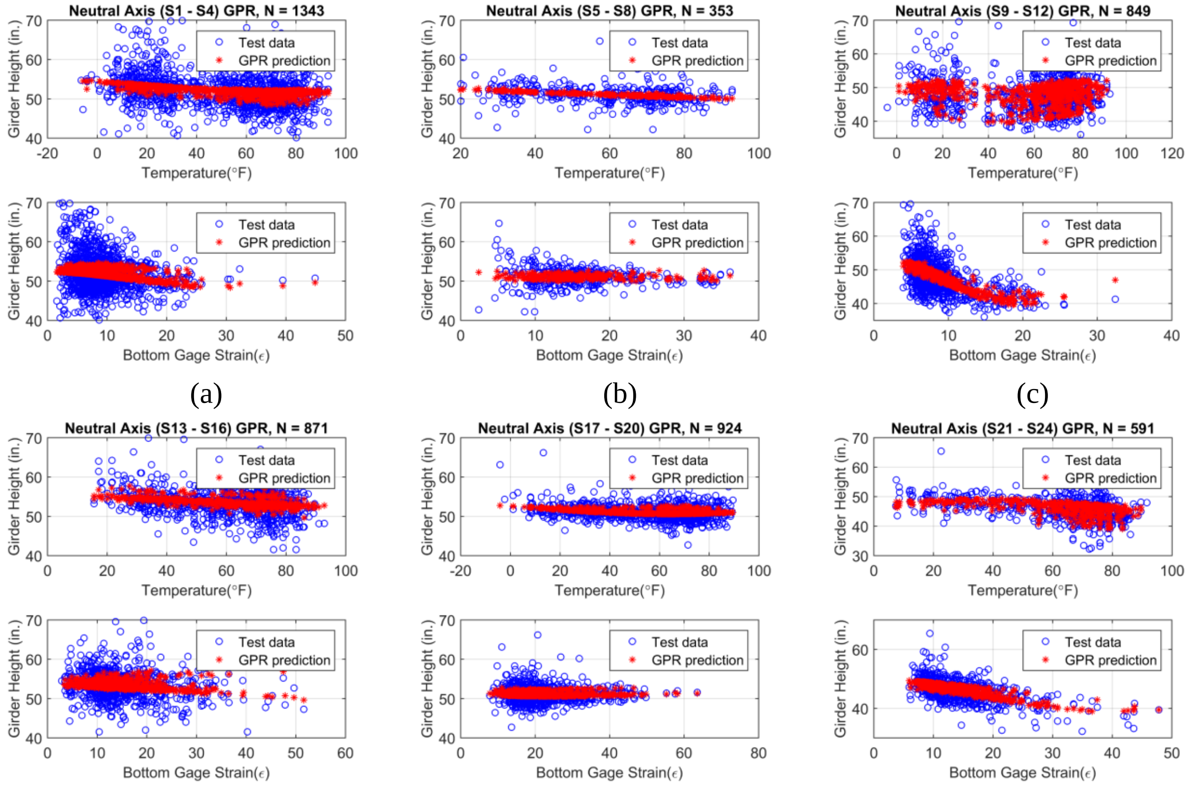

(a) (b) (c)

(d) (e) (f)

Figure 5-14. Neutral axis estimations (circle marker) versus temperature and bottom web strain (proxy for load magnitude) with GPR prediction (star marker) for (a) S1-S4 (b) S5-S8 (c) S9-S12 (d) S13-S16 (e) S17-S20 (f) S21-S24.

experience higher strain amplitudes than the end span gages, resulting in higher SNR and possibly better neutral axis estimation.

Neutral axis location is a section property, and as such is expected to be insensitive to temperature and acceleration measures. However, slight dependencies were observed at several locations so GPR modeling was performed. Figure 5-14 shows neutral axis girder height estimation versus temperature and bottom gage strain (a proxy for load magnitude). At the center span locations where good composite action is expected and shear studs reinforce the behavior, the influence of temperature and load are not very evident. Slight temperature dependence can be seen for locations S1 – S4, S13 – S16 and S21 – S24. Load dependence can be observed for locations S9 – S12 and S21 – S24. A recurring observation is also that response variance is reduced

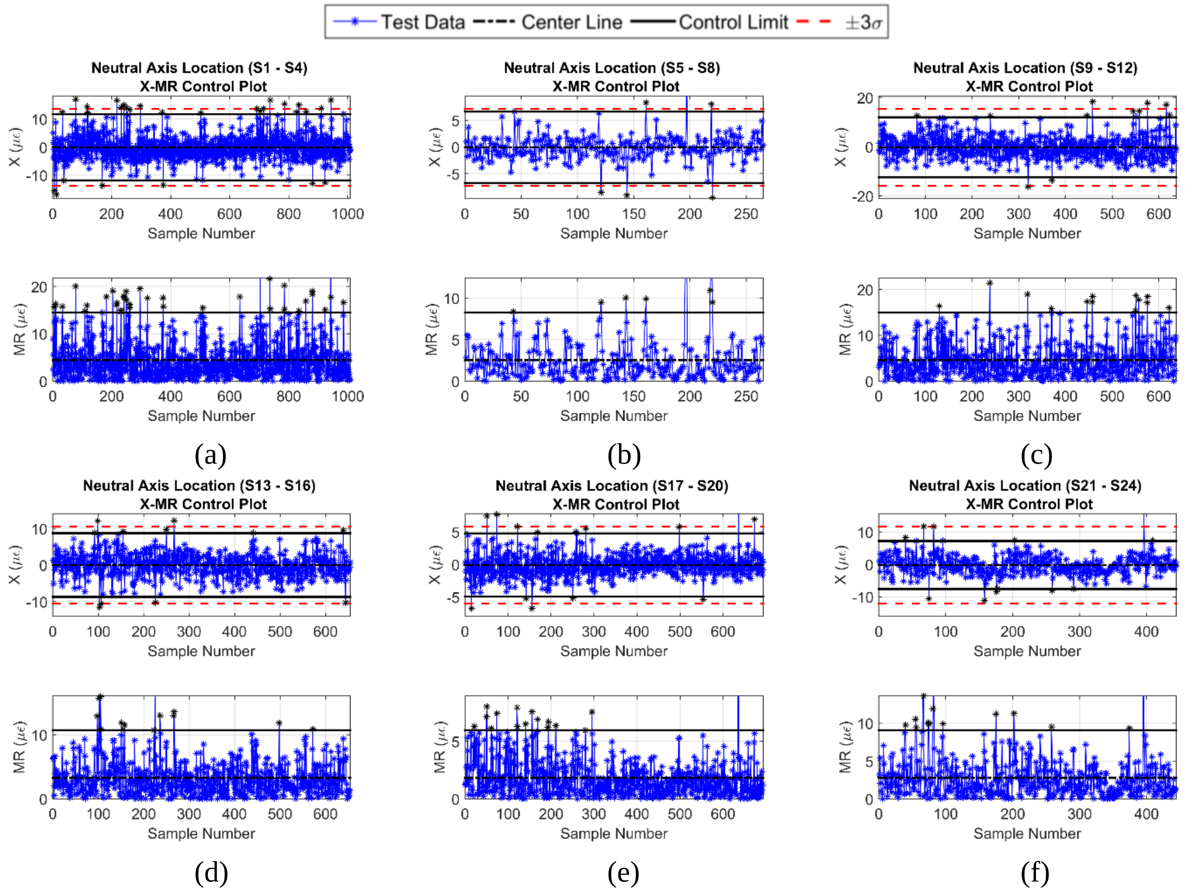

(a) (b) (c) (d) (e) (f)

Figure 5-15. X-MR control charts of neutral axis difference measures (measured – GPR predicted) for (a) S1-S4 (b) S5-S8 (c) S9-S12 (d) S13-S16 (e) S17-S20 (f) S21-S24.

for higher strains. This may be due to less data at these strain levels. It may also be explained by initial slippage at the steel-concrete interface for non-shear stud locations. Figure 5-15 shows the resulting $X - MR$ control plots for measured neutral axis height minus predicted neutral axis height. Standard limits using scaled moving range mean value (5.16 & 5.17) as well as normal distribution fit ±3σ are shown. MR plots show a higher incidence of threshold crossing (similar with previous control charts). Again here, loss of composite action will likely lead to a slow moving change in neutral axis position towards the steel centroid. In this case, a mean value trend would be easily detectable from the X control chart, allowing bridge managers an early indication of section strength losses. The fact that partial interaction is shown for the areas of the deck historically suffering significant surface damage is interesting; a new ability to investigate correlations in deck deterioration (cracking, spalling) with neutral axis movement is possible with the proposed framework.

5.4 Conclusion

The TRB monitoring system leverages embedded processing capabilities of wireless sensors to process light computational tasks as well as the *SenStore* data management framework to store and process bigger computing tasks such as machine learning, classification and regression. Performance monitoring of four targeted processes were demonstrated here to address the needs of MDOT for pin and hanger bridges. Link plate bending, link plate fatigue, thermal expansion and composite action behavior are all observed. In-plane and out-of-plane bending strains were measured at peak strain locations as located by a support vector classifier built from a small supervised subset of TRB data. Using the SVC, long-term collection of peak strains and corresponding peak accelerations were made. Peak accelerations were used a load proxy to characterize strain sensitivity to load magnitude. GPR was used to model the relationship between acceleration and strain and later used to predict strains given acceleration data. Partial pin-hanger resistance to rotation was observed by a positive correlation in in-plane strain with acceleration. Difference measures were plotted in $X - MR$ control plots to determine performance thresholds for future long-term performance monitoring. An AASHTO based remaining fatigue life procedure was implemented which utilizes strain cycle histograms computed on-board the *Narada* wireless sensor. Fatigue was determined to be of no concern as hanger stresses are observed to be well below fatigue thresholds. Specifically, maximum effective stresses of approximately 0.3 ksi were observed while the fatigue threshold is 1.6 ksi. Bridge beam-end contact was monitored by static deck strain measures to capture thermal expansion performance. Thermal strain consistent with temperature change over the complete temperature profile indicates free expansion; a cease in thermal expansion as temperatures rise would indicate beam-end contact. Daily temperature fluctuations were observed to cause a cyclic response of strain versus temperature (rather than following a linear path for expansion and contraction) requiring a second regression input be used (time of day and temperature). The SPC control limits contain the majority of the deck strain measures and serve to easily identify a drift in deck strain due to beam-end contact. Ideally, beam-end contact could be identified in an early stage so that significant damage was not introduced. Composite action performance is characterized by an estimated neutral axis position from four strain gages configured at six deck section locations. Only the center span section of the bridge was designed with shear studs for a strong design intention of composite action. Therefore, center span neutral axis estimations are better behaved (show less variance and meet neutral axis criteria for composite action) than the end span measures. Neutral axis was predicted using temperature and bottom strain magnitude (as a proxy for load magnitude). Difference measures between measured and predicted were used to design a $X - MR$ control plot to automatically detect a drop in neutral axis position due to loss of composite action. The TRB has historically had more deck surface damage in regions of partial composite action. The proposed framework could establish a link between position or movement of the neutral axis position and deck surface damage if that correlation exists.

CHAPTER 6.

LONG-TERM MONITORING OF PIN AND HANGER ASSEMBLIES FOR RELIABILITY-BASED ASSET MANAGEMENT

6.1 Introduction

The problems arising from pin and hanger details have been well documented. The Mianus River Bridge in Greenwich, CT collapsed in 1983 from a failed pin and hanger detail coupled with a lack of redundancy. The National Transportation Safety Board (NTSB) highway accident report [9] found that the probable cause was undetected lateral displacement of the hanger plate caused by corrosion-induced forces. In 1978, the St. Clair River bridge in Illinois had several fracture hanger plates due to high stress from in-plane bending caused by corrosion induced pin-plate fixity [10]. The span did not collapse due to redundancy but did experience a drop in the bridge deck by as much as 19 mm. Juntunen [7] reported on a Michigan Department of Transportation study to observe live loading in existing pin and hanger details. Several pin and hanger bridges were instrumented for live load measurement and several problems were discovered including corrosion, beam-end contact and a fractured link plate. Three types of loading were observed: axial, in-plane (strong-axis) and out-of-plane (weak-axis). Fatigue analyses were conducted per AASHTO remaining fatigue life methods. The report recommended to inspectors that suspected cracking should be verified by ultrasonic inspection and if found the link plate should be replaced and the cause should be determined. Furthermore, heavily corroded link plates should be replaced, bridge distress from beam-end contact should be searched for and if found relief action be taken. It was also recommended that non-redundant link plate bridges be inspected annually and kept in excellent condition and that further research should be done to show that fatigue category E is appropriate. Another MDOT report [107] suggests that the effects on stress distribution and capacity of link plates having corrosion induced section loss should be investigated. The Illinois Department of Transportation conducted a study to evaluate the effects of fixity in pinned supports for cantilever truss and girder bridges, including a pin and hanger design similar to the TRB [8]. They summarized that among the several methods used to field test pin connection behavior that strain gages and electronic rotation sensors were the most suitable. Among the conclusions of this study were that strain gage circuits instrumented on hangers can be used to quantitatively measure the effects of pin fixity, cantilever bridge pin and hangers may experience yielding under complete fixity and partial fixity can result in damage to hangers.

Currently, ultrasonic inspection is the preferred method for advanced in-service inspection of pins for cracking [189-191]. Although ultrasonic inspection has shown to be a successful NDE method for crack detection in pins, few NDE methods have been proposed for pre-crack detection, and no long-term sensing efforts have been made for condition monitoring. Clark *et al.* [189] proposed use of ultrasonic methods to measure hanger stress and indicate potential crack behavior. They developed a test specimen to simulate a hanger with a single locked pin to validate their proposed method. Their model results agreed with strain gage readings within 5 to 55 $\mu\varepsilon$ for different measurement scenarios. Houcque [192] conducted a finite element based investigation of pin and hanger integrity and developed a crack growth model for the joint. The FE model was used for stress analysis, thermal effect, mixed mode stress intensity factor determination and fatigue crack growth simulation. While failure of the pin and hanger detail can be catastrophic, the onset of failure is slow for fatigue cracking, yielding due to section loss and yielding due to frozen pins. Structural monitoring techniques may pose an economic advantage to pin and hanger management by alerting officials of life reducing behavior before significant and costly damage is done.

The goal of this study is to establish a long-term condition monitoring program for early detection of damage inducing conditions in pin and hanger assemblies using an FE model, reliability metrics and section area estimations. First, an FE model capable of simulating progressive pin locking is developed to characterize sensor response sensitivity to increasing lock-up conditions. Second, long-term sensor data is used to build statistical models of hanger strain response to live loads. The measured data is used to evaluate pin and hanger limit states and subsequent reliability index calculations. Net-section area estimations are made using a ratiometric measure of hanger strains. The sensing strategy targets observation of plate bending and net-section stresses.

Pin and hanger performance monitoring and damage detection is performed using strain gage response from operational pin and hanger assemblies on the Telegraph Road Bridge (TRB). The TRB was constructed in 1973 and had the original pin and hanger assemblies replaced in 1988. Corrosion is evident around the assemblies today and recent inspection reports cite the possibility that some assemblies may be frozen. Strain gages and accelerometers permanently installed to the pin and hanger detail are used to feed a reliability index calculation. A FE model is built to validate the sensor strategy and to characterize the sensitivity of vibration and strain responses to pin and hanger “lock-up” by adjusting the friction coefficient at the pin-plate contact surface. The reliability index monitoring framework supports the forward trend of risk-based asset management. Yield limit states for pin shear and hanger net-section tension are evaluated using

(b)

(a) (c)

Figure 6-1. Pin and hanger detail (a) shown in-service suspending middle span girder from end span girder and shown removed due to extensive corrosion damage to the (b) outside (c) inside face

strain gage responses. Long-term performance of the pin and hanger assembly in terms of reliability index is proposed and demonstrated from August, 2014 to June, 2015 for the two yield limit states. In addition to the reliability evaluations, strain gages are also used to estimate hanger net-section area as a long-term capacity measure. Each goal is geared towards long-term condition monitoring of the pin and hanger assembly for early detection of corrosion section loss and corrosion build-up. This approach to pin and hanger evaluation complements currently utilized VI and NDE fracture detection methods.

6.2 Pin and Hanger Detail

The pin and hanger detail became a popular design for bridges between 1940 and 1980. The design was discontinued in Michigan around 1981 [107] but many of the already in-service pin and hanger bridges still operate today. The pin and hanger design provides several advantages including the ability to accommodate thermal expansion, reduced moments near pier supports, simplified design calculations and an expansion joint away from piers and bearing which reduces corrosion to bearing elements (shown in Figure 6-1a). However, as mentioned previously, the pin and hanger detail has revealed over time to have several vulnerabilities. Introduction of corrosion between the pin and plate, as well as between the plate and girder, can cause unexpected stress fields that can reduce the capacity of the pin and hanger elements as well as increase the demands being placed on them. For the extreme case of a fully fixed pin-plate mechanism where rotation is not allowed, large shear and torsional forces can be introduced to the hangers and pins, especially due to large displacement thermal expansion [192]. Figure 6-1b shows severe corrosion section loss to the back side of a hanger plate; this type of damage would be undetectable by VI.

The introduction of water and salt from leaky expansion joints has been a main contributor to the field's move away from using pin and hanger details. As water and salts drip from the deck above and settle into the bottom pin-plate interface region, corrosion starts to occur and build up. Two potentially catastrophic behaviors of the pin and hanger assembly due to corrosion build-up are: 1) partial (or complete) fixity that induces plate bending and pin torsion, and 2) "walking" of the plate outward towards the open end of the pin. The first consequence can induce large shear stresses at the pin surface and increased net-section stresses in the hanger. Under fully locked conditions and large thermal expansion, FE results have shown pin shear reaching yield stress [192]. The second consequence is also attributed largely to sway displacements and misaligned bridge spans. Pin and hanger details provide very little lateral support for the suspended span, and since they have very little damping capability can result in ten to fifteen out-of-plane bending fatigue cycles per truck [7]. The strain gage instrumentation program is designed to address the concerns of the pin and hanger assembly.

6.3 Telegraph Road Bridge Instrumentation Program

Although the TRB is quite redundant to catastrophic pin and hanger failure (the TRB carries seven girder lines), there are several fracture critical pin and hanger bridges in the state of

Michigan making the TRB an excellent testbed for developing pin and hanger health assessment strategies. There are two main objectives of the measurement program. The first objective is to measure strains which can be used to evaluate important limit state equations used in design of pin and hanger assemblies (*e.g.*, hanger net-section tension, pin shear). The second objective is to estimate net-section area using strain gages and provide a capacity performance measure. As corrosion deterioration grows in the pin-hole region, the net-section area estimation would expectedly decline and be an early indicator of excessive corrosion and the onset of torsional stresses and increased net-section stresses. Both objectives are intended to indicate a modified boundary condition in the pin and hanger mechanism, and as such serve as an early indicator of a progression towards future damage. To realize the abovementioned objectives, two pin and hanger assemblies were instrumented with eight strain gages. The current pin and hanger implementation has been providing data since August, 2014. The two hanger assemblies currently in-service are located on the east side hanger line of the TRB at girder lines two and six (G2, G6). The eight strain gages are strategically positioned on hangers for expected behaviors under corrosion locking and section loss. The strain gage layout can be seen in Figure 2-6 with strain gages labeled #1–#8. Strain gage details as well as measurement interface details are described in Chapter 2.

Steel hanger plates and pins are made from ASTM A588 steel and ASTM A108 steel, respectively. Both materials carry a minimum yield strength of 50 ksi (345 MPa) and are assumed to have a 29,000 ksi (200 GPa) modulus of elasticity, 11,600 ksi (80 GPa) shear modulus and Poisson’s ratio of 0.29. Steel hanger plates measure 42 in (106.68 cm) long, have a center-to-center hole length of 31 in (78.74 cm), are 10 in (25.4 cm) wide, $1\frac{1}{4}$ in (3.18 cm) thick and have a hole diameters of $5\frac{1}{32}$ in (12.78 cm). Steel pins measure 7 in (17.78 cm) long and have barrel diameter of 5 in (12.7 cm).


(a) (b) (c) (d)

Figure 6-2. TRB strain gage instrumentation (a) mid-plate rosette (b) near-hole and right side plate (c) left side plate and (d) installed wireless DAQ system

The gage layout is intended to measure strain locations in the hanger plate which are particularly sensitive to axial, in-plane bending and out-of-plane bending deformations and to infer torsional forces applied to the pins. For the in-plane bending shown in Figure 2-6, equal and opposite moments in the plates are expected at the top and bottom pins. In-plane strain gages provide bending strain information to make the moment estimation. Figure 6-2 shows sensor instrumentation used in this study as installed on the TRB. Figure 6-2a – Figure 6-2c shows installed strain gage sensors used. Figure 6-2d shows the complete sensor system with permanently installed wireless DAQ hardware. All TRB data acquisition is performed using the *Narada* wireless sensor [51].

6.4 FE Model

A finite element model was generated for the pin and hanger assembly region in order to validate sensor placement and notions of corrosion influence on measured data in the hopes of getting high resolution information. Abaqus [193] is used to model a typical pin and hanger assembly as specified by original design drawings for the TRB provided by MDOT. Hanger elements are meshed using standard 8-node linear brick reduced integration elements (C3D8R); pins use linear wedge elements (C3D6). The entire assembly contains 60,612 elements. The


(a) (b)

Figure 6-3. Link plate model (a) assembly and (b) meshing

assembly and meshing of the pin and hanger model are shown in Figure 6-3a and Figure 6-3b, respectively. Since the pin-plate interface behavior is critical to this study, special attention was given to the construction of the region. Partitions were made in plate regions near the pin holes to allow well-structured meshing in the region. These regions were meshed with a finer grid than the rest of the model since these regions experience the largest rate of stress change for the applied loads. The pins were also partitioned for better structured meshing and meshed with a fine grid in the hopes that the modeling provides sufficient detail for accurate surface-to-surface contact interaction. The matter of corrosion in the pin-plate mechanism is a challenge to model. To simulate progressive locking conditions, Coulomb friction is introduced to the contact surfaces of the pin and plate. The friction parameter between the pin and plate surface was varied between 0.1 and 1.0. Static friction coefficients for hard steel on steel contact has been listed as approximately 0.1 for lubricated and 0.8 for dry, clean surface [194]. The outer surface of the pin (master) and inner surface of the plate hole (slave) are defined as contact surfaces, with a hard normal interaction and friction tangential interaction. Two interaction options are available, small sliding and finite sliding. Small sliding is limited to small relative displacements and is less

(a) (b)

Figure 6-4. Link plate dead load validation testing showing (a) von Mises stress distribution and (b) pin hole deformation (largely exaggerated) with stress concentration

computational. Finite sliding was used here as large relative displacements may be required and since relative displacement behavior is so important to the surface friction influence. Rather than simplify the model to a single hanger plate with constraints on the hole region, a model which includes two hangers, two pins and truncated girders were used. Both hanger plates and girders were used to ensure a load application from the pin to the hangers which closely resembles the built structure. Pins were used to resemble an accurate constraint to hole deformation in the plate section. The various parts of the model (pins, plates, girders) are mostly contained by surface contact friction; free rotation is regarded as tangential friction, $\mu = 0.1$.

For validation, three criteria were checked under free rotation and zero section loss. First, normal stress at the hanger plate gross section was confirmed for the expected bridge dead load. Typical stress field response and pin-hole region deformation for dead load are shown in Figure 6-4a and Figure 6-4b, respectively. Particularly noticeable in Figure 6-4b is the stress concentration and pin-hole deformation. Second, stress concentration near the pin-hole was compared against a value range of $k = 2.13$ [195] and $k = 2.25$ [196] for the TRB hanger plate dimensions with an open hole and tight-fitting pin-loaded hole, respectively. Third, the first modal frequency was observed for the out-of-plane bending mode. It is expected that the pins create a boundary condition close to fixed-fixed for out-of-plane bending as the pins are tight fitting and

Table 6-1. FE model validation results

Validation Step	Analytical Result	FE Result	Experimental Result
DL gross (ksi)	3.21	3.21	N/A
DL net (ksi)	13.67 (k=2.13)	13.37 (k=2.08)	N/A
Mode 1,2 (Hz)	105-240	175.2	189

limit out-of-plane rotation of the plate at the hole location. Frequencies were calculated analytically to be between 105 Hz and 240 Hz for pinned-pinned and fixed-fixed boundary conditions respectively. Impulse hammer testing directed in the out-of-plane direction was performed on a TRB hanger plate resulting in a dominant frequency of 189 Hz. The analytical results of the dead load and vibration validation analyses are all in close agreement with the FE model and the TRB experimental testing as seen in Table 6-1.

Following validation testing, a set of experiments were conducted to observe vibration and strain sensitivity to increased interface tangential friction. First, modal frequencies were observed for a tangential friction coefficient μ, ranging from 0.1 (lubricated) to 1.0 (dry, clean) at the pin-plate interface surface. The results of the simulations can be seen in Figure 6-5 for 1st mode bending (out-of-plane), 1st mode torsion (out-of-plane), 2nd bending (out-of-plane), 1st bending (in-plane), 2nd torsion (out-of-plane). In particular, in Figure 6-5a absolute modal frequency is plotted

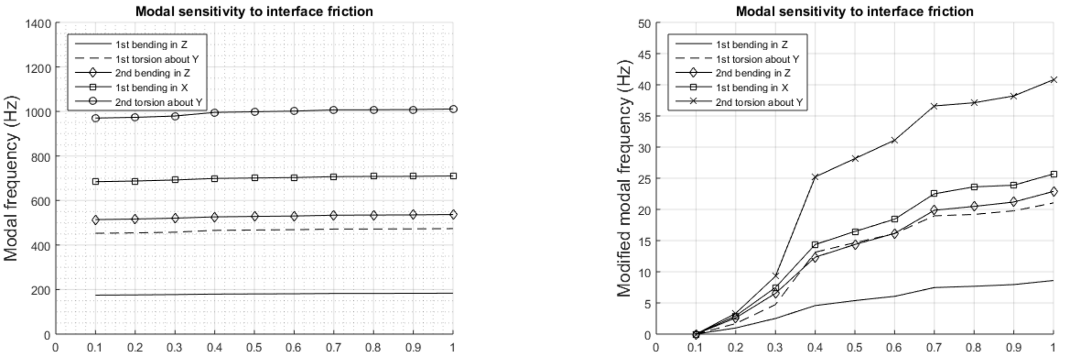

(a) (b)

Figure 6-5. FE modeled link plate mode frequency vs surface friction coefficient (a) absolute frequency (b) μ=0.1 centered frequency

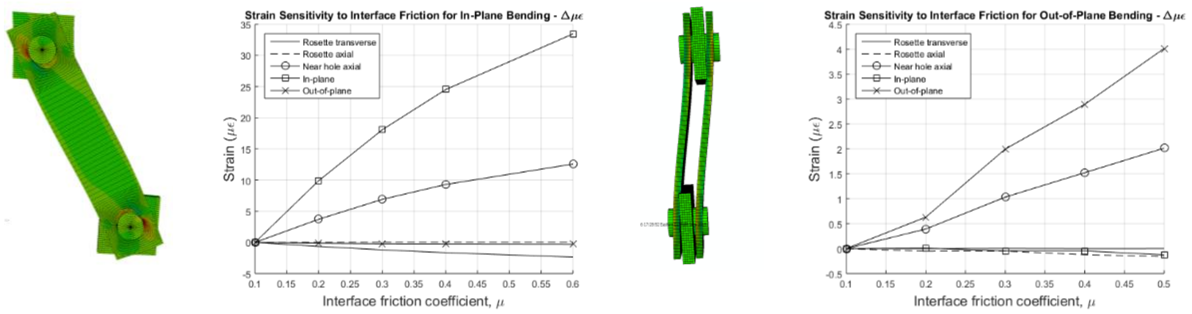

(a) (b)

Figure 6-6. FE strain response to targeted behavior at TRB installed strain gage locations

against the FE model tangential friction coefficient. In Figure 6-5b, modal frequencies are centered by their $\mu = 0.1$ result to shows more closely each mode's relative sensitivity to the friction coefficient. From this view it is easy to see how much each mode varies in absolute frequency (Hz) due to varying friction (implied varying corrosion). At a friction coefficient of $\mu = 1.0$, modal frequency is shown to change between 10 and 40 Hz from $\mu = 0.1$; such frequency changes would be measured with high resolution from the *Narada*. The sensitivity of friction to plate strains was also observed. Of particular interest was the sensitivity of the TRB instrumentation to in-plane and out-of-plane bending for varying corrosion levels. In-plane and out-of-plane bending simulations were performed by prescribing a constant displacement on the bottom pin for varying levels of interface friction. The results of the simulations are shown in Figure 6-6a for in-plane displacement and Figure 6-6b for out-of-plane displacement. In similar fashion to the modal results in Figure 6-5b, strain gage responses are centered at the $\mu = 0.1$ result to observe relative strains rather than absolute strains. The strain responses shown are rosette transverse (gage #1), rosette axial (gage #3), near hole axial (gage #4), in-plane (gage #6 – gage #8) and out-of-plane (gage #5 – gage #7). As expected, strain gage response with most sensitivity to in-plane and out-of-plane displacements under corrosion build-up are the TRB configurations for in-plane and out-of-plane bending, respectively. The vibration and strain corrosion sensitivity studies are an attempt to reinforce the TRB sensing scheme for monitoring progressive locking behavior and to enable future studies fusing acceleration and strain gage measurements. Currently, work is in progress using acceleration measures from the top and bottom pins as input to the FE model and validating FE strain response with TRB strain gage response. Accelerometers on the plates for local vibration monitoring may be a direct measure of boundary conditions (*i.e.*, damage) given the simple make-up of the pin and hanger assembly.

The FE model has been validated for use in several ways and the TRB sensing scheme has been reinforced. The remainder of this chapter focuses on long-term strain gage data acquired at the TRB with the abovementioned sensing scheme for statistical parameter extraction and reliability assessment on yield limit state functions relevant to pin and hanger design.

6.5 Long-Term Reliability Based Condition Monitoring

Structural reliability refers to a structures ability to meet the demands it was designed for. In order to assess the reliability of a structure, failure to meet demands needs to be defined. Failure modes may come in the form strength criteria (*e.g.*, stress limit) or serviceability criteria (*e.g.*, deflection limit) for example, and are often defined through design criteria in the form of limit state functions. For the safety of structures, capacity, C, should exceed demand, D. The safety margin, $M = g(X) = C - D$, where X is a vector of random variables describing capacity and demand behavior, indicates whether or not failure is considered (*i.e.*, $M \leq 0$, indicates failure). The probability of failure is the probability that demand exceeds capacity, or $P(C - D \leq 0)$ and the definition of reliability, R, is the probability that the structure does not fail, or $R = 1 - P_f$. In the simple case that the random variables which comprise the failure function are independent, normally distributed and the failure function is linear in the random variables, then the probability of failure is given as $P_f = \Phi(-\beta)$, where the reliability index β is defined as,

$$\beta = \frac{\mu_M}{\sigma_M} = \frac{\mu_C - \mu_D}{\sqrt{\sigma_C^2 + \sigma_D^2}} \tag{6.1}$$

[93]. In this study, two yield limit state functions are considered which utilize the strain gage configuration designed for the TRB hanger plates. Limit states are evaluated for reliability index using TRB data. Among the goals of this study is to establish a continuous reliability monitoring program for pin and hanger assemblies approaching new performance- and risk-based asset management goals for the U.S. infrastructure.

6.5.1 Pin and Hanger Limit states

Hanger net-section tension and pin shear limit states are considered for pin and hanger reliability monitoring. Fatigue limit states are not evaluated since infinite fatigue life stress levels have been reported previously in Chapter 5. However, in general, the fatigue reliability of pin and hanger assemblies should be considered. Pin and hanger strains are converted to stresses with the assumption that Hooke's law applies and assessed against yield stress limits. The axial tension limit for the net-section is taken directly from strain gage #4. Combined effects from axial and bending loading will be observed at the gage location. It was recommended [107] that general yielding be evaluated at the net-section and to ignore stress concentrations. The FE model suggests that the gage #4 location is a good representation of the average net-section stress since it is approximately mid-way between the hole edge and the plate edge. Also, strain gage #4 is instrumented in the exact region being evaluated so it has the added benefit of experiencing all potential combined stresses in the link plate. The limit state function is given as

$$g(X) = C - D = 0 \tag{6.2}$$

where D, the average stress in the net-section area is the load variable and C, the yield stress is the resistance variable. The load variable, D, is calculated as

$$D = \frac{DL + LL}{A_{net}} = \frac{DL}{A_{net}} + \varepsilon_{H4} \cdot E \tag{6.3}$$

where, the net-section axial stress is calculated using dead load, DL, live load, LL, and net-section area, A_{net}. The dead load, yield stress and elastic modulus are considered lognormal random variables given in Table 6-2, obtained from compiled statistical information on steel properties. Yield stress and elastic modulus RV parameters are obtained from compiled statistical information on steel properties [197]. Dead load stress mean value is estimated using design drawings with the assumption that deck weight, including parapet estimations, are uniformly distributed among the seven girder lines while standard deviation is calculated using a coefficient of variation of 10%; it was suggested in [198] to use dead load $COV = 0.08$ for factory-made elements and $COV = 0.10$ for cast-in-place elements. Live load distribution parameters are extracted from measured data at strain gage #4. Figure 6-7a and Figure 6-7b show long-term statistics for peak strain at strain gages #3 and #4, respectively, due to the maximum load event for each one-minute monitoring period. Strain gage #3 is shown as a validation measurement to the net-section strain gage. Since general yielding criteria ignores stress concentrations, when strain gage #3 is factored by the gross section/net-section area ratio it will provide good validation of the net-section average strain response. However, strain gage #4 is used for reliability estimation as only the net-section strain gage will increase for corrosion induced section loss. Maximum load response statistical behavior closely resemble the generalized extreme value (GEV) distribution having mean $\mu = 5.25\ \mu\varepsilon$, standard deviation $\sigma = 4.31\ \mu\varepsilon$ and $k = 0.43$ as shown by GEV fit dashed line overlays in Figure 6-7a and Figure 6-7b. The convenient calculation for reliability index shown previously is no longer valid since the basic random variables are a non-normal mixture. In order to handle the mixture of lognormal and GEV RV's, a Monte Carlo simulation (MCS) approach to determining probability of failure, P_f, is used, and subsequent reliability index, β, is estimated using the normal distribution. The basic algorithmic approach to MCS is 1) generate a random sample from the assumed distribution of the limit state random variables; 2) evaluate the limit state deterministically using the generated samples; 3) record the binary result (pass or fail); 3) repeat steps 1, 2 and 3 an appropriate number of times. After N iterations; 4) estimate P_f as ${}^{N_f}/_{N}$, where N_f is the number of failed limit state evaluations in step 2 and N is the total number of iterations. The convergence of P_f should be monitored to determine the appropriate number of iterations. Since loads to measured hangers on the TRB are well below the yield limit, probability of failure

Table 6-2. Random variable parameters used for reliability evaluation

Random Variable	Mean	COV	Distribution
Yield stress, (ksi)	49.6	0.089	Lognormal
Elastic Modulus, E (ksi)	29696	0.018	Lognormal
DL (kip)	43	0.100	Lognormal

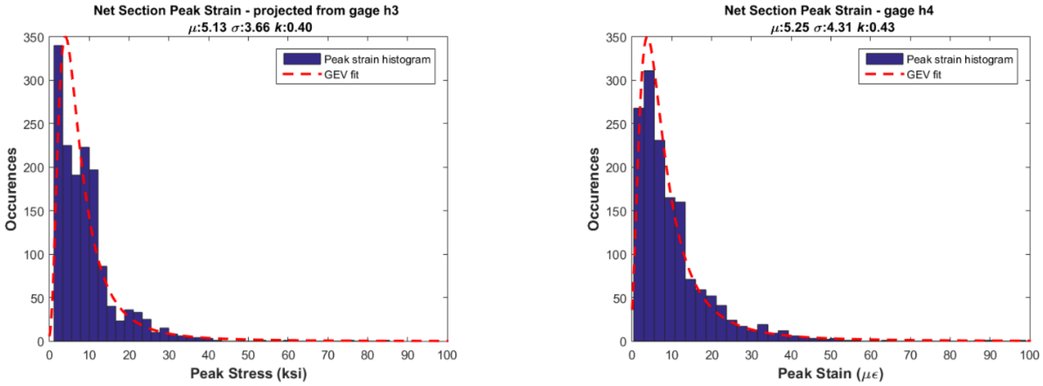

(a) (b)

Figure 6-7. Peak strains for traffic loads (a) projected to the net-section from mid-plate strain gage h3 and (b) from net-section strain gage h4 measurements

is quite low requiring many iterations for MCS. Here, $1e7$ iterations is selected resulting in a $P_f =$ $1.01e$-5 and $\beta = 4.26$ for the entire data history.

For the pin shear limit, a similar procedure is followed. The load transfer of the suspended span dead load and live load to the pin and hangers results in two shear planes. Additionally, for partial or full fixity, torsional stress is introduced having the relation $\tau = \frac{T\rho}{J}$ where T is applied torque, ρ is the distance from the pin center to the evaluation point and J is the polar moment of inertia. Here, dead load and live load is desired (rather than net-section stress) so strain gage #3 is used to estimate LL supported by the pin as it best resembles average tensile stress in the hanger. The shear stress in the pin due to transverse shear is parabolically distributed with maximum shear occurring at the neutral axis having value $\tau_{max} = \frac{4V}{3A}$ or $\tau_{max} = 1.33 \cdot \tau_{avg}$ where τ_{avg} is the average shear stress. Torsion load applied to the pin is determined using hanger strains #6 and #8 (ε_{H6} and ε_{H8}) to calculate moment in the hanger at the pin connection. The shear stress in the pin due to torque from the plate increases linearly from the pin center to the outer edge with maximum shear stress observed at the outer edge where ρ is equal to the pin radius, c. Shear stress

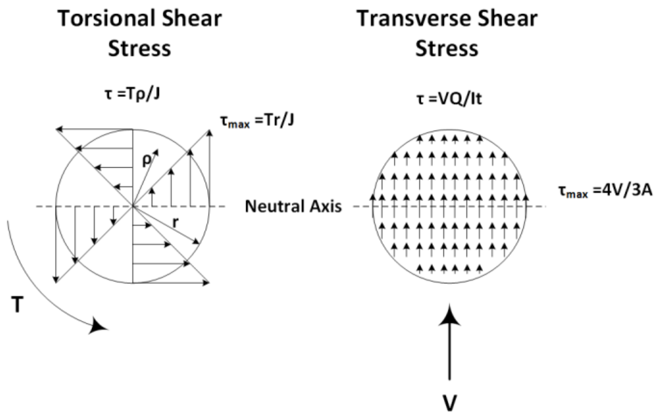

Figure 6-8. Shear stress distribution for transverse and torsional shear in a circular section

distributions for transverse and torsional shear are shown in Figure 6-8. The polar moment of inertia for a solid shaft is defined as $J = \frac{\pi}{2}(c^4)$. The total maximum shear stress is given as

$$S = \frac{DL + LL}{A_{pin}} \cdot \left(\frac{4}{3}\right) + \frac{T\rho}{J} \tag{6.4}$$

where

$$LL = \varepsilon_{H3} \cdot E \cdot A_{plate} \tag{6.5}$$

and

$$T = M = \frac{\sigma}{y} \cdot I = \frac{(\varepsilon_{H6} - \varepsilon_{H8}) \cdot E}{2} \cdot \frac{2}{h} \cdot \left(\frac{1}{12} bh^3\right) \tag{6.6}$$

including elastic modulus, E, plate cross-sectional area, A_{plate}, pin cross-sectional area, A_{pin}, plate width, h, plate thickness, b and pin radius, c. Plate and pin dimensions should be evaluated with some uncertainty but for simplicity here they are assumed deterministic and based on field measurements. The shear yield stress is given as $F_v = 0.60F_y$ with the same uncertainty as the yield stress given in Table 6-2. Figure 6-9 shows long-term results for peak shear stress demand from each one-minute data collection taken since August, 2014. Again, maximum load response statistical behavior resembles a GEV distribution having $\mu = 1.02\ \mu\varepsilon,\ \sigma = 0.70\ \mu\varepsilon$ and $k = 0.27$ as shown by the dashed line overlay in Figure 6-9. Monte Carlo methods are used in the complete time-history to estimate reliability index for this limit state, resulting in $\beta = 4.87$ ($P_f = 5.5e\text{-}7$) for $5e7$ iterations. Strain values also suggest that yield stress limits are far from being approached for the measured hangers and probability of failure is expected to be extremely low.

The fatigue limit state is not evaluated since effective stress in the hanger net-section is far below the constant amplitude fatigue threshold (CAFL) used for AASHTO fatigue life analysis. In Chapter 5, stress cycle histograms from rainflow counting on the hanger plates was presented in Figure 5-7 for the plate mid-section and plate net-section (gage #3 and gage #4). Effective stress is approximately 0.13 ksi at mid-plate and 0.27 ksi at the net-section; the CAFL for fatigue category E is 4.5 ksi. Examples of a reliability evaluation for fatigue life using monitored data can be found in literature [199, 200].

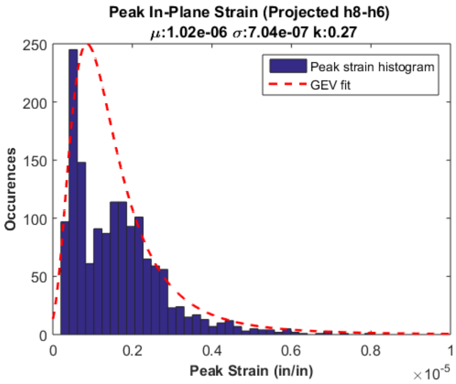

Figure 6-9. Peak shear stress histogram from TRB hanger pins due to traffic loading

Reliability index should be viewed as time-varying since the net-section is degrading with age and corrosion and traffic demands may increase over time. As such, the goal here is to develop reliability index time-history results for bridge managers to utilize towards performance- and risk-based criteria.

6.6 Net-Section Area Monitoring

The main goal of this study is to provide early detection of degrading conditions in pin and hanger assemblies before safety margins have eroded to the point of expensive repairs. At the heart of this goal for pin and hanger assemblies is early indication of corrosion build up in the pin-plate area since section loss and lock-up can significantly reduce safety margins. Corrosion is usually concentrated in the bottom pin-hole region as seen by the severe pitting in Figure 6-1c while the middle plate region is least affected. This of course is not a certain fact but an observation made from failed samples (Figure 6-1c) and intuition. This observation will allow for an introductory method for net-section area estimation with a reduced amount of uncertainty as the middle plate dimensions can be taken reliably from design drawings, manufacturer specifications and even field measurements and the middle plate strain gage is used as a reference sensor for net-section strains. In the case of the TRB, the hanger net-section area is exactly one half of the gross section area, leading to an expected strain ratio of 2 without considering non-uniform stress field in the net-section region. The results of a finite element analysis of the pin and hanger assembly confirm that for the TRB strain gage location the net-section to gross section strain ratio is approximately 2 as the net-section strain gage is far enough from the hole edge to see a large stress concentration. The stress in the net-section at the strain gage location can be related to the stress in the gross section at mid-plate by the formula

$$\sigma_n = \sigma_g \cdot \frac{A_g}{A_n} \cdot k \qquad (6.7)$$

where σ_n is net-section stress, $\sigma_g$is gross section stress, $A_g$is gross section area, $A_n$is net-section area and k is the stress concentration factor at the strain gage location. Rearranging for net-section area and using Hooke's law to utilize strain gage readings directly, the following relation exists

$$A_n = A_g \cdot \frac{\varepsilon_g}{\varepsilon_n} \cdot k \qquad (6.8)$$

Where elastic modulus on top and bottom cancel out. Considering the case of $k = 1$ and using $A_g = 12.5\ in.$, the net-section area can be estimated with strain gage #3 and strain gage #4; the expected net-section are is $\frac{A_g}{2} = 6.25\ in.$ Figure 6-10a and Figure 6-10b shows long-term results for net-section area estimation using truck induced peak strains and free vibrations, respectively to determine the more appropriate signal processing methodology. Assuming that $k = 1$ is accurate, the free vibration approach for the first mode frequency appear to match the expected result more closely. Ideally though, both methods will display a decreasing trend for area estimation under section loss. An alternate method for monitoring the section area can also be made by directly observing the ratio of strain gage #3 to strain gage #4 with the realization that for section loss at the hole, not only will the stress increase due to reduced area but also the stress concentration will be moving closer to strain gage #4, amplifying the response even more. The sensitivity of the $\varepsilon_4/\varepsilon_3$ measure will increase as section loss spreads farther from the hole.

6.7 Conclusions

A method for continuous condition monitoring of pin and hanger assemblies was desired to complement current inspection techniques. Corrosion buildup is the main contributor to pin and

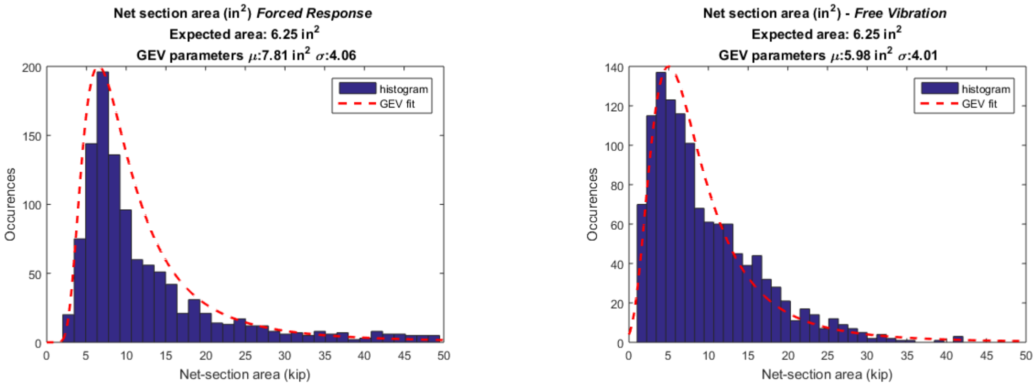

(a) (b)

Figure 6-10. Net-section area estimation by strain ratio for gage #3 and gage #4 processed by (a) peak strain amplitudes due to truck loading and (b) first mode vibration response in the frequency domain

hanger degradation and as such the sensing strategy and monitoring procedures were geared towards identifying assembly behavior for early stage corrosion. A FE model was first developed to investigate strain and local vibration sensitivity to progressively locking pin-plate joints. The effects of corrosion induced locking were simulated by adjusting the interface friction parameter at the pin-plate contact surface. FE modal vibration frequency increased with friction coefficient increase. In-plane strain measures showed the greatest sensitivity of all the strain measures to increasing friction for in-plane displacement controlled loading. Out-of-plane strain measures showed highest sensitivity to increasing friction for out-of-plane displacement controlled loading. It is evident in the FE model that boundary condition changes at the pin-plate interface lead to significant response changes and high sensitivity indication of damage. Second, a reliability-based health monitoring framework was presented for pin and hanger assemblies. Two yield limit states for steel are evaluated for plate net-section tension and pin shear failure. The net-section limit state includes bending effects by the sensor placement. The strain gage placed in the net-section region is sensitive to the combined effects of axial and bending loads as well as the effects of section loss. The pin is not directly monitored by strain gages although the shear limit state equation considers pin locking by adding a pin torsion component from measured hanger moments. Long-term measures of input RVs showed that the best describing distribution fit was the GEV distribution. Non-measured input RVs were estimated by previous literature. Reliability was evaluated using MCS methods resulting in reliability index estimations of $\beta = 4.26$ and $\beta = 4.87$ for net-section tension and pin shear limits, respectively. The long-term monitoring framework proposed here allows periodic performance monitoring of pin and hanger assemblies through reliability index performance metric and sets the stage for risk-based management. By utilizing permanently installed sensor data, a long-term condition monitoring program is proposed which does not currently exist for the pin and hanger detail, offering a new type of support which compliments the current state of practice of visual and NDE inspections. Finally, net-section area estimations are made using long-term data statistics. Current estimates of the net-section area are 7.81 in^2 and 5.98 in^2 for forced and free vibration analysis, respectively; the design net-section area is 6.25 in^2. The FE model analyses, reliability analyses and section area estimations are all intended to measure the effects of early onset corrosion of the pin-plate interface.

CHAPTER 7.

CONCLUSIONS

7.1 Summary of Results

The focus of this dissertation is to advance wireless SHM to serve as a decision support tool for owners seeking performance- and risk-based asset management. In order for wireless SHM to meet these demands, several hurdles must be overcome. Wireless sensing is cost-effective but inherently limited to temporary power supplies. Big advances in low-power hardware and power harvesting have been made but operational strategies for low-power consumption have not been fully exploited. In the first part of this thesis, power-efficient usage in wireless sensors is highlighted by embedding compressed sensing data compression and sensor-based interrogation methods in a microcontroller for large data reductions. Specifically, a data compression technique termed compressed sensing and an on-board data processing methodology for fatigue evaluation are embedded into a wireless sensor for large data reductions prior to transmission (and thus large power savings). In the second part of this thesis, a top-down sensor strategy is advocated to target specific damage concerns of bridge owners. This is in contrast to generalized global vibration based approaches which have low sensitivity to local damage. Data-driven data interrogation methods targeting local system responses provide statistical performance and reliability information, compensating for environmental and load influences by using Gaussian Process regression and machine learning methods. The performance and reliability frameworks demonstrated with long-term sensor data are intended to move away from traditional SHM and towards a new approach for risk-based management support.

This dissertation highlights the power savings from the CS and on-board fatigue analysis embedded data reduction techniques. For the CS study, it was observed that at least 20% of Nyquist required sampling was required for acceptable mode shape reconstruction accuracy. Also, it was observed that for a five node network as deployed on the TRB, approximately 8%, 9% and 10% power savings were achieved by 10%, 20% and 30% random sampling, respectively. Greater energy-efficiency can be had for larger sensor networks, projecting higher than 50% for a 100 node network using the TDMA methodology employed on the TRB. The impact on battery life is measured directly from the TRB network. Battery voltages are statistically higher for the CS nodes than the Nyquist uniform sampling nodes.

Embedded fatigue life monitoring is difficult to characterize for power savings as this is dependent on user preference. The potential reductions, however, are immense. Should an owner not require updates on fatigue life, transmissions could potentially cease until fatigue information is specifically requested. Fixed size on-board histogram storage of cycle information will have a maximum storage capacity before some information must be transmitted, but this is highly dependent on the lower threshold setting for cycle extraction as well as pre-rainflow counting signal conditioning (*e.g.,* low-pass filtering). In short, drastic, or nearly all, transmissions can be reduced for the proposed system greatly reducing transmission energy consumption and bandwidth demands which further enables high sensor densities and better coverage of susceptible fatigue damage locations.

In order to move away from SHM and towards risk-based asset management, methods for automated capacity-demand monitoring are required and reliability analyses must be made; Chapter 5 and Chapter 6 highlight these efforts. Chapter 5 utilized long-term monitoring data for the condition performance characterization of a pin and hanger bridge over complete temperature and load profiles experienced on-site to provide performance insight regarding the current bridge capacity. This dissertation highlights automated analyses for modal parameter identification, neutral axis estimation, link-plate bending behavior and thermal deck strain as well as automated performance monitoring using SPC. Link plate bending for in-plane and out-of-plane modes is shown to be sensitive to load magnitude; GPR is used to model this dependency. Neutral axis is not expected to vary with load or temperature for this bridge type, however the long-term data supports slight dependence for certain locations. Normalization of response data to outside influences is performed using long-term data models. Full automation of data acquisition, load identification, regression modeling, normalization and outlier detection on targeted bridge sub-systems of high interest to owners is shown.

Long-term statistical knowledge of live load behaviors enabled reliability studies in Chapter 6. As risk-based management support is the primary goal of this thesis (and bridge owners), a reliability framework to handle sensor data was made. A reliability monitoring program for pin and hanger defects is demonstrated using yield stress limit states for evaluation. Hanger net-section tension and pin shear limit states were evaluated for reliability index using continuous strain gage response to estimate live load parameters. Basic random variables not measured by the sensor system (*e.g.,* dead load, elastic modulus) are taken from literature. Peak strains for in-plane bending and axial measures were collected long-term and used to estimate the behavioral underlying distribution. The GEV distribution showed to be a good fit for peak strain statistics and was used to model axial and bending peak strains. Because limit state functions were comprised of a mix of lognormal and GEV random variables, analytical solutions for reliability index estimation become more complex (than for the case of normal RV's). As such, Monte Carlo simulation (MCS) methods were used to estimate the probability of failure for hanger net-section tension and pin shear. Reliability index estimations were obtained using simulation calculated probability of failure estimates in a standard normal distribution. Reliability index estimations for hanger net-section tension and pin shear were calculated at $\beta = 4.26$ ($P_f = 1.01e$-5) and $\beta = 4.87$ ($P_f = 5.5e$-7), respectively. Long-term data was also used to form a statistical estimate of net-section area in the hanger plate as a means of hanger capacity assessment. Data from forced-response and free-response were evaluated. Free-response data best estimates the net-section area near 6 in.^{2} (the design value is 6.25 in.^{2}). A finite element model was designed to capture the effects of pin-plate fixity to further efforts to integrate sensor data for boundary condition assessment.

7.2 Contributions

In order to enable wireless structural monitoring for long-term management, WSNs have to be more robust to harsh environmental conditions and sustainable on limited power supply (*e.g.*, solar power). In addition, since SHM has not proven to be useful for bridge management, an alternative approach to SM and decision support needs to be made. Vibration based damage detection is commonly used and has shown challenges, especially due to influence from environmental and loading conditions as well as local damage inference from global acceleration measurements. Channel cost further limits global sensor systems by limiting spatial density. Enabling sustainable long-term wireless sensing opens the door to higher channel counts and higher density spatial sensing. Limitations in damage detection have been mentioned; however, attempts towards damage mitigation rather than damage detection are of increasing interest as the U.S. moves away from reactive bridge management and towards proactive, performance-based management.

The main contributions of this dissertation are to develop power-efficient usage strategies for wireless monitoring systems on remote highway bridges and to use data-driven interrogation methods for structural performance assessment in an effort to utilize the high channel counts that wireless offers and to make structural monitoring systems adoptable for U.S. bridge management. These contributions are in contrast with cable-based systems limited by cost and obtrusiveness, as well as global vibration based structural monitoring which has proven ineffective for bridge management support. In Chapter 2, the TRB wireless sensor network is described to address specific damage behavior and concerns of MDOT. The top-down sensor strategy deployed is novel for long-term structural monitoring, using a combinations of acceleration, strain and temperature measurements to detect behavior associated with incipient damage in the most common deterioration processes for pin and hanger steel girder composite bridges. The long-term performance data from the TRB is a contribution alone as there are very few data sets on in-service bridges, especially short-span highway bridges. The USDOT has implemented long-term monitoring programs for this purpose alone (*e.g.*, LTBP Program). The TRB system has also demonstrated sustainable operations over a four-year time frame. Challenges of winter weather were addressed by the end of the study, verifying the potential for permanent WSNs in remote northern climates for SM.

The compressed sensing work in Chapter 3 is novel by its implementation for field deployment. The TRB demonstration was the first example of CS in a long-term WSN deployment for operational structural monitoring. Most of the current literature quantify the accuracy of signal reconstruction only. The work in Chapter 3 shows quantified energy savings and the impact of CS on battery levels and communication reliability for a long-term deployed WSN. The TRB implementation is among the first structural monitoring wireless sensors with true compressive sampling (*i.e.,* no digital processing is required to produce compressed measurements) embedded and field deployed with no requirement for custom sampling hardware or digitally computed linear combinations on full length signals. A very repeatable example is demonstrated utilizing commercial off-the-shelf (COTS) hardware and embedded linear congruential pseudo-random sampling. The CS strategy advocated does not require custom sampling hardware, significant on-board storage and nor the execution of potentially large matrix operations by the wireless sensor microcontroller. Chapter 4 demonstrates a second example of power-efficient usage for WSN and at the same time decentralizes the fatigue life monitoring process. Embedding fatigue life monitoring on wireless sensors enables high channel counts required to monitor many fatigue "hot-spots" that exist for large structures (*e.g.,* ship hulls). The contribution of this work lies in embedded rainflow counting and power spectral density calculations on-board a wireless sensor and on-board damage according to Palmgren-Miner rules.

Contributions in terms of data-driven interrogation methods for structural monitoring are described in Chapter 5 and Chapter 6. This work characterizes pin and hanger bridge response across a complete temperature and load envelope. Full temperature characterization requires at least one year of continuous sensor data, making this four-year implementation valuable by its ability to fully model physical response sensitivity to temperature effects. In addition, the work here establishes a statistical process control (SPC) framework for automated performance monitoring. In contrast to current literature SPC techniques which utilize single sensor data directly or damage sensitive features on vibration signals, the work presented here uniquely casts information obtained from sensor systems targeting specific concerns of MDOT into a SPC framework, such as neutral axis position, thermal expansion rate and link plate bending strain which also account for influences of load and temperature through long-term regression modeling. This approach to structural monitoring is at the heart of the top-down sensor strategy employed and also at the heart of boundary condition assessments for capacity-demand information and subsequent reliability estimations.

Chapter 6 is a novel long-term structural monitoring approach to reliability monitoring that sets the stage for wireless sensor monitoring as a valuable tool for risk-based management. A reliability and capacity monitoring application for pin and hanger assemblies is made due to their high susceptibility to corrosion damage and locking. Also, since VI and NDE methods used for pin and hanger inspection are focused on damage detection only, the TRB sensing strategy offers enormous potential as a preventative monitoring tool by its ability to detect early indication of locking and corrosion. The proposed work uniquely utilizes long-term hanger response data to evaluate shear and tension limit states in pin and hangers, respectively, for reliability-index based performance monitoring. The work here reduces the amount of uncertainty in the reliability formulation by using measured data. The methods proposed here promote damage prevention by targeting damage inducing conditions (*e.g.*, changes in link plate bending, changes in net-section strain response) which are in contrast to current inspection procedures. The work shown in Chapter 6 for pin and hanger assemblies is generally applicable to targeted deterioration and is intended for other degradation systems being measured on the TRB (*e.g.*, neutral axis) and to be extended to many locations to approach system level reliability measures.

7.3 Future Work

The most immediate goals for future work lie in extending the reliability framework discussed in Chapter 6. Reliability measures for composite action, beam end contact and link plate bending can be formulated and evaluated with the current sensor instrumentation. System level reliability measures are a natural extension as well. The low-cost of wireless sensing enables high density sensing making instrumentation of each and every hanger plate possible. Reliability estimations for each assembly can be combined into a system reliability framework and paired with failure consequences to provide owners with meaningful decision support. The pin and hanger study can be extended further than reported in Chapter 6. The simplicity of the pin and hanger assembly makes for an interesting direct evaluation of damage by considering the effect of boundary conditions at the pin-plate interface. Future work includes fusing pin and plate accelerations with plate strains as well as utilizing the FE model developed in Chapter 6 to infer levels of corrosion in the pin-plate boundary. The reliability index monitoring framework is in line with new bridge management motivations for performance- and risk-based asset management and should be extended beyond pin and hanger concerns.

In Chapter 3 compressed sensing methods were applied to acceleration signals for compression. The current scheme utilizes the Fourier basis for sparsity and the result is adequate compressibility. The compressibility of bridge vibrations may be better with a tailored approach built on learning of long-term data. For example, creation of custom atoms for signal decomposition built on typical responses from typical vehicle classes may enable an empirically derived dictionary demonstrating sparser transforms and thus greater data compression.

A longer term future research goal involves autonomous and re-configurable sensor networks optimized for resource efficiency to make wireless systems even more sustainable for permanent deployments. Wireless sensors are typically deployed with a fixed data acquisition task, a fixed power supply, a fixed sensing schedule, etc., based on the initial needs of the sensor system. Needs can change in the short-term and long-term, prompting a need for re-configuration. For example, initial data collections may suggest that certain sensors are under- or over-utilized due to inaccuracies in assumed boundary conditions, connections, load demands, solar power, etc. In this case, sensor usage can be increased or decreased and resources can be re-allocated through the remainder of the sensor network based on optimization strategies. Optimizations for power usage, communication bandwidth, information value, etc., can be made periodically and used to re-configuring the sensor network autonomously to provide the best value to the structure owner given the current and projected resources for the WSN. The TRB network would be an ideal testbed for this kind of future work.

REFERENCES

[1] Federal Highway Administration (2014). *National Bridge Inventory* (NBI). Retrieved from: http://www.fhwa.dot.gov/bridge/nbi.cfm

[2] American Society of Civil Engineers (2013). *2013 Report Card For America's Infrastructure*.

[3] Transportation for America (2013). *The Fix We're In For: The State of Our Nation's Bridges 2013*. Retrieved from: http://t4america.org/docs/bridgereport2013/2013BridgeReport.pdf

[4] American Association of State Highway and Transportation Officials (2007). *Transportation - Invest in our Future: Future Needs of the U.S. Surface Transportation System*. Retrieved from: ftp://ftp.mdt.mt.gov/research/library/TIF1-1-FUTURE_NEEDS-AASHTO.PDF

[5] Federal Highway Administration (2004). *2004 Status of the Nation's Highways, Bridges, and Transit: Conditions and Performance*. Retrieved from: https://www.fhwa.dot.gov/policy/2004cpr/pdfs/cp2006.pdf

[6] K. Wright (2012). *Steel Bridge Design Handbook: Selecting the Right Bridge Type*. [Report No. FHWA-IF-12-052]. Retrieved from: https://www.fhwa.dot.gov/bridge/steel/pubs/if12052/volume05.pdf

[7] D. A. Juntunen (1998). *Study of Michigan's Link Plate and Pin Assemblies*. [Report No. R-1358]. Retrieved from: https://www.michigan.gov/documents/mdot/MDOT_RC-1358_412398_7.pdf

[8] J. M. South, C. Hahin, and R. O. Telford (1992). *Analysis, inspection, and repair methods for pin connections on Illinois bridges*. [Report No. FHWA/IL/PR-01]. Retrieved from: http://ntl.bts.gov/lib/9000/9300/9320/airm.pdf

[9] National Transportation Safety Board (1984). *Highway Accident Report: Collapse of a Suspended Span of Interstate Route 95 Highway Bridge Over the Mianus River*. [Report No. NTSB/HAR-84-03]. Retrieved from: http://rebar.ecn.purdue.edu/Fatigue/Fisher_Files/128-Mianus_River_Bridge/Additional_Information/Publications//Part%201%20NTSB%20Highway%20Accident%20Report.pdf

[10] J. W. Fisher and U. Yuceoglu (1981). *A Survey of Localized Cracking in Steel Bridges*. [Fritz Lab Report No. 448-2(81)]. Retrieved from: http://digital.lib.lehigh.edu/fritz/pdf/448_2_81_.pdf

[11] C. LeRose (2001). *The collapse of the silver bridge*. Retrieved from: http://www.wvculture.org/history/wvhs1504.html

[12] D. Rolander, B. Phares, B. Graybeal, M. Moore, and G. Washer (2001). Highway bridge inspection: State-of-the-practice survey. *Transportation Research Record: Journal of the Transportation Research Board*, vol. 1749, pp. 73-81.

[13] Federal Highway Administration (2001). "*Reliability of visual inspection for highway bridges*. [Technical Summary]. Retrieved from: https://www.fhwa.dot.gov/publications/research/nde/pdfs/01105.pdf

[14] T. W. Ryan, R. A. Hartle, J. E. Mann, and L. J. Danovich (2006). *Bridge inspector's reference manual (BIRM)*. [Report No. FHWA NHI 12-049]. Retrieved from: http://www.fhwa.dot.gov/bridge/nbis/pubs/nhi12049.pdf

[15] M. Moore, B. Phares, B. Graybeal, D. Rolander, and G. Washer (2001). *Reliability of visual inspection for highway bridges, volume I: Final report*. [Report No. FHWA-RD-01-020]. Retrieved from: https://www.fhwa.dot.gov/publications/research/nde/pdfs/01020a.pdf

[16] P. J. Vanderzee (2009). Sensor Technology for Assessing Bridge Performance. *Presented at the Fifth US-Taiwan Bridge Engineering Workshop*, Taipei, Taiwan.

[17] G. A. Washer (2000). Developing NDE technologies for infrastructure assessment. *Public Roads*. 63(4), 44-50.

[18] D. S. Forsyth, H. T. Yolken, and G. A. Matzkanin (2006). A Brief Introduction to Nondestructive Testing. *AMMTIAC Quarterly 1(2)*. Retrieved from: http://citeseerx.ist.psu.edu/viewdoc/download?doi=10.1.1.383.7049&rep=rep1&type=pdf

[19] A. Nair and C. S. Cai (2010). Acoustic emission monitoring of bridges: Review and case studies. *Engineering Structures,* 32(6), pp. 1704-1714.

[20] M. L. Wang, J. P. Lynch, and H. Sohn (2014). *Sensor Technologies for Civil Infrastructures* vol. 1, Cambridge:Woodhead Publishing.

[21] C. R. Farrar and K. Worden (2007). An introduction to structural health monitoring. *Philosophical Transactions of the Royal Society A: Mathematical, Physical and Engineering Sciences,* 365 (1851), pp. 303-315.

[22] C. R. Farrar and K. Worden (2012). *Structural health monitoring: a machine learning perspective.* Chichester: John Wiley & Sons.

[23] D. Adams (2007). *Health monitoring of structural materials and components: methods with applications.* Hoboken, NJ:John Wiley & Sons.

[24] S. D. Glaser, H. Li, M. L. Wang, J. Ou, and J. Lynch (2007). Sensor technology innovation for the advancement of structural health monitoring: a strategic program of US-China research for the next decade," *Smart Structures and Systems,* 3(2), pp. 221-244.

[25] M. Celebi (2002). *Seismic instrumentation of buildings (with emphasis on federal buildings)*. [Report No. 00-157]. Retrieved from:

http://pubs.usgs.gov/of/2000/0157/pdf/of00-157.pdf

[26] C. R. Farrar (2001). Historical overview of structural health monitoring. [presented at the Lecture Notes on Structural Health Monitoring using Statistical Pattern Recognition], Los Alamos, NM.

[27] B. Peeters, J. Maeck, and G. De Roeck (2001). Vibration-based damage detection in civil engineering: excitation sources and temperature effects. *Smart materials and Structures*, 10, pp. 518-527.

[28] M. Friswell and J. E. Mottershead (1995). *Finite element model updating in structural dynamics*. Dordrecht: Springer.

[29] H. Sohn, C. R. Farrar, N. F. Hunter, and K. Worden (2001). Structural Health Monitoring Using Statistical Pattern Recognition Techniques. *Journal of Dynamic Systems, Measurement, and Control*, 123(4), pp. 706-711.

[30] S. W. Doebling, C. R. Farrar, and M. B. Prime (1998). A summary review of vibration-based damage identification methods. *Shock and Vibration Digest*, 30(2), pp. 91-105.

[31] A. Heng, S. Zhang, A. C. C. Tan, and J. Mathew (2009). Rotating machinery prognostics: State of the art, challenges and opportunities. *Mechanical Systems and Signal Processing*, 23(3), pp. 724-739.

[32] O. F. Eker, F. Camci, and I. K. Jennions (2012). Major challenges in prognostics: Study on benchmarking prognostics datasets. *European Conference of Prognostics and Health Management Society*, pp. 1-8.

[33] S. W. Doebling, C. R. Farrar, M. B. Prime, and D. W. Shevitz (1996). Damage Identification and Health Monitoring of Structural and Mechanical Systems from Changes in their Vibration Characteristics: A Literature Review. [Report No. LA-13070-MS]. Retrieved from: https://institute.lanl.gov/ei/shm/pubs/lit_review.pdf.

[34] S. Alampalli (1998). Influence of in-service environment on modal parameters. *Proceedings of the 16th International Modal Analysis Conference*, pp. 111-116.

[35] M. L. Fugate, H. Sohn, and C. R. Farrar (2001). Vibration-based damage detection using statistical process control. *Mechanical Systems and Signal Processing.* 15(4), pp. 707-721.

[36] H. Sohn, J. A. Czarnecki, and C. R. Farrar (2000). Structural health monitoring using statistical process control. *Journal of Structural Engineering*, 126(11), pp. 1356-1363.

[37] Y. Zhang, S. M. O'Connor, G. van der Linden, A. Prakash, and J. P. Lynch (2015 in review). SenStore: a Scalable Cyberinfrastructure Platform for Implementation of Data-to-Decision Frameworks for Infrastructure Health Management. *Journal of Computing in Civil Engineering*.

[38] M. Collette and J. P. Lynch (2013). Lifecycle Support for Naval Ships based on Structural Health Monitoring: Data to Decisions Strategies," *ASNE Annual Meeting*, p. 13.

[39] E. G. Straser, A. S. Kiremidjian, T. H. Meng, and L. Redlefsen (1998). Modular, wireless network platform for monitoring structures. *Proceeding of 16th Interational Modal Analysis Conference*, pp. 450-456.

[40] D. Zhu, J. Guo, C. Cho, Y. Wang, and K.-M. Lee (2012). Wireless mobile sensor network for the system identification of a space frame bridge. *IEEE/ASME Transactions on Mechatronics,* 17(3), pp. 499-507.

[41] I. F. Akyildiz, W. Su, Y. Sankarasubramaniam, and E. Cayirci (2002). Wireless sensor networks: a survey. *Computer networks*, 38, pp. 393-422.

[42] M. C. W. Kintner-Meyer, J. R. Skorpik, and L. D. Reid (2004). Report On Cost-Effectiveness And Energy Savings From Application Of Low-Cost Wireless Sensing. [Report No. PNNL-15018]. Retrieved from: http://www.pnl.gov/main/publications/external/technical_reports/PNNL-15018.pdf

[43] N. A. Tanner, J. R. Wait, C. R. Farrar, and H. Sohn (2003). Structural health monitoring using modular wireless sensors. *Journal of Intelligent Material Systems and Structures*, 14(1), pp. 43-56.

[44] J. P. Lynch, A. Sundararajan, K. H. Law, A. S. Kiremidjian, and E. Carryer (2004). Embedding damage detection algorithms in a wireless sensing unit for attainment of operational power efficiency. *Smart Materials and Structures, IOP,*13, pp. 800-810.

[45] S. N. Pakzad, G. L. Fenves, S. Kim, and D. E. Culler (2008). Design and implementation of scalable wireless sensor network for structural monitoring. *Journal of Infrastructure Systems,* 14, pp. 89-101.

[46] J. P. Lynch, Y. Wang, K. Loh, J. H. Yi, and C. B. Yun (2006). Performance monitoring of the Geumdang Bridge using a dense network of high-resolution wireless sensors. *Smart Materials and Structures,* 15, pp. 1561-1575.

[47] J. L. Hill and D. E. Culler (2002). Mica: A wireless platform for deeply embedded networks. *Micro, IEEE,* 22, pp. 12-24.

[48] L. Nachman, J. Huang, J. Shahabdeen, R. Adler, and R. Kling (2008). Imote2: Serious computation at the edge. *Wireless Communications and Mobile Computing Conference*, pp. 1118-1123.

[49] J. Polastre, R. Szewczyk, and D. Culler (2005). Telos: enabling ultra-low power wireless research. *Information Processing in Sensor Networks*, pp. 364-369.

[50] P. Levis, S. Madden, J. Polastre, R. Szewczyk, K. Whitehouse, A. Woo, *et al.* (2005). TinyOS: An Operating System for Sensor Networks. in W. Weber, J. Rabaey, and E. Aarts (Eds.) *Ambient Intelligence*. Berlin: Springer.

[51] R. A. Swartz, D. Jung, J. P. Lynch, Y. Wang, D. Shi, and M. P. Flynn (2005). Design of a wireless sensor for scalable distributed in-network computation in a structural health monitoring system. *Presented at the 5th International Workshop on Structural Health Monitoring,* pp. 1570-1577

[52] B. F. Spencer, M. E. Ruiz-Sandoval, and N. Kurata (2004). Smart sensing technology: opportunities and challenges. *Journal of Structural Control and Health Monitoring,* 11, pp. 349-368.

[53] S. Jang, H. Jo, S. Cho, K. Mechitov, J. A. Rice, S. H. Sim, *et al.* (2010). Structural health monitoring of a cable-stayed bridge using smart sensor technology: deployment and evaluation. *Smart Structures and Systems,* 6, pp. 439-459.

[54] M. Kurata, J. Kim, J. Lynch, G. van der Linden, H. Sedarat, E. Thometz, *et al.* (2012). Internet-Enabled Wireless Structural Monitoring Systems: Development and Permanent Deployment at the New Carquinez Suspension Bridge. *Journal of structural engineering,* 139, pp. 1688-1702.

[55] G. Feltrin, J. Meyer, R. Bischoff, and M. Motavalli (2010). Long-term monitoring of cable stays with a wireless sensor network. *Structure and Infrastructure Engineering,* 6, pp. 535-548.

[56] G. C. Lee and E. Sternberg (2015). *Bridges: Their Engineering and Planning*. New York: SUNY Press.

[57] S. Alampalli and G. Fu (1994). Instrumentation for remote and continuous monitoring of structure conditions. *Transportation research record,* 1432, pp. 59-67.

[58] E. G. Straser (1998). *A modular, wireless damage monitoring system for structures*. [Ph. D. dissertation], Stanford University.

[59] J. P. Lynch (2002). Decentralization of wireless monitoring and control techniques for smart civil structures. [Ph.D. dissertation], Stanford University.

[60] J. P. Lynch, K. H. Law, A. S. Kiremidjian, E. Carryer, C. R. Farrar, H. Sohn, *et al.* (2004). Design and performance validation of a wireless sensing unit for structural monitoring applications. *Structural engineering & mechanics,* 17, pp. 393-408.

[61] S. Kim, S. Pakzad, D. Culler, J. Demmel, G. Fenves, S. Glaser, *et al.* (2007). Health monitoring of civil infrastructures using wireless sensor networks. *Information Processing in Sensor Networks,* pp. 254-263.

[62] M. J. Whelan and K. D. Janoyan (2009). Design of a robust, high-rate wireless sensor network for static and dynamic structural monitoring. *Journal of intelligent material systems and structures,* 20, pp. 849-863.

[63] M. V. Gangone, M. J. Whelan, and K. D. Janoyan (2011). Wireless monitoring of a multispan bridge superstructure for diagnostic load testing and system identification. *Computer‐Aided Civil and Infrastructure Engineering*, 26, pp. 560-579.

[64] J.-H. Weng, C.-H. Loh, J. P. Lynch, K.-C. Lu, P.-Y. Lin, and Y. Wang (2008). Output-only modal identification of a cable-stayed bridge using wireless monitoring systems. *Engineering Structures,* 30, pp. 1820-1830.

[65] H. Jo. *Jindo Bridge - Smart Structure Systems Laboratory*. [Website] http://smartstructure.weebly.com/jindo-bridge.html

[66] H. Jo, S.-H. Sim, K. A. Mechitov, R. Kim, J. Li, P. Moinzadeh, *et al.* (2011). Hybrid wireless smart sensor network for full-scale structural health monitoring of a cable-stayed bridge. *Proc. SPIE 7981*, pp. 798105-798105.

[67] T. V. Galchev, J. McCullagh, R. L. Peterson, and K. Najafi (2011). Harvesting traffic-induced vibrations for structural health monitoring of bridges. *Journal of Micromechanics and Microengineering,* 21(10), p. 104005.

[68] S. J. Roundy (2003). Energy scavenging for wireless sensor nodes with a focus on vibration to electricity conversion. [Ph.D. dissertation] University of California, Berkely.

[69] T. Galchev, J. McCullagh, R. L. Peterson, K. Najafi, and A. Mortazawi (2011). Energy harvesting of radio frequency and vibration energy to enable wireless sensor monitoring of civil infrastructure. *Proc. SPIE 7983*, pp. 798314-798314.

[70] Y. Wang, J. P. Lynch, and K. H. Law (2007). A wireless structural health monitoring system with multithreaded sensing devices: design and validation. *Structure and Infrastructure Engineering*, 3, pp. 103-120.

[71] V. A. Kottapalli, A. S. Kiremidjian, J. P. Lynch, E. Carryer, T. W. Kenny, K. H. Law, *et al.* (2003). Two-tiered wireless sensor network architecture for structural health monitoring. *Proc. SPIE 5057*, pp. 8–19.

[72] J. P. Lynch and K. J. Loh (2006). A summary review of wireless sensors and sensor networks for structural health monitoring. *The Shock and vibration digest*, 38, pp. 91-128.

[73] N. A. Tanner, C. R. Farrar, and H. Sohn (2002). Structural health monitoring using wireless sensing system with embedded processing. *Proc. SPIE 4704*, pp. 215-224.

[74] A. T. Zimmerman, M. Shiraishi, R. A. Swartz, and J. P. Lynch (2008). Automated modal parameter estimation by parallel processing within wireless monitoring systems. *ASCE Journal of Infrastructure Systems,* 14, pp. 102-113.

[75] J. P. Lynch, A. Sundararajan, K. H. Law, A. S. Kiremidjian, and E. Carryer (2004). Embedding damage detection algorithms in a wireless sensing unit for operational power efficiency. *Smart Materials and Structures*, 13, pp. 800-810.

[76] J.-W. Park, S.-H. Sim, and H.-J. Jung (2013). Wireless sensor network for decentralized damage detection of building structures. *Smart Structures and Systems,* 12, pp. 399-414.

[77] G. Hackmann, F. Sun, N. Castaneda, C. Lu, and S. Dyke (2008). A holistic approach to decentralized structural damage localization using wireless sensor networks. *Real-Time Systems Symposium*, pp. 35-46.

[78] C. A. Peckens, J. P. Lynch, and J.-S. Pei (2011). Distributed neural computations for embedded sensor networks. *Proc. SPIE 7981*, pp. 79811U-79811U.

[79] J. P. Lynch, A. Sundararajan, K. H. Law, A. S. Kiremidjian, and E. Carryer (2003). Power-efficient data management for a wireless structural monitoring system. *Proceedings of the 4th International Workshop on Structural Health Monitoring,* pp. 1177-1184.

[80] J. Caffrey, R. Govindan, E. Johnson, B. Krishnamachari, S. Masri, G. Sukhatme, *et al.* (2004). Networked sensing for structural health monitoring. *Proceedings of the 4th International Workshop on Structural Control*, pp. 57-66.

[81] E. J. Candès, J. Romberg, and T. Tao (2006). Robust uncertainty principles: Exact signal reconstruction from highly incomplete frequency information. *IEEE Transactions on Information Theory,*52, pp. 489-509.

[82] D. L. Donoho (2006). Compressed sensing. *IEEE Transactions on Information Theory,* 52, pp. 1289-1306.

[83] Y. Tsaig and D. L. Donoho (2006). Extensions of compressed sensing. *Signal Processing,* 86, pp. 549-571.

[84] D. Mascarenas, A. Cattaneo, J. Theiler, and C. Farrar (2013). Compressed Sensing Techniques for Detecting Damage in Structures. *Structural Health Monitoring,* 12, pp. 325-388.

[85] Y. Bao, J. L. Beck, and H. Li (2010). Compressive sampling for accelerometer signals in structural health monitoring. *Structural Health Monitoring,* 10, pp. 235-246.

[86] Y. Bao, H. Li, X. Sun, Y. Yu, and J. Ou (2013). Compressive sampling–based data loss recovery for wireless sensor networks used in civil structural health monitoring. *Structural Health Monitoring,* 12, pp. 78-95.

[87] Federal Highway Administration (2011). *Bridge Preservation Guide.* [Report No. FHWA-HIF-11042]. Retrieved from:
http://www.fhwa.dot.gov/bridge/preservation/guide/guide.pdf

[88] Federal Highway Administration. (2012). *Moving Ahead for Progress in the 21*st *Century Act (MAP-21): A Summary of Highway Provisions*. Retrieved from:
http://www.fhwa.dot.gov/map21/summaryinfo.cfm

[89] P. Thompson and R. Shepard (1994). The Pontis Bridge Management System. *Structural Engineering International,* 8, pp. 303-308.

[90] H. Hawk and E. P. Small (1998). The BRIDGIT bridge management system. *Structural engineering international,* 8, pp. 309-314.

[91] D. M. Frangopol, J. S. Kong, and E. S. Gharaibeh (2001). Reliability-based life-cycle management of highway bridges. *Journal of computing in civil engineering,* 15, pp. 27-34.

[92] P. C. Das (2010). Bridge management objectives and methodologies. *Bridge Management: Proceedings of the Third International Conference*, pp. 1-7.

[93] P. Thoft-Christensen and M. J. Baker (1982). *Structural reliability theory and its applications*. New York: Springer.

[94] R. E. Melchers (1999). *Structural Reliability: Analysis and Prediction* vol. 2. West Sussex, England: John Wiley & Sons.

[95] H. O. Madsen, S. Krenk, and N. C. Lind (2006). *Methods of structural safety* Englewood, NJ: Prentice-Hall.

[96] A. S. Nowak and J. Zhou (1990). System reliability models for bridges. *Structural Safety,* 7, pp. 247-254.

[97] S. W. Tabsh and A. S. Nowak (1991). Reliability of highway girder bridges. *Journal of Structural Engineering,* 117, pp. 2372-2388.

[98] A. C. Estes and D. M. Frangopol (1999). Repair optimization of highway bridges using system reliability approach. *Journal of Structural Engineering,* 125, pp. 766-775.

[99] J. S. Kong and D. M. Frangopol (2003). Life-cycle reliability-based maintenance cost optimization of deteriorating structures with emphasis on bridges. *Journal of Structural Engineering,* 129, pp. 818-828.

[100] M. Brown, J. Gomez, M. Hammer, and J. Hooks (2014). *Long-Term Bridge Performance Program High Priority Issues*. [Report No. FHWA-HRT-14-043]. Retrievd from: https://www.fhwa.dot.gov/publications/research/infrastructure/structures/ltbp/14043/14043.pdf

[101] M. Barbato and J. P. Conte (2010). Structural reliability applications of nonstationary spectral characteristics. *Journal of Engineering Mechanics,* 137, pp. 371-382.

[102] M. Gobbato, J. P. Conte, J. B. Kosmatka, and C. R. Farrar (2012). A reliability-based framework for fatigue damage prognosis of composite aircraft structures. *Probabilistic Engineering Mechanics,* 29, pp. 176-188.

[103] W.-H. Kang, J. Song, and P. Gardoni (2008). Matrix-based system reliability method and applications to bridge networks. *Reliability Engineering & System Safety,* 93, pp. 1584-1593.

[104] M. M. Ettouney, S. Alampalli, and A. K. Agrawal (2005). Theory of multihazards for bridge structures. *Bridge Structures,* 1, pp. 281-291.

[105] M. M. Ettouney and S. Alampalli (2011). *Infrastructure health in civil engineering: Theory and components* vol. 1, Boca Raton: CRC Press.

[106] A. Cardini and J. T. DeWolf (2009). Long term structural health monitoring of a multi girder steel composite bridge using strain data. *Structural Health Monitoring,* 8, pp. 47-58.

[107] P. O. Jansson (2008). *Analysis of Stress Distribution in Link Plates Used for Suspending Bridge Beams.* [Report No. R-1517]. Retrieved from: https://www.michigan.gov/documents/mdot/MDOT_Research_Report_R1517_248445_7.pdf

[108] H. Sohn, C. R. Farrar, F. M. Hemez, D. D. Shunk, D. W. Stinemates, B. R. Nadler, *et al.*, (2003). A Review of Structural Health Monitoring Literature 1996-2001. [Report No. LA-13976-MS]. Retrieved from: https://institute.lanl.gov/ei/shm/pubs/LA_13976_MSa.pdf

[109] G. W. van der Linden, A. Emami-Naeini, Y. Zhang, and J. P. Lynch (2013). Cyber-infrastructure design and implementation for structural health monitoring. *Proc. SPIE 8694*, pp. 869419-869419-8.

[110] Y. Zhang, S. M. O'Connor, G. van der Linden, A. Prakash, and J. P. Lynch (2015 in review). SenStore: a Scalable Cyberinfrastructure Platform for Implementation of Data-to-Decision Frameworks for Infrastructure Health Management. *Journal of Computing in Civil Engineering*.

[111] J. Kim, A. Swartz, J. P. Lynch, J.-J. Lee, and C.-G. Lee (2010). Rapid-to-deploy reconfigurable wireless structural monitoring systems using extended-range wireless sensors. *Smart Structures and Systems,* 6, pp. 505-524.

[112] Y. Zhang, M. Kurata, J. P. Lynch, G. van der Linden, H. Sederat, and A. Prakash (2012). Distributed cyberinfrastructure tools for automated data processing of structural monitoring data. *Proc. SPIE 8347*, pp. 83471Y-8.

[113] M. C. Brown, J. Gomez, T. Cousins, and F. Barton (2003). Composite Action in a Steel Girder Span with Precast Deck Panels: The I-81 Bridge Over the New River in Radford, Virginia. [Report No. VTRC 04-R4]. Retrieved from: http://www.virginiadot.org/vtrc/main/online_reports/pdf/04-r4.pdf

[114] A. A. Mosavi, H. Sedarat, S. M. OConnor, A. EmamiNaeini, V. Jacob, A. Krimotat, *et al.* (2012). Finite Element model updating of a skewed highway bridge using a multivariable sensitivity based optimization approach. *Proc. of SPIE 8347*, pp. 834727-12.

[115] P. Andersen, R. Brincker, B. Peeters, G. De Roeck, L. Hermans, and C. Krämer (1999). Comparison of system identification methods using ambient bridge test data. *Proceedings of the 17th International Modal Analysis Conference (IMAC)*, pp. 1035-1041.

[116] B. Peeters and G. De Roeck (1999). Reference-based stochastic subspace identification for output-only modal analysis. *Mechanical systems and signal processing,* 13, pp. 855-878.

[117] P. Van Overschee and B. De Moor (1996). *Subspace identification for linear systems: Theory, implementation*. Dordrecht:Kluwer.

[118] P. Andersen, R. Brincker, M. Goursat, and L. Mevel (2007). Automated modal parameter estimation of civil engineering structures. *Presented at the International Conference of Experimental Vibration Analysis for Civil Engineering Structures*, pp. 1-10.

[119] F. Magalhaes, A. Cunha, and E. Caetano (2009). Online automatic identification of the modal parameters of a long span arch bridge. *Mechanical Systems and Signal Processing,* 23, pp. 316-329.

[120] B. Peeters and G. De Roeck (2001). One-year monitoring of the Z 24-Bridge: environmental effects versus damage events. *Earthquake engineering & structural dynamics,* 30, pp. 149-171.

[121] Y. Zhang, M. Häckell, J. P. Lynch, and R. Rolfes (2014). Automated Modal Parameter Extraction and Statistical Analysis of the New Carquinez Bridge Response to Ambient Excitations," in H.S. Atamturktur, B. Moaveni, C. Papadimitriou and T. Schoenherr (Eds.) *Model Validation and Uncertainty Quantification, Volume 3.* New York: Springer.

[122] H. Sohn, M. Dzwonczyk, E. G. Straser, A. S. Kiremidjian, K. H. Law, and T. Meng (1999). An experimental study of temperature effect on modal parameters of the Alamosa Canyon Bridge. *Earthquake engineering & structural dynamics,* 28, pp. 879-897.

[123] H. Sohn (2007). Effects of environmental and operational variability on structural health monitoring. *Philosophical Transactions of the Royal Society A: Mathematical, Physical and Engineering Sciences,* 365, pp. 539-560.

[124] C. R. Farrar, S. W. Doebling, P. J. Cornwell, and E. G. Straser (1997). Variability of modal parameters measured on the Alamosa Canyon Bridge. *Proceedings of the 15th International Modal Analysis Conference (IMAC),* pp. 257-263.

[125] J. Romberg and M. B. Wakin (2007). Compressed Sensing: A tutorial. *Presented at the IEEE Statistical Signal Processing Workshop,* Madison, Wisconsin.

[126] M. A. Davenport, J. N. Laska, P. T. Boufounos, and R. G. Baraniuk (2009). A simple proof that random matrices are democratic. *arXiv preprint arXiv:0911.0736.*

[127] S. M. O'Connor, J. P. Lynch, and A. C. Gilbert (2011). Compressive sensing approach for structural health monitoring of ship hulls. *Proceedings of the 9th International Workshop on Structural Health Monitoring,* pp. 1675-1682.

[128] M. A. Davenport, M. F. Duarte, M. B. Wakin, J. N. Laska, D. Takhar, K. F. Kelly, *et al.* (2007). The smashed filter for compressive classification and target recognition. *Proc. SPIE 6498*, pp. 64980H-64980H-12.

[129] J. Cortial, C. Farhat, L. Guibas, and M. Rajashekhar (2007). Compressed sensing and time-parallel reduced-order modeling for structural health monitoring using a DDDAS. In Y.Shi, G.D. van Albada, J. Dongarra and P.M.A. Sloot (Eds.), *Computational Science–ICCS 2007*, Berling: Springer.

[130] M. Haile and A. Ghoshal (2012). Application of compressed sensing in full-field structural health monitoring. *Proc. SPIE 8346*, pp. 834618-834618-6.

[131] J. Haupt, W. U. Bajwa, M. Rabbat, and R. Nowak (2008). Compressed sensing for networked data. *IEEE Signal Processing Magazine*, 25, pp. 92-101.

[132] R. Masiero, G. Quer, M. Rossi, and M. Zorzi (2009). A Bayesian analysis of compressive sensing data recovery in wireless sensor networks. *2009 International Conference on Ultra Modern Telecommunications & Workshops*, pp. 1-6.

[133] W. Bajwa, J. Haupt, A. Sayeed, and R. Nowak (2006). Compressive wireless sensing. *Proceedings of the 5th international conference on Information processing in sensor networks*, pp. 134-142.

[134] Y. Bao, Z. Zou, and H. Li (2014). Compressive sensing based wireless sensor for structural health monitoring. *Proc. SPIE 9061,* pp. 90611W-90611W.

[135] S. M. O'Connor, J. P. Lynch, and A. C. Gilbert (2013). Implementation of a compressive sampling scheme for wireless sensors to achieve energy efficiency in a structural health monitoring system. *Proc. SPIE 8694,* pp. 86941L-86941L-11.

[136] R. Brincker, L. Zhang, and P. Andersen (2001). Modal identification of output-only systems using frequency domain decomposition. *Smart Materials and Structures,* 10, pp. 441-445.

[137] S. M. O'Connor, J. P. Lynch, M. Ettouney, G. van der Linden, and S. Alampalli (2012). Cyber-enabled Decision Making System for Bridge Manangement using Wireless Monitoring Systems: Telegraph Road Bridge Demonstration Project. *Presented at the NDE-NDT for Highways and Bridges: Structural Materials Technology (SMT)*, New York, NY.

[138] D. Needell and J. A. Tropp (2009). CoSaMP: Iterative signal recovery from incomplete and inaccurate samples. *Applied and Computational Harmonic Analysis,* 26, pp. 301-321.

[139] R. J. Allemang and D. L. Brown (1982). A correlation coefficient for modal vector analysis. *Proceedings of the International Modal Analysis Conference & Exhibit*, pp. 110-116.

[140] E. J. Candès and T. Tao (2006). Near-optimal signal recovery from random projections: Universal encoding strategies? *IEEE Transactions on Information Theory,* 52, pp. 5406-5425.

[141] E. J. Candès (2008). The restricted isometry property and its implications for compressed sensing. *Comptes Rendus Mathematique,* 346, pp. 589-592.

[142] R. G. Baraniuk (2007). Compressive sensing. *IEEE Signal Processing Magazine,* 24, p. 118.

[143] E. J. Candès and T. Tao (2005). Decoding by linear programming. *IEEE Transactions on Information Theory*, 51, pp. 4203-4215.

[144] E. J. Candes, J. K. Romberg, and T. Tao (2006). Stable signal recovery from incomplete and inaccurate measurements. *Communications on Pure and Applied Mathematics,* 59, pp. 1207-1223.

[145] E. J. Candès (2006). Compressive sampling. *Proceedings on the International Congress of Mathematicians*, pp. 1433-1452.

[146] M. Rudelson and R. Vershynin (2008). On sparse reconstruction from Fourier and Gaussian measurements. *Communications on Pure and Applied Mathematics,* 61, pp. 1025-1045.

[147] J. A. Tropp and A. C. Gilbert (2007). Signal Recovery From Random Measurements Via Orthogonal Matching Pursuit. *IEEE Transactions on Information Theory*, 53, pp. 4655-4666.

[148] D. L. Donoho, Y. Tsaig, I. Drori, and J.-L. Starck (2012). Sparse solution of underdetermined systems of linear equations by stagewise orthogonal matching pursuit. *IEEE Transactions on Information Theory,* 58, pp. 1094-1121.

[149] D. Needell and R. Vershynin (2009). Uniform uncertainty principle and signal recovery via regularized orthogonal matching pursuit. *Foundations of Computational Mathematics*, 9, pp. 317-334.

[150] A. Gilbert, M. Strauss, J. Tropp, and R. Vershynin (2006). Algorithmic linear dimension reduction in the l_1 norm for sparse vectors. *Arxiv preprint cs/0608079*.

[151] A. C. Gilbert, M. J. Strauss, J. A. Tropp, and R. Vershynin (2007). One sketch for all: fast algorithms for compressed sensing. *Proceedings of the thirty-ninth annual ACM symposium on Theory of computing*, pp. 237-246.

[152] A. C. Gilbert, S. Guha, P. Indyk, S. Muthukrishnan, and M. Strauss (2002). Near-optimal sparse fourier representations via sampling. *Proceedings of the thirty-fourth annual ACM symposium on Theory of computing*, pp. 152-161.

[153] A. C. Gilbert, S. Muthukrishnan, and M. Strauss (2005). Improved time bounds for near-optimal sparse Fourier representations. *Proc. SPIE 5914*, p. 59141A.

[154] J. A. Rice, K. Mechitov, S.-H. Sim, T. Nagayama, S. Jang, R. Kim, *et al.* (2010). Flexible smart sensor framework for autonomous structural health monitoring. *Smart Structures and Systems*, 6, pp. 423-438.

[155] K. Chintalapudi, J. Paek, N. Kothari, S. Rangwala, R. Govindan, and E. Johnson (2005). Embedded sensing of structures: A reality check. *Proceedings of the 11th IEEE International Conference on Embedded and Real-Time Computing Systems and Applications*, pp. 95-101.

[156] G. L. Fenves and M. Tomizuka (2006). Distributed sensor applications for civil infrastructure monitoring and sensing rich approach to the design of modern mechatronic systems. *4th International Conference on Earthquake Engineering*, p. 19.

[157] D. E. Knuth (1981). *The art of computer programming, volume 2: seminumerical algorithms*. Boston: Addison-Wesley Professional, 1981.

[158] R. A. Sielski (2007). *Aluminum marine structure design and fabrication guide.* [Report No. SSC-452]. Retrieved from: http://www.shipstructure.org/pdf/452-II.pdf

[159] J. K. Donald and A. Blair (2007). *Fracture mechanics characterization of aluminum alloys for marine structural applications.* [Report no. SSC-448]. Retrieved from: http://www.shipstructure.org/pdf/448.pdf

[160] R. A. Sielski (2008). Research needs in aluminum structure. *Ships and Offshore Structures*, pp. 57-65.

[161] M. Matsuishi and T. Endo (1968). Fatigue of metals subjected to varying stress. *Presented to the Japan Society of Mechanical Engineers*, Fukuoka, Japan.

[162] T. Dirlik (1985). Application of computers in fatigue analysis. [Ph.D. dissertation, University of Warwick].

[163] S. D. Downing and D. F. Socie (1982). Simple rainflow counting algorithms. *International Journal of Fatigue*, 4, pp. 31-40.

[164] R. I. Stephens, A. Fatemi, R. R. Stephens, and H. O. Fuchs (2000). *Metal Fatigue in Engineering.* Hoboken: John Wiley & Sons.

[165] G. Glinka and J. Kam (1987). Rainflow counting algorithm for very long stress histories. *International Journal of Fatigue*, 9, pp. 223-228.

[166] H. Okamura, S. Sakai, and I. Susuki (1979). Cumulative fatigue damage under random loads. *Fatigue & Fracture of Engineering Materials & Structures*, 1, pp. 409-419.

[167] W. T. Kirkby and P. R. Edwards (1966). *A method of fatigue life prediction using data obtained under random loading conditions*. [RAE Technical Report No. 66023]. Retrieved from: http://repository.tudelft.nl/view/aereports/uuid%3A343f69af-8fed-4bbc-896f-5ac57ba0e78d/

[168] A. Williams, J. Rinne, and M. Miner (1976). Fatigue Analysis of Steel Offshore Structures. *ICE Proceedings*, 60(4), pp. 635-654.

[169] N. Bishop and F. Sherratt (1990). A theoretical solution for the estimation of "rainflow" ranges from power spectral density data. *Fatigue & Fracture of Engineering Materials & Structures*, 13, pp. 311-326.

[170] P. D. Welch (1967). The Use of Fast Fourier Transform for the Estimation of Power Spectra: A Method Based on Time Averaging Over Short, Modified Periodograms," *IEEE Trans. Audio & Electroacoust.* 15, pp. 70-73.

[171] S. O. Rice (1945). Mathematical analysis of random noise. *Bell System Technical Journal*, 23, pp. 282-332.

[172] M. A. Miner (1945). Cumulative damage in fatigue. *Journal of Applied Mechanics*, 12, pp. A159-A164.

[173] J. O. Smith (1942). *The effect of range of stress on the fatigue strength of metals*. University of Illinois Engineering Experiment Station Bulletin No. 316, Urbana, IL.

[174] Department of Defense (1998). *Metallic Materials and Elements for Aerospace Vehicle Structures*. [Report No. MIL-HDBK-5H]. Retrieved from: https://www.lib.ucdavis.edu/dept/pse/resources/fulltext/MILHDBK5H.pdf.

[175] *ASM Material Data Sheet*. [Website]. Retrieved from: http://asm.matweb.com/search/SpecificMaterial.asp?bassnum=MA6061t6

[176] S. Sarkani (1990). Feasibility of auto-regressive simulation model for fatigue studies. *Journal of Structural Engineering*, 116, pp. 2481-2495.

[177] B. E. Boser, I. M. Guyon, and V. N. Vapnik (1992). A training algorithm for optimal margin classifiers. *Fifth Annual Workshop on Computational Learning Theory*, pp. 144-152.

[178] C. M. Bishop (2006). *Pattern Recognition and Machine Learning*. New York, NY: Springer-Verlag.

[179] C.-C. Chang and C.-J. Lin (2011). LIBSVM: A Library for Support Vector Machines. *ACM Transactions on Intelligent Systems and Technology*, 2, pp. 1-27.

[180] C. E. Rasmussen (2004). Gaussian processes in machine learning," in O. Bousquet, U. von Luxberg and G. Ratsch (Eds.) *Advanced Lectures on Machine Learning* (63-71) Berlin: Springer.

[181] D. J. C. MacKay (1997). Gaussian processes-a replacement for supervised neural networks? [Lecture Notes for a tutorial at NIPS 1997]. Retrieved from: http://www.inference.eng.cam.ac.uk/mackay/gp.pdf

[182] C. K. I. Williams (1998). Prediction with Gaussian processes: From linear regression to linear prediction and beyond. In M. Jordan (Ed.) *Learning in graphical models* (599-621) Dordrecht: Springer.

[183] C. E. Rasmussen and H. Nickisch (2010). Gaussian processes for machine learning (GPML) toolbox. *The Journal of Machine Learning Research,* 11, pp. 3011-3015.

[184] D. C. Montgomery (1991). *Introduction to statistical quality control*. New York: Wiley.

[185] J. S. Oakland (2007). *Statistical Process Control*. Abingdon: Routledge.

[186] American Association of State Highway Transportation Officials (1990). *Guide Specifications for Fatigue Evaluation of Existing Steel Bridges*. [Report].

[187] J. W. Fisher, G. L. Kulak, and I. F. C. Smith (1998). A Fatigue Primer for Structural Engineers," [Report - National Steel Bridge Alliance, American Institute of Steel Construction].

[188] S. O'Connor, J. Kim, J. P. Lynch, K. H. Law, and L. Salvino (2010). Fatigue Life Monitoring of Metallic Structures by Decentralized Rainflow Counting Embedded in a Wireless Sensor Network. *Proceeding of ASME 2010 Conference on Smart Materials, Adaptive Structures and Intelligent Systems (SMASIS),* pp. 751-759.

[189] A. V. Clark, C. S. Hehman, D. Gallagher, M. G. Lozev, and P. A. Fuchs (1999). Ultrasonic measurement of stress in pin and hanger connections. *Journal of nondestructive evaluation,* 18, pp. 103-113.

[190] B. A. Graybeal, R. A. Walther, and G. A. Washer (2000). Ultrasonic inspection of bridge hanger pins. *Transportation Research Record: Journal of the Transportation Research Board,* 1697, pp. 19-23.

[191] M. Moore, B. M. Phares, and G. A. Washer (2004). *Guidelines for Ultrasonic Inspection of Hanger Pins*. [Report No. FHWA-HRT-04-042]. Retrieved from: http://www.fhwa.dot.gov/publications/research/infrastructure/structures/04042/04042.pdf

[192] D. Houcque (2008). *Structural integrity assessment of pin and hanger connection of aging highway bridges using finite element analysis.* [Ph.D. dissertation, Northwestern University].

[193] K. Hibbitt (2013). *ABAQUS: User's Manual: Version 6.13*. Retrieved from: http://129.97.46.200:2080/v6.13/books/usi/default.htm

[194] *The Engineering ToolBox*. [Website]. Retrieved from: http://www.engineeringtoolbox.com/

[195] W. C. Young and R. G. Budynas (2002). *Roark's formulas for stress and strain* vol. 7. New York: McGraw-Hill.

[196] B. J. Hamrock, B. O. Jacobson, S. R. Schmid, and B. Jacobson (1999). *Fundamentals of machine elements*. Singapore: WCB/McGraw-Hill.

[197] P. E. Hess, D. Bruchman, I. A. Assakkaf, and B. M. Ayyub (2002). Uncertainties in material and geometric strength and load variables. *Naval engineers journal*, 114, pp. 139-166.

[198] A. S. Nowak (1993). Live load model for highway bridges. *Structural safety*, 13, pp. 53-66.

[199] M. Liu, D. M. Frangopol, and K. Kwon (2010). Fatigue reliability assessment of retrofitted steel bridges integrating monitored data. *Structural Safety*, 32, pp. 77-89.

[200] Y. Q. Ni, X. W. Ye, and J. M. Ko (2010). Monitoring-based fatigue reliability assessment of steel bridges: analytical model and application. *Journal of Structural Engineering*, 136, pp. 1563-1573.